

AD-A071 621

AIR FORCE INST OF TECH WRIGHT-PATTERSON AFB OHIO SCH--ETC F/6 20/3
ELECTRIC AND MAGNETIC FIELDS OF AN INTENSE PULSE OF RELATIVISTI--ETC(U)
1979 K A DREYER

UNCLASSIFIED

AFIT/DS/PH/79-1

NL

1 OF 3
AD
A071621





AFIT/DS/PH/79-1

LEVEL II

~~DDC~~



AD A 071 621

ELECTRIC AND MAGNETIC FIELDS OF AN
INTENSE PULSE OF RELATIVISTIC ELECTRONS
PROPAGATING THROUGH AIR

AFIT/DS/PH/79-1

Kenneth A. Dreyer
Capt USAF

DDC FILE COPY

DDC
RECEIVED
JUL 24 1979
RECEIVED
D

DISTRIBUTION STATEMENT A
Approved for public release;
Distribution Unlimited

79 07 23 05

14
AFIT/DS/PH/79-1

6 ELECTRIC AND MAGNETIC FIELDS OF AN
INTENSE PULSE OF RELATIVISTIC ELECTRONS
PROPAGATING THROUGH AIR.

DISSERTATION

9 Final rept.

Presented to the Faculty of the School of Engineering
of the Air Force Institute of Technology
Air University
in Partial Fulfillment of the
Requirements for the Degree of
Doctor of Philosophy

11 1979

12 194 p.

DDC
RECEIVED
JUL 24 1979
D

10 by
Kenneth A. Dreyer, B.S., M.S.
Captain USAF

Accession For	
NTIS GRA&I	<input checked="" type="checkbox"/>
EDC TAB	<input type="checkbox"/>
Unannounced Justification	<input type="checkbox"/>
By _____	
Distribution/ _____	
Availability Codes	
Dist	Avail and/or special
A	

012 225
DISTRIBUTION STATEMENT A
Approved for public release;
Distribution Unlimited

79 07 23 036 *mt*

PREFACE

The motivation for this research is an on-going interest on the part of the Air Force Weapons Laboratory for atmospheric propagation of electron beams. Earlier work, performed by Briggs, at Lawrence Livermore Laboratory, and Johnston at Science Applications, Inc., focused on propagation of relativistic electron beams through air at sea-level conditions, and on beam currents of 15 kilo-Amperes and less. Models for both the air beam interaction and the electric and magnetic fields were deemed valid only under these conditions of interest. An exception to this was the low-pressure modeling by Briggs for Livermore's FX-25 experimental data. However, the low pressure model of the air-beam interaction did not include electronic attachment or recombination, and is consequently invalid above a pressure of 50 Torr.

Three high-energy electron beam accelerating machines at the Air Force Weapons Laboratory are available for air propagation experiments. A large range in beam current and energy is possible with these machines. Electron beam energy is variable from one MeV to seven MeV, and the beam currents can be varied from 10 kilo-Amperes to 250 kilo-Amperes. In addition, vacuum chambers attached to

all three machines allow the pressure to be varied from a few milli-Torr up to 630 Torr (one Albuquerque atmosphere).

Therefore, in anticipation of and support for the atmospheric propagation experiments, it was decided to initiate a long-term study at the Air Force Weapons Laboratory whose aim was to describe the electric and magnetic fields of an electron beam pulse from the various machines as the pulse passes through air. What is reported here is a part of that study.

To accomplish this required model adaptation and development to extend the calculational regime over all pressures and beam currents of interest. In particular, this study

(1) adapts an air chemistry model from Wittwer that was originally developed for high-altitude electromagnetic pulse (EMP) studies. This model is extensively modified to encompass high pressures (low-altitude) effects and include improvements in ionization modeling. It is the only model in existence capable of adequately describing the state of the plasma over the pressure range of five Torr to 760 Torr.

(2) extends the calculational regime above 15 kilo-Amperes up to 1,000 kilo-Amperes. This study establishes the existence of the current saturation phenomenon and, for the first time, calculates the value of the saturation current.

There are two other features that make this study unique.

(3) A two-dimensional model for the electric and magnetic fields is developed that is based upon the fields themselves, rather than upon the potentials. The computational works of Lee, for example, are based upon EM potentials.

(4) This study extracts the dominant elements of electromagnetic theory to produce a simple one-dimensional model of the fields. The excellent agreement with experiment demonstrates the validity of the models in this study.

There are a large number of people that have aided me in the pursuit of this work; I cannot thank them all, but I would like to especially thank the following people: Edward Lee and Richard Briggs, and the rest of the Lawrence Livermore Laboratory beam group for their time and ideas; Keith Brueckner, University of California at San Diego, and John Jackson, Air Force Academy, for initially piquing my interest on this project; Robert Johnston, Science Applications, Inc., Palo Alto, for many fruitful discussions and for persuading me to perform the ionization lag calculations; Leon Wittwer, SAMS0, for his initial support and critical review; Norman Roderick, Harald Dogliani, and the rest of the Air Force Weapons Laboratory management that gave me time for this work; and Phil Nielsen, my

dissertation adviser. Most of all, I thank my wife,
Joyce, and my children for supporting me in those crucial
years.

Contents

	<u>Page</u>
Preface	iii
List of Figures	ix
List of Tables	xi
Abstract	xii
I. Introduction	1
Purpose	1
Background	4
Previous Research	10
Scope of Present Work	12
Major Conclusions	17
Outline of Remaining Sections	19
II. Two-Dimensional Model of EM Fields	20
Introduction	20
Principal Assumptions	20
Basic Equations	22
Retarded Time Transformation	27
Boundary Conditions	28
Discussion	29
III. One-Dimensional Model of EM Fields	31
Introduction	31
Principal Assumptions	32
Derivation of Model Equations	33
Comparison with Circuit Equation	39
Discussion	40
IV. Ionization Model	44
Introduction	44
Derivation of Fluid Equations	45
Principal Assumptions	50
Equations of the Ionization Model	57
Boundary Conditions	58
Cascade Ionization	59
Discussion	67

Contents

	<u>Page</u>
V. Computational Results	70
Introduction	70
Pulse Shape	71
Behavior of Fields	72
Comparison of the One- and Two-Dimensional Models	78
Comparison with Experiment and Previous Calculations	86
Effects of Cascade Ionization Time Lag	95
Saturation of Net Current	98
Discussion	101
VI. Major Conclusions and Recommendations	103
Major Conclusions	103
Recommendations	104
References	106
Appendix A: EM Fields of a Beam in a Vacuum	111
Analytic Approximation	115
Numerical Calculation	122
Appendix B: Reaction Rates	131
Rate Equations	131
Analytic Approximation	146
Appendix C: Program BEAM1	151
Finite Difference Equations	151
Solution Algorithm	154
Appendix D: Program BEAM2	159
Appendix E: Program MONTY	162
Simulation Method	162
Solution Algorithm	165
Experimental Cross Section Data	167
Theoretical Cross Sections	170
Vita	192

List of Figures

<u>Figure</u>		<u>Page</u>
1	Longitudinal Density Profile	7
2	Radial Density Profile	7
3	Radial Electric Field	8
4	Longitudinal Electric Field	8
5	Azimuthal Magnetic Field	8
6	Differential Ionization Cross Section . . .	60
7	Cascade Ionization Time Lag	62
8	Ionization, Non-Zero Field	64
9	Behavior of Fields	73
10	Radial Variation of Radial Electric Field .	75
11	Radial Variation of Axial Electric Field .	76
12	Radial Variation of Azimuthal Magnetic Field	77
13	Behavior of Fields, BEAM2	79
14	Comparison of Calculated and Analytically Estimated Radial Variation of Axial Elec- tric Field	81
15	Comparison of Calculated Axial Behavior of Fields	83
16	Comparison of Calculated and Analytically Estimated Radial Variation of Axial Elec- tric Field, 76 Torr	84
17	Comparison of Radial Variation of Electron Density at 760 and 76 Torr	85
18	Comparison of Conductivity Calculations from Johnston and Dreyer	87
19	Comparison of Electron and Neutral Gas Energy from Johnston and Dreyer	88

List of Figures

<u>Figure</u>		<u>Page</u>
20	Comparison of Experimental Net Current with Values from EMPULSE and BMCOND	90
21	Comparison of Experimental Net Current with Values from BEAM1 and BEAM2	91
22	Comparison of Experimental Electron Density with Calculated Values	92
23	Comparison of Calculated Electron Density With and Without Cascade Ionization Lag . .	97
24	Net Current at the Top of the Current Rise.	99
25	New Current at the Rear of the Pulse . . .	100
26	Longitudinal Variation of Vacuum Fields . .	129
27	Radial Variation of Vacuum Fields	130
28	Avalanche, Attachment, and Recombination Coefficients	136
29	Collision Frequencies	137
30	Comparison of Collision Frequency Models .	139
31	Comparison of Avalanche Models	141
32	Flow Chart for Program BEAM1	156
33	Flow Chart for Solution of Ionization Model Equations	158
34	Experimental Molecular Nitrogen Cross Sections	168
35	Experimental Molecular Nitrogen Reaction Rates	169
36	Comparison of Experimental and Theoretical Ionization Cross Sections for Molecular Nitrogen	174

List of Tables

<u>Table</u>		<u>Page</u>
I	Summary of Beam Calculations	14
II	Summary of Parameters	15
III	Comparison of Theory and FX-100 Data . . .	94
IV	N ₂ Vibrational Excitation Cross Sections .	178
V	N ₂ Electronic Excitation Cross Sections . .	183
VI	N ₂ Total Ionization Cross Sections	187
VII	N ₂ Momentum Transfer Cross Sections	188
VIII	Parameters for Electron Impact	189
IX	Comparison of Stopping Power Formulas for Electrons	191

Abstract

Since propagation characteristics of an electron beam traversing a neutral gas are determined by the response of the beam electrons to their self-fields, an accurate evaluation of the electric and magnetic (EM) fields is essential to any propagation analysis. We report here on theoretical models that were developed for the electromagnetic fields associated with an electron beam propagating in air. One- and two-dimensional models of the fields, and a model for the electron avalanche of the air, were solved on a computer. The major conclusions from calculational results are:

(1) The ionization model adequately describes the ionization process over a pressure range of from five Torr to 760 Torr.

(2) Ionization lag from the high energy secondary electrons is unimportant.

(3) In many cases the one-dimensional model was found to be as good as the two-dimensional model.

(4) The net current saturates near 15 kilo-Amperes at sea-level pressure, and saturates at lower values at lower air pressures.

ELECTRIC AND MAGNETIC FIELDS OF AN
INTENSE PULSE OF RELATIVISTIC ELECTRONS
PROPAGATING THROUGH AIR

I. INTRODUCTION

Purpose

Recently, intense interest has surfaced for employing relativistic electron beams for various scientific and military purposes. One major application is to heat a plasma, or pellet, to thermonuclear temperatures (Refs 1, 2). Since the expected thermonuclear reaction is quite intense the accelerator producing the electron beam must be separated from the target by a stand-off distance on the order of 10 meters. In addition, a neutral gas, probably air, may be placed in the region between the accelerator nozzle and the target to absorb some of the thermonuclear energy and minimize damage to the accelerator. Thus, for this application to be successful, the electron beam must stably traverse the stand-off distance with little or no spreading or energy loss. Some other applications also require propagation over extended distances.

Successful propagation through air over extended distances is by no means assured. A host of parasitic

phenomena seemingly conspire to severely limit propagation of intense electron beams. Of the experiments performed to date no electron beams have been stably propagated through air at atmospheric pressure (Refs 3, 4, 5, 6). In all of the experiments the mechanism that prevented successful propagation was beam breakup caused by the hose instability (Ref 7). In a series of experiments performed at the Air Force Weapons Laboratory the hose instability was minimized to the extent that the beam propagated a distance of 12 feet without significant hose distortions (Ref 6). However, the beam was seen to diverge before breakup due to elastic scatter off of gas molecules (Ref 8). This divergence, called "Nordsieck expansion", is expected to be prevalent at atmospheric pressure whenever the hose instability is not present.

Although the strength of the hose instability is lessened at lower pressures another instability, the two-stream instability, can completely stop the beam after traveling just a few centimeters (Ref 9). Of the three experiments performed to date on intense electron beam propagation in reduced pressure air, all report evidence that the two-stream instability occurs under certain conditions (Refs 3, 4, 5). Of these experiments, one showed no stable propagation at any pressure (Ref 3), another showed a very narrow stable propagation window at a pressure of two Torr (Ref 4), and the third showed a narrow stable propagation window at a pressure of 20 Torr

(Ref 5). Apparently, the hose instability causes the beam to break up at pressures above the window pressure, and the two-stream instability stops the beam below the window pressure.

In addition to these phenomena, there are others, such as beam-head erosion (Ref 4) and return current heating (Ref 10) that have been observed to degrade beam propagation.

The behavior of all of these phenomena are critically dependent upon the environment seen by the beam. In particular, the beam electrons are acted upon by their own electric and magnetic (EM) fields, and these fields ultimately become the sources for the parasitic phenomena that degrade propagation through air. Until quite recently an adequate description of the EM fields was not available, primarily because the dominant interactions had not been extracted from the details of the beam electron-air interaction. As an example, in EM field calculations performed by Johnston in 1975 (Ref 11), he considered over 300 chemical reactions that could be induced in air by an intense pulse of relativistic electrons passing through air.

It has been the intent of this work to adapt the simplified theories of others to the electron beam-air interaction problem, and devise simplified, yet accurate, models where necessary in order to extract the dominant physical mechanisms so that accurate determinations of the

EM fields can be made. Therefore, in this study, these fields are determined for an intense pulse of relativistic electrons propagating through cold air that has not been previously ionized. The coupled air ionization-beam electric field problem is the most difficult of all propagation problems.

As the beam electrons pass through air they interact with the gas molecules to produce a weakly ionized plasma. This plasma is composed of electrons and an equal number of singly ionized positive ions. Since the ions are immobile over the time scales of interest in this study (less than 10^{-7} seconds), any current that flows in the plasma is carried by the plasma electrons. The EM fields are strongly influenced by the plasma conductivity, so the EM fields are strongly coupled to the free electron density. Therefore, this study also treats the ionization process in some detail. We include beam electron impact ionization, ionization produced by high energy secondary electrons (cascade ionization), and ionization produced by breakdown in the intense EM fields associated with the beam (avalanche ionization). The same general procedures used here can be used for propagation of other types of particles, or through other neutral gases, providing the appropriate reaction rates and cross sections are employed.

Background

A great deal of information has been amassed in

recent years describing some facets of direct (impact plus cascade) ionization of a neutral gas by energetic charged particles and avalanche ionization by intense EM fields. Cosmic ray studies, for example, include ionization estimates of the slowing down of solar protons in the upper atmosphere (Ref 12). The electromagnetic pulse phenomenon depends, in part, on the secondary electrons generated as Compton electrons ionize the background gas (Ref 13). Finally, a large amount of literature is available on electrical discharges in gases (Refs 14, 15).

A relativistic pulse of charged particles ionizes the air by both methods; direct ionization by energetic charged particles, and avalanche ionization produced by intense EM fields. For example, a one MeV electron produces about 25 electrons per centimeter of travel through sea level density air. Some of these electrons are quite energetic and, consequently, produce more ionization in a cascade process. This results in an additional 35 electrons per centimeter of travel. These cascade electrons are produced over a period of about one nanosecond, based on estimated cross sections found in Appendix E. This phenomenon is called the "ionization time lag". The total ionization rate, including both impact and cascade ionization, is roughly 2×10^{12} electrons per second per beam particle.

In addition to this ionization mechanism, electric fields may reach levels that rapidly accelerate thermal

electrons to energies above the ionization threshold, resulting in avalanche ionization. The ionization threshold is near 12.8 eV for oxygen and 15.6 eV for nitrogen. For a beam in a vacuum with a current of $I=10$ kilo-Amperes and a radius a of one centimeter, the radial electric field at the radial edge of the pulse is

$$E_r \sim \frac{I}{ca} = 10^3 \text{ sV/cm} = 3 \times 10^7 \text{ V/m} \quad (1-1)$$

where c is the speed of light. This value is well above the sea level air breakdown threshold. Longmire (Ref 16 and Appendix B) estimates the e-folding time for the avalanche produced by this field to be about 10^{-11} seconds.

This rapid ionization and concomitant increase in the electrical conductivity is responsible for a rapid departure of the electric fields from the fields of a pulse in a vacuum. Consider a pulse with longitudinal and radial profiles given in Figures 1 and 2. When passing through air the pulse fields change from their vacuum values to resemble the fields illustrated in Figures 3, 4 and 5. These changes all occur in the rise portion of the pulse, Δz . The radial electric field, E_r , is determined solely by the net space charge. Hence, the rising conductivity will reach a value in a short period of time that is high enough to short out the radial field. The characteristic time for the field to decay is the charge neutralization

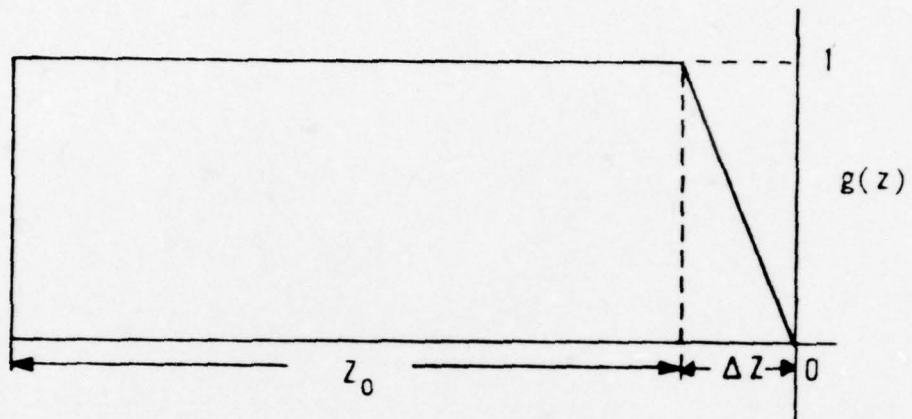


Figure 1. Longitudinal Density Profile

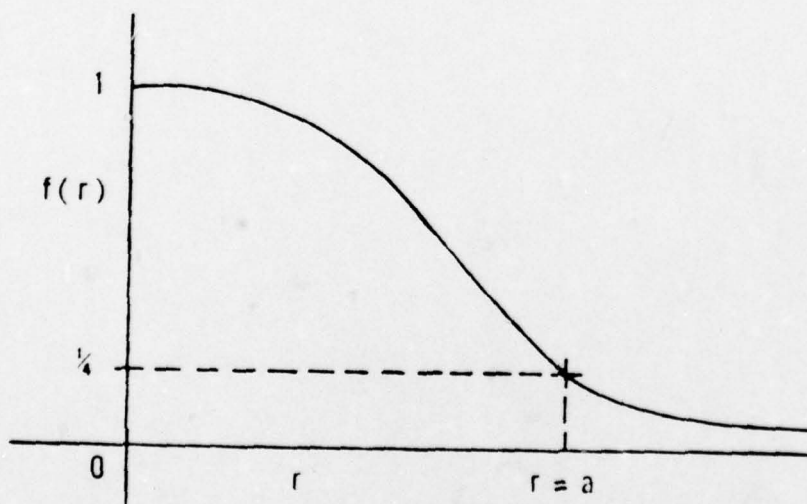


Figure 2. Radial Density Profile

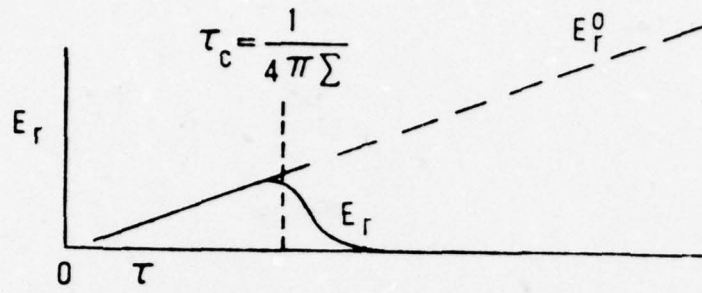


Figure 3. Radial Electric Field

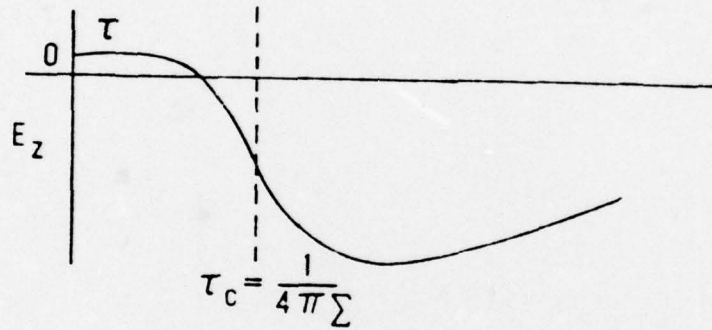


Figure 4. Longitudinal Electric Field

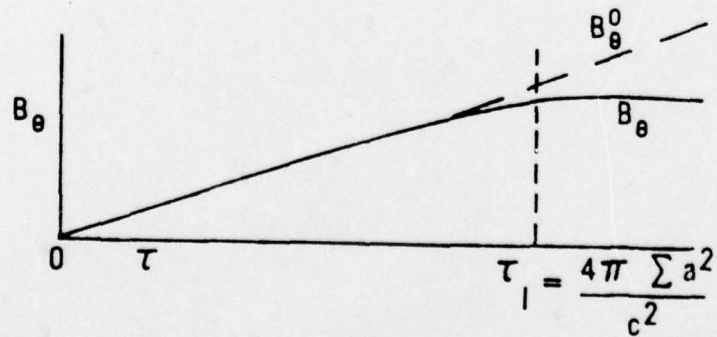


Figure 5. Azimuthal Magnetic Field

time, τ_c , defined by

$$\tau_c = \frac{1}{4\pi\Sigma(\tau_c)} \quad (1-2)$$

where $\tau = t - z/\beta c$ is the time elapsed since pulse arrival and $\Sigma(\tau)$ is the background electron conductivity. As the radial field decays (Fig 3) the longitudinal field (Fig 4) is driven to assume a value which is opposite in sign and normally much stronger than the longitudinal field in a vacuum. After the radial field has decayed away completely the longitudinal field has assumed its inductive form determined from $\frac{d}{dt} B_\theta$. Since E_z acts in a direction so as to generate a plasma current which flows counter to the beam current, E_z must decrease with increasing conductivity. The result is that the plasma current increases until the time derivative of the plasma current and beam current are equal and opposite. At this point the magnetic field is "frozen" into the plasma (background electrons) created by the beam, and B_θ ceases to increase. The characteristic time for this to occur is called the current saturation time and is estimated to be

$$\tau_I = \frac{4\pi a^2 \Sigma(\tau_I)}{c^2} \quad (1-3)$$

Previous Research

This complex interaction between the beam particles, the EM fields, and the background electrons was first modeled by Johnston (Ref 11). He considered a pulse of relativistic electrons with the same longitudinal profile as shown Figure 1, but the radial profile was considered constant out to radius a , and zero for radial distances greater than a . Instead of solving Maxwell's equations directly he employed the following circuit equation,

$$E_z = -L \frac{\partial I}{\partial t} \quad (1-4)$$

where

$$\begin{aligned} L &= \text{inductance, an adjustable parameter, generally} \\ &\quad \text{of order } 2/c^2 \\ I &= \text{total current} = I_b + I_p \\ I_b &= \text{beam current} \\ I_p &= \text{plasma (counter) current, } \equiv \pi a^2 \Sigma E_z \end{aligned} \quad (1-5)$$

This circuit equation (1-4) can be derived by ignoring the displacement current, performing a retarded time transformation to the beam frame, assuming no variation of parameters in the radial direction, and time invariance in the retarded frame.

Equation (1-4) was solved simultaneously with a large set of rate equations (over 300), describing the reactions among many different species of particles found in the

air, in order to calculate the conductivity. Johnston further assumed a beam particle ionization rate of 100 electrons per centimeter of travel, all produced instantaneously and with an energy of 7.5 eV. The radial electric field was ignored and the magnetic field inferred from the net current. Obviously, radial information is lost in his model.

More recently, Lee (Ref 17) has modeled these interactions in his numerical program, EMPULSE. In his model the fields are coupled to the background electrons through the conductivity given by

$$\Sigma = \frac{e^2 n_e}{m_e v_m} \quad (1-6)$$

with $v_m = 6.4 \times 10^9 / (\text{Torr})$, independent of the electron temperature. The beam electron ionization rate is taken as 63 electrons produced per centimeter of travel. The avalanche coefficient he used is an E/p fit from data of Felsenthal and Proud (Ref 18). Recombination and dissociative attachment are ignored. Pulse profiles considered by Lee are similar to those shown in Figures 1 and 2, but they differ in that the top of the rise portion is rounded.

Lee's program does not evaluate the field components themselves, but rather employs the scalar potential, ϕ , and the longitudinal component of the vector potential, \vec{A} . In a fashion similar to Johnston he employs the retarded

time transformation to the beam frame and assumes time invariance in the new set of independent variables. He retains variations in the radial dimension but does not include attachment or recombination. Thus, the program is two-dimensional and time independent. Originally developed to simulate the hose instability, EMPULSE contains many other features which are necessary to adequately describe the instability. The computational times are quite long, however, requiring the simplified handling of the background electrons. Lee also presents experimental data that is compared to the results of EMPULSE. The agreement is poor at pressures above 50 Torr.

Scope of Present Work

In this work we improve upon the previous efforts in the following ways:

1. We derive a two-dimensional model (r and z variation) of the EM fields from Maxwell's equations. We employ the fields directly, rather than the potentials, and so we eliminate the necessity of numerical differentiation of the potentials to find the electric field strength. A key assumption in the model is setting the longitudinal displacement current equal to zero. Although this is not rigorously correct, it is at least consistent with the observation that in the limit of zero conductivity and very high beam electron energy, the longitudinal field vanishes.

2. Guided by the results of the two-dimensional

model a one-dimensional model (z variation only) is derived by explicitly modeling the radial variation of the conductivity. From this assumed variation of the conductivity, radial variation of other parameters is found analytically. For most cases the numerically determined axial variation of the fields closely agree. The one-dimensional model is computationally simpler than the two-dimensional model, and the simplicity of the equations allows deeper physical insight.

3. We present a bulk ionization model, consisting of a set of fluid equations for the plasma electrons, and a lumped restricted set of reaction rates. This model was originally devised by Wittwer (Ref 19) for studies of the high-altitude electromagnetic pulse (EMP). It is modified here to include low-altitude effects and cascade ionization. Although the model is considerably simpler than some, it retains all of the important reactions. It is the only documented model that accurately describes the state of the background plasma produced by the beam for air pressures of five Torr to 760 Torr. Its simplicity allows insight into the role of various reactions, and its accuracy resolves some key issues.

4. The calculational regime is extended to currents up to 1,000 kilo-Amperes. Previous calculations focused on beam currents near 10 kilo-Amperes. Above 10 kilo-Amperes a pronounced saturation of the net current (beam current plus plasma current) is predicted, and is in

agreement with available experimental data. Status of these calculations is summarized in Table I.

TABLE I

SUMMARY OF BEAM CALCULATIONS

These categories are included by the following authors:

	Johnston	Lee	Dreyer
Longitudinal Dimension	X	X	X
Radial Dimension		X	X
Maxwell's Equations solved via-			
Circuit Equation	X		X
Vector Potential		X	
Electric and Magnetic Field			X
Includes-			
Radial Electric Field		X	X
Avalanche Ionization	X	X	X
Recombination & Attachment	X		X
Electron Ionization Cascade			X

The range of parameters considered in this study is given in Table II, and explained below. Of the parameters listed here only two, air pressure and pulse current, are limited by assumptions of the models. The rest of the parameters are limited by practical considerations.

TABLE II

SUMMARY OF PARAMETERS

Beam Electron Kinetic Energy:	1 - 10 MeV
Pulse Current:	$I \ll I_A$, 1-1,000kA
Bennett Radius:	0.1 cm - 10 cm
Pulse Duration:	1×10^{-8} - 1×10^{-7} sec
Air Pressure:	5-760 Torr

Electron kinetic energies are taken to be between one and 10 MeV because energies below about one MeV are not strongly considered for the fusion application, and virtually no machines exist with high energy densities that have beam kinetic energies above 10 MeV.

The pulse current must be less than the Alfvén current, I_A , defined by

$$I_A = \frac{\beta \gamma m c^3}{e}$$

and is $1.70 \times 10^4 \beta \gamma$ Amperes for electrons. It is the maximum current a charge neutralized beam can carry (Refs 20, 21). Requiring $I \ll I_A$ means that the beam particles in a charge neutralized beam follow nearly straight line trajectories. The lower limit of one kA is chosen to bound the current saturation phenomenon.

The equilibrium radius that a pulse establishes after

exiting an accelerator is determined, in large part, by the scatter produced by the exit foil, if a foil is used (Ref 22). A realistic minimum of 0.1 cm is established by consideration of foil thickness and type. Above a 10 cm radius a 1,000 KA pulse has an energy density too small to be of importance in the fusion application.

The pulse duration is taken between 1×10^{-8} and 1×10^{-7} seconds. This range in pulse length is chosen since most accelerators, and some planned accelerators, that produce intense relativistic electron beams have pulse lengths in this range.

A fusion reactor, employing electron beams, may require a partially evacuated path for the beam to traverse. The two-stream instability threshold is near a pressure of one Torr, with the actual pressure threshold depending upon the beam temperature. Rapid attenuation of the beam follows onset of this instability. Thus, we restrict our attention to pressures at and above five Torr.

Three numerical programs were written in the course of this study. The first program, named BEAM1, solves Maxwell's equations in two dimensions while simultaneously solving the fluid equations of the ionization model. It is assumed that in a coordinate frame moving with the velocity of the beam particles the fields are time independent, and the equations are solved in such a frame.

The second program, named BEAM2, solves the one-dimensional EM field equations simultaneously with the

equations of the ionization model. Since numerical evaluation of the fields is only carried out over the axial direction, BEAM2 is considerably cheaper to run than BEAM1. Execution times for BEAM2 typically run a factor of 50 less than execution times for BEAM1. Equations solved by BEAM2 are solved in the same reference frame as in BEAM1.

A third numerical program, named MONTY, was written to investigate the details of the secondary electron ionization cascade. Results from this program are used as a source for deriving a simplified model of the cascade that is included in the ionization model. Program MONTY employs Monte-Carlo simulation of the interactions between the plasma electrons and the neutral gas. Both elastic and inelastic processes are handled explicitly in a one-dimensional velocity space. An external electric field is applied requiring one dimensional electron trajectories to be calculated. Program MONTY is expensive to run so results are necessarily limited to short pulse times and pressures substantially below atmospheric pressure.

While introducing a significant reduction in mathematical complexity, we feel that the present calculations are the most accurate available, and extend over a far wider range of parameters.

Major Conclusions

1. For what experimental data exist both the one-dimensional and two-dimensional models, along with the

ionization model, adequately predict the observed electron density and net current flow. Differences between experiment and theory may be attributed to the uncertainty in modeling the pulse shape.

2. In view of the fact that the one-dimensional model is in close agreement with the two-dimensional model, and with experimental data, it is concluded that the one-dimensional model developed here adequately predicts the EM fields, conductivity generation, and net current flow. The substantial savings in computing time over the two-dimensional model allow parameter studies to be performed cheaply.

3. At low pressures (less than 100 Torr), conductivity generation in the pulse rise portion is dominated by avalanche ionization, rather than by direct ionization. Consequently, field calculations in this portion of the pulse and at these pressures are insensitive to the delay in ionization by the high energy secondary electrons that are created by beam electron impact. Calculated values of the net current and EM fields are virtually independent of the delay time. Thus, the phenomenon of ionization time lag is unimportant in determining EM fields or net current flow.

4. Ignoring avalanche ionization, the magnetic diffusion time scales linearly with the beam current. Consequently, the "frozen-in" value of the magnetic field and the net current flowing in the pulse are virtually inde-

pendent of the beam current, as long as the beam current is sufficiently high. Thus, the net current is seen to saturate. At a pressure of one atmosphere saturation occurs for beam currents above 15 kilo-Amperes. The saturation value of the net current decreases with a decrease in air pressure.

Outline of Remaining Sections

In the next section we derive the two-dimensional EM model equations. Simplifications and approximations introduced in their derivation are discussed. Section III contains the development of the one-dimensional EM model. The one-dimensional model is derived by handling the radial variation of parameters in an analytic fashion. In Section IV the ionization model is introduced. Important results are given in Section V, and the major conclusions of this work, along with recommendations for further research are presented in Section VI. Some additional details are found in the appendices.

II. TWO-DIMENSIONAL MODEL OF EM FIELDS

Introduction

In this section we derive a set of equations for the electric and magnetic fields that is two-dimensional (r and z variation) and time independent. Although some limiting assumptions are applied to Maxwell's equations, all important terms are retained. Since both axial and radial variations of the fields are included, behavior of the fields in both dimensions can be observed from numerical solutions of the equations. From these equations, and with additional assumptions, we derive the equations of the one-dimensional model in Section III.

The remainder of this section is split into several parts. In the next part we present the principal assumptions of the two-dimensional model, and, in the following part, the basic field equations are derived. After that we apply the retarded time transformation, and require time invariance in the transformed system to arrive at the model equations. Finally, the boundary conditions are specified, and a short discussion follows.

Principal Assumptions

The principal assumptions employed in the two-dimensional model are the following:

1. Axial symmetry. By requiring axial symmetry the only non-zero field components are E_r , the radial electric field, E_z , the axial electric field, and B_θ , the azimuthal magnetic field.

2. Paraxial motion of beam electrons. We do not require here that the beam electrons move exactly parallel to the beam axis, but we do require that the beam electrons move almost parallel to the beam axis. That is, we require $|\vec{v}| \ll \beta c$, where \vec{v} is the perpendicular beam electron velocity, and βc is the parallel velocity. This assumption is valid in all parts of the beam.

3. Axial displacement current is ignored. This assumption is valid as long as $a/\Delta z \ll 1$, where a is the beam radius and Δz is the beam rise length. It is made to reduce the complexity and execution time of the numerical program, BEAM1, that solves the two-dimensional model equations. Retaining the displacement current results in an advective differential equation, so the associated difference equation is subject to the Courant condition (Ref 23). Ignoring the term results in a diffusive differential equation with an associated finite difference equation that is not subject to the Courant condition (Ref 24). Output from BEAM1 shows that, in all of the cases considered in this study, the axial displacement current density is at least an order of magnitude less than the axial conduction current density.

4. Beam fields translate rigidly in space. Thus, all parameters are only functions of the retarded time coordinate $(t-z/\beta c)$. This assumption is analogous to the "high-frequency approximation" of Karzas and Latter (Ref 25) in their analysis of the electromagnetic pulse generated by a high altitude nuclear burst. This assumption is rigorously correct in the limit $\beta \rightarrow 1$ because,

a. for $\beta = 1$ the paraxial approximation 2. reduces to rigid translation of the beam at the speed of light.

b. for $\beta = 1$ the domain where EM fields can be determined reduces to the half-space in the direction of motion of the beam electrons (Ref 26), so the fields can only be influenced by events occurring in that half space.

c. the fields vanish at the head of the pulse. The author has verified this assumption for the case $\beta \geq 0.9$ by computer solution of the exact equations of Maxwell. It is clear that this assumption will break down if the paraxial approximation does not hold.

Basic Equations

In vector form, Maxwell's equations are

$$\vec{\nabla} \cdot \vec{E} = 4\pi\rho \quad (2-1)$$

$$\vec{\nabla} \times \vec{E} = -\frac{1}{c} \frac{\partial \vec{B}}{\partial t} \quad (2-2)$$

$$\vec{\nabla} \times \vec{B} = \frac{4\pi}{c} \vec{J} + \frac{1}{c} \frac{\partial \vec{E}}{\partial t} \quad (2-3)$$

By assuming axial symmetry, the component equations in cylindrical coordinates are

$$\frac{1}{r} \frac{\partial}{\partial r} (rE_r) + \frac{\partial E_z}{\partial z} = 4\pi\rho \quad (2-4)$$

$$\frac{\partial E_z}{\partial r} - \frac{\partial E_r}{\partial z} = \frac{1}{c} \frac{\partial B_\theta}{\partial t} \quad (2-5)$$

$$\frac{\partial E_r}{\partial t} + 4\pi J_{pr} = -c \frac{\partial B_\theta}{\partial z} \quad (2-6)$$

$$\frac{\partial E_z}{\partial t} + 4\pi(J_{bz} + J_{pz}) = \frac{c}{r} \frac{\partial}{\partial r} (rB_\theta) \quad (2-7)$$

where J_{pr} is the radial component of the plasma current density, J_{pz} is the axial component of the plasma current density, and J_{bz} is the axial component of the beam current density. Under the paraxial approximation the radial component of the beam current density is zero.

If we specify the plasma current density, \vec{J} , then the four equations (2-4) through (2-7), in the four variables ρ , E_r , E_z , and B_θ , form a closed set. By properly specifying boundary conditions a unique solution can be obtained. Notice, too that equations (2-5) through (2-7)

in the variables E_r , E_z , B_θ , form a closed set and can be solved without calculating the net charge density. Therefore, we consider only the curl equations given in component form in (2-5) through (2-7). We specify the plasma current density by a set of fluid equations describing the state of the plasma, to be presented in Section IV.

We now derive an equation for the radial electric field by ignoring the displacement current density and the plasma current density in the axial direction. Although the plasma current density may approach that of the beam current density in some parts of the beam, this occurs only after the radial field has decayed substantially and is no longer important. The resulting differential equation is uncoupled from the other fields.

Taking the divergence of both sides of equation (2-3), we have, in cylindrical coordinates,

$$\frac{1}{r} \frac{\partial}{\partial r} \left[r \left(\frac{\partial E_r}{\partial t} + 4\pi J_{pr} \right) \right] + \frac{\partial}{\partial z} \left[\frac{\partial E_z}{\partial t} + 4\pi (J_{bz} + J_{pz}) \right] = 0 \quad (2-8)$$

We have established in Appendix A that, for $\Sigma=0$, and

$$\frac{a}{\gamma \Delta z} \ll 1 \quad (2-9)$$

where a is the Bennett radius of the pulse and Δz is the rise length, and γ is the relativistic factor, then

$$E_z \ll E_r \quad (2-10)$$

Guided by this result for fields in a vacuum we ignore the displacement current density and the plasma current density in the axial direction by requiring

$$\left| \frac{1}{r} \frac{\partial}{\partial r} \left[r \left(\frac{\partial E_r}{\partial t} + 4\pi J_{pr} \right) \right] + \frac{\partial}{\partial z} [4\pi J_{bz}] \right| \gg \left| \frac{\partial}{\partial z} \left[\frac{\partial E_z}{\partial t} + J_{pz} \right] \right| \quad (2-11)$$

Then we have

$$\frac{1}{r} \frac{\partial}{\partial r} \left[r \left(\frac{\partial E_r}{\partial t} + 4\pi J_{pr} \right) \right] = -4\pi \frac{\partial J_{bz}}{\partial z} \quad (2-12)$$

Now

$$-4\pi \frac{\partial J_{bz}}{\partial z} = -4\pi \beta c \frac{\partial \rho_b}{\partial z} = 4\pi \frac{\partial \rho_b}{\partial t} \quad (2-13)$$

where ρ_b is the beam charge density. From the divergence equation, and again ignoring the axial field, we have

$$4\pi \frac{\partial \rho_b}{\partial t} = \frac{1}{r} \frac{\partial}{\partial r} \left(r \frac{\partial E_r^0}{\partial t} \right) \quad (2-14)$$

where E_r^0 is the radial electric field of the beam propagating in a vacuum. Equation (2-12) becomes

$$\frac{1}{r} \frac{\partial}{\partial r} \left[r \left(\frac{\partial E_r}{\partial t} + 4\pi J_{pr} \right) \right] = \frac{1}{r} \frac{\partial}{\partial r} \left(r \frac{\partial E_r^{\circ}}{\partial t} \right) \quad (2-15)$$

Integrating once and employing the condition,

$$\lim_{\Sigma \rightarrow 0} E_r = E_r^{\circ} \quad (2-16)$$

we arrive at

$$\frac{\partial E_r}{\partial t} + 4\pi J_{pr} = \frac{\partial E_r^{\circ}}{\partial t} \quad (2-17)$$

Finding an equation for the axial electric field is considerably simpler. Operating on (2-7) with $\frac{1}{c} \frac{\partial}{\partial t}$ and on equation (2-5) with $\frac{c}{r} \frac{\partial}{\partial r} (r \quad)$, we have

$$\frac{1}{r} \frac{\partial}{\partial r} \left[r \left(\frac{\partial E_z}{\partial r} - \frac{\partial E_r}{\partial z} \right) \right] - \frac{1}{c} \frac{\partial}{\partial t} \left[\frac{\partial E_z}{\partial t} + \frac{4\pi}{c} (J_{bz} + J_{pz}) \right] = 0 \quad (2-18)$$

We again ignore the axial displacement current density.

Then equation (2-18) becomes

$$\frac{1}{r} \frac{\partial}{\partial r} \left[r \left(\frac{\partial E_z}{\partial r} - \frac{\partial E_r}{\partial z} \right) \right] = \frac{4\pi}{c^2} \frac{\partial}{\partial t} (J_{bz} + J_{pz}) \quad (2-19)$$

Finally, the magnetic field is found by integrating over r

in (2-7), and again ignoring the axial displacement current density. This yields

$$B_{\theta} = \frac{4\pi}{cr} \int_0^r r' (J_{bz} + J_{pz}) dr' \quad (2-20)$$

Retarded Time Transformation

We note that the fields described by equations (2-17), (2-19), and (2-20) are functions of the triplet (r, z, t) , so numerical algorithms that solve these equations must necessarily be two-dimensional and time-dependent. We introduce a great simplification to the numerical algorithms by transforming the field equations to the beam frame (non-relativistic), and observing that the fields are independent of time in that frame. We reduce the functional dependence of the fields on the triplet (r, z, t) to the doublet (r, τ) . The transformation equations are:

$$\tau = t - z/\beta c \quad (2-21)$$

$$\lambda = z/\beta c \quad (2-22)$$

In the transformation $(z,t) \rightarrow (\tau,\lambda)$, λ plays the role of time in the new system, while τ plays the role of axial distance (although it has units of time). Derivatives transform according to

$$\frac{\partial f}{\partial t} = \frac{\partial f}{\partial \tau} \frac{\partial \tau}{\partial t} + \frac{\partial f}{\partial \lambda} \frac{\partial \lambda}{\partial t} = \frac{\partial f}{\partial \tau} \quad (2-23)$$

$$\frac{\partial f}{\partial z} = \frac{\partial f}{\partial \tau} \frac{\partial \tau}{\partial z} + \frac{\partial f}{\partial \lambda} \frac{\partial \lambda}{\partial z} = \frac{1}{\beta c} \left(\frac{\partial}{\partial \lambda} - \frac{\partial}{\partial \tau} \right) \quad (2-24)$$

Setting the λ (time) derivatives equal to zero we have

$$\frac{\partial f}{\partial z} = - \frac{1}{\beta c} \frac{\partial f}{\partial \tau} \quad (2-25)$$

The resulting field equations are

$$\frac{\partial E_r}{\partial \tau} + 4\pi J_{pr} = \frac{\partial E_r^o}{\partial \tau} \quad (2-26)$$

$$\frac{1}{r} \frac{\partial}{\partial r} \left[r \left(\frac{\partial E_z}{\partial r} + \frac{1}{\beta c} \frac{\partial E_r}{\partial \tau} \right) \right] = \frac{4\pi}{c^2} \frac{\partial}{\partial \tau} (J_{bz} + J_{pz}) \quad (2-27)$$

The equation for B_θ , (2-20), remains unchanged. These are the two-dimensional model field equations.

Boundary Conditions

For a beam propagating in air, far from any boundaries, the correct boundary condition is that the fields vanish infinitely far from the beam. These conditions appear impossible to implement in a numerical program, so we choose an approximate set. They are,

1. All fields vanish at the very front of the pulse. Because the beam electrons are relativistic and $a/\Delta z \ll 1$, the actual fields at the front of the pulse are much less than the fields in the remainder of the pulse. In Figure 27, Appendix A, plots are given for the fields of a pulse in a vacuum. The curves show that the fields are quite small at the front of the pulse.

2. At $r = 0$, $E_r = B_\theta = \partial E_z / \partial r = 0$. The radial electric field is essentially an electrostatic field so it must vanish on the axis. In addition, the magnetic field which is driven by axial currents, must also vanish on the axis. Thus, to maintain consistency with the curl equation (2-5) at $r = 0$, the radial gradient of the axial field must vanish there.

3. At $r = r_{\max}$, E_r and E_z take on the values of a pulse traveling in a vacuum. Plasma electrons are moved radially outward to some distance, b , which increases back from the pulse head. At radial distances greater than b the net charge contained inside that distance is equal to the original beam charge, and the electric field is virtually the same as the electric field of a pulse traveling in a vacuum.

Discussion

Equations (2-25), (2-26), and (2-20), along with the boundary conditions and conductivity generation equations to be presented in Section IV, form a complete set, and

are the equations that the numerical program, BEAM1, solve. Numerical solution of these equations has two advantages over numerical solutions to the unaltered form of Maxwell's equation. Firstly, by transforming to a system where the fields are independent of time, program execution time is greatly reduced. Secondly, by ignoring the axial displacement current density a differential equation for the axial field is derived whose finite difference equation can be made linearly stable. We gain these advantages without a perceptible loss in accuracy, as evidenced by the good agreement with experimental data.

These field equations, as they stand, are independent of pulse shape. We can, however, considerably simplify this set of equations by assuming a particular radial variation of the pulse particle density, and the conductivity. This leads to the one-dimensional model.

III. ONE-DIMENSIONAL MODEL OF THE EM FIELDS

Introduction

In the last section we derived a set of equations for the electric and magnetic fields that retained the axial and the radial variations of the fields. In this section we make additional assumptions to derive a set of differential equations that retain only an axial variation. Radial dependence is eliminated from the differential equations of the previous section by approximating the variations with analytic functions. The one-dimensional model we derive here has two important advantages. Firstly, computer execution time for the one-dimensional model is reduced by a factor of 50 below that of the execution time for solving the two-dimensional equations. Secondly, the charge neutralization and current saturation times appear explicitly in the one-dimensional equations, allowing a more direct insight into the behavior of the EM fields.

The remainder of this section is split into four parts. In the first part we specify the principal assumptions that are used in developing the model equations. The second part is devoted to deriving the one-dimensional equations from the two-dimensional equations. In the

third part we compare Johnston's original circuit equation with an analagous equation we derive from the one-dimensional model equations. The last part of this section is devoted to a discussion of the model equations.

Principal Assumptions

Listed here are the assumptions that are made to derive the one-dimensional model equations from the two-dimensional model equations of the previous section.

1. Since our starting point in this derivation is the two-dimensional model, all of the assumptions of that model, which are listed in the previous section, are encompassed here.

2. We assume that the plasma current density is given by Ohm's law,

$$\vec{J}_p = \Sigma \vec{E} \quad (3-1)$$

where the conductivity is a scalar quantity, rather than a tensor quantity. In Appendix B we show that Ohm's law holds as long as the momentum-transfer collision time is shorter than any other time of interest. At a pressure of five Torr this collision time is less than 10^{-10} seconds, and is shorter than the charge neutralization time, the shortest time of interest for the purposes of this work. Since the collision time varies inversely with pressure, Ohm's law is valid for pressures of five Torr and above.

3. The radial variation of both the beam electron density and the conductivity are assumed to vary in a Bennett fashion. This variation is given by

$$f(r) = (1 + r^2/a^2)^{-2} \quad (3-2)$$

This radial dependence for the beam density is chosen since this dependence is observed as the actual variation achieved by an electron beam propagating through a neutral gas (Ref 27). The conductivity will closely follow the beam current density whenever direct ionization dominates over avalanche ionization. At low pressures (less than 100 Torr) and in the pulse rise portion, avalanche ionization dominates over direct ionization and the radial variation of the conductivity can then deviate from a Bennett profile. We do not take this deviation into account.

Derivation of Model Equations

From the previous section we have already derived an equation for the radial field which is independent of r . It is

$$\frac{\partial E_r}{\partial \tau} + 4\pi J_{pr} = \frac{\partial E_r^o}{\partial \tau} \quad (2-16)$$

Using Ohm's law,

$$\frac{\partial E_r}{\partial \tau} + 4\pi \Sigma E_r = \frac{\partial E_r^0}{\partial \tau} \quad (3-3)$$

This is the radial electric field equation of the one-dimensional model. The formal solution is

$$E_r = \int_0^{\tau} \frac{\partial E_r^0}{\partial \tau'} \exp(-4\pi \int_0^{\tau} \Sigma d\tau'') d\tau' \quad (3-4)$$

or, integrating by parts,

$$E_r = E_r^0 - \int_0^{\tau} 4\pi \Sigma E_r^0 \exp(-4\pi \int_0^{\tau} \Sigma d\tau'') d\tau' \quad (3-5)$$

Equation (3-5) clearly expresses the decay of the radial field with increasing conductivity.

We now turn our attention to the more difficult task of simplifying the equation for the axial electric field of the previous section,

$$\frac{1}{r} \frac{\partial}{\partial r} \left[r \left(\frac{\partial E_z}{\partial r} + \frac{1}{\beta c} \frac{\partial E_r}{\partial \tau} \right) \right] = \frac{4\pi}{c^2} \frac{\partial}{\partial \tau} (J_{bz} + J_{pz}) \quad (2-27)$$

Our method is to integrate over r and use Ohm's law to obtain an integro-differential equation for J_{pz} . By performing the integration over r in an approximate manner we

obtain a differential equation in τ for J_{pz} . Integrating over r ,

$$E_z = \frac{4\pi}{c^2} \frac{\partial}{\partial \tau} \int_b^r \frac{dr'}{r'} \int_0^{r'} (J_{bz} + J_{pz}) r'' dr'' - \frac{1}{\beta c} \frac{\partial}{\partial \tau} \int_b^r E_r dr' \quad (3-6)$$

where we have used the conditions,

$$\left. \frac{\partial E_z}{\partial r} \right|_{r=0} = 0 \quad (3-7)$$

$$E_z (r=b) = 0 \quad (3-8)$$

$$E_r (r=0) = 0 \quad (3-9)$$

The parameter, b , is used as the radial position where E_z changes sign. We interpret this as the position of the charge sheath, the sheath being built up by plasma electrons ejected from the beam by the radial electric field. We will later show how to estimate the sheath position.

Multiplying both sides of equation (3-6) by the conductivity, we have

$$J_{pz} = \frac{4\pi \Sigma}{c^2} \frac{\partial}{\partial \tau} \int_b^r \frac{dr'}{r'} \int_0^{r'} (J_{bz} + J_{pz}) r'' dr'' - \frac{\Sigma}{\beta c} \frac{\partial}{\partial \tau} \int_b^r E_r dr' \quad (3-10)$$

In order to perform the integration over the current density we assume,

$$\Sigma = \Sigma_0 f(r) \quad (3-11)$$

$$J_{bz} = J_{bzo} f(r) \quad (3-12)$$

$$J_{pz} = J_{pzo} f(r) \quad (3-13)$$

where the zero subscript denotes the on-axis values of the variables, and $f(r)$ is given by (3-2). We have, approximately,

$$J_{pz} = -\frac{\pi a^2}{c^2} \Sigma_0 f(r) G(r) \frac{\partial}{\partial \tau} (J_{bzo} + J_{pzo}) - \frac{\Sigma_0}{\beta c} f(r) \frac{\partial}{\partial \tau} \int_b^r E_r dr' \quad (3-14)$$

where

$$G(r) = \ln \left(\frac{1+b^2/a^2}{1+r^2/a^2} \right) \quad (3-15)$$

So that the integration over E_r in (3-10) can be carried out we make the approximation that the radial field follows the radial variation of that field for a pulse traveling in a vacuum. From Appendix A,

$$E_r^{\circ}(r) = 2\pi\rho^{\circ}r/(1+r^2/a^2) \quad (3-16)$$

or

$$E_r^{\circ}(r) = 2E_r^{\circ}(a)ra/(r^2+a^2) \quad (3-17)$$

Thus, we approximate the radial variation of E_r by

$$E_r(r) = 2E_r(a)\frac{ra}{r^2+a^2} \quad (3-18)$$

where $E_r^{\circ}(a)$ and $E_r(a)$ are the radial fields at the Bennett radius for a beam in a vacuum, and in air, respectively. This approximate radial dependence is obviously not exact since the conductivity in (3-4) is a function of the radial variable; but, since we integrate over the radial variable the specific radial dependence is of secondary importance. Thus

$$\int_b^r E_r(r)dr' = aG(r)E_r(a) \quad (3-19)$$

and

$$J_{pz} = J_{pzo} h(r) = f(r)G(r) \left[-\frac{\pi a^2 \Sigma_o}{c^2} \frac{\partial}{\partial \tau} (J_{bzo} + J_{pzo}) \right] \quad (3-20)$$

$$+ \frac{\Sigma_o a}{\beta c} \frac{\partial E_r(a)}{\partial \tau}$$

After normalizing to insure that $h(0)=1$, we have the approximate radial variation of the plasma current density,

$$h(r) = [1 - \ln(1+r^2/a^2) / \ln(1+b^2/a^2)] (1+r^2/a^2)^{-2} \quad (3-21)$$

and the equation for J_{pzo} in τ ,

$$\frac{\partial J_{pzo}}{\partial \tau} + \frac{J_{pzo}}{\tau_m} = -\frac{\partial J_{bzo}}{\partial \tau} + \frac{c}{\pi a \beta} \frac{\partial E_r(a)}{\partial \tau} \quad (3-22)$$

where

$$\tau_m = \frac{\pi a^2 \Sigma_0 \ln(1+b^2/a^2)}{c^2} \quad (3-23)$$

The parameter, τ_m , is the magnetic diffusion time for a cylindrical pulse with the Bennett profile, propagating through air.

Once $E_r(a)$ and J_{pzo} are calculated the rest of the fields are simply found. The axial field is found from Ohm's law

$$E_z = J_{pz} / \Sigma \quad (3-24)$$

The magnetic field is found by direct integration to be

$$B_\theta = \frac{2I_b(r)}{cr} + \frac{2I_p(r)}{cr} \quad (3-25)$$

where

$$I_b(r) = \frac{\pi r^2 J_{bz0}}{1+r^2/a^2} \quad (3-26)$$

$$I_p(r) = \frac{\pi r^2 J_{pz0}}{1+r^2/a^2} \left\{ 1 - \frac{[1-(a^2/r^2)\ln(1+r^2/a^2)]}{\ln(1+b^2/a^2)} \right\} \quad (3-27)$$

$I_b(r)$ and $I_p(r)$ are the beam and plasma currents, respectively, contained inside the cylinder of radius r .

We are left with determining the position of the charge sheath, b . Results from the two-dimensional model show b to be near the radial position where the radial field reaches its maximum. We approximate this position from the charge neutralization time,

$$4\pi\Sigma(\tau,r)\tau=1 \quad (3-28)$$

$$\frac{4\pi\Sigma_o(\tau)\tau}{(1+b^2/a^2)^2} = 1 \quad (3-29)$$

and

$$\frac{b}{a} = [(4\pi\Sigma_o(\tau)\tau)^{1/2} - 1]^{1/2} \quad (3-30)$$

Comparison with the Circuit Equation

It is instructive to compare Johnston's circuit

equation (Ref 11) with an analogous equation that we derive here. Solving (3-22) for the axial field, we have

$$E_{z0} = - \frac{\ln(1+b^2/a^2)}{c^2} \frac{\partial}{\partial \tau} \left[I - \frac{ca}{\beta} E_r(a) \right] \quad (3-31)$$

To arrive at this equation we assume that

$$I_p = \pi a^2 J_{pz0}$$

Compare this with equation (1-4),

$$E_z = -L \frac{\partial I}{\partial \tau} \quad (3-32)$$

The parameter, L , is the effective inductance, assumed to be on the order of $2/c^2$. Thus, we improve upon the original circuit equation in three ways. Firstly, we include a term for the radial electric field. Secondly, we obtain a more accurate estimate of the inductance, L , and thirdly, in the course of deriving the one-dimensional model equations we analytically estimate the radial dependence of the fields. Consequently, we include all pertinent phenomena in equation (3-22).

Discussion

In this section we have substantially reduced the complexity of the field equations of the previous section

by integrating out the explicit dependence of the radial variable in the axial field equation. We only do this in an approximate fashion, so the radial variation of the fields are less accurately described by the one-dimensional model. We list here the primary equations of the one-dimensional model

$$\frac{\partial E_r}{\partial \tau} + 4\pi \Sigma E_r = \frac{\partial E_r^o}{\partial \tau} \quad (3-3)$$

$$\frac{\partial J_{pzo}}{\partial \tau} + \frac{J_{pzo}}{\tau_m} = - \frac{\partial J_{bzo}}{\partial \tau} + \frac{c}{\pi a \beta} \frac{\partial E_r(a)}{\partial \tau} \quad (3-22)$$

These two equations are solved by program BEAM2. The magnetic field is evaluated algebraically from equation (3-26).

A qualitative description of the fields is afforded by observing the formal solutions to the primary equations,

$$E_r = \int_0^{\tau} \frac{\partial E_r^o}{\partial \tau'} \exp(-4\pi \int_{\tau'}^{\tau} \Sigma d\tau'') d\tau' \quad (3-4)$$

and

$$J_{pzo} = - \int_0^{\tau} \left(\frac{\partial J_{bzo}}{\partial \tau'} - \frac{c}{\pi a \beta} \frac{\partial E_r(a)}{\partial \tau'} \right) \exp\left(-\int_{\tau'}^{\tau} \frac{d\tau''}{\tau_m}\right) d\tau' \quad (3-33)$$

These two solutions are formally similar, but E_r and J_{pzo} show quite different detail. As conductivity increases it reaches a value that is so large that the radial electric fields is actually "shorted out", and decays away. A close estimate of when that value of conductivity is reached is given by

$$4\pi \int_0^{\tau} \Sigma(\tau') d\tau' = 1 \quad (3-34)$$

We make the further approximation,

$$4\pi \int_0^{\tau} \Sigma(\tau') d\tau' = 4\pi \Sigma(\tau) \tau = 1 \quad (3-35)$$

Consequently, we define the charge neutralization time from (3-35) by solving for τ ,

$$\tau_c = \frac{1}{4\pi \Sigma(\tau_c)} \quad (1-2)$$

On the other hand, as conductivity increases, the plasma current is seen to increase in the pulse rise portion. Once the conductivity has reached a sufficiently high value we reach the condition,

$$\frac{\partial J_{pzo}}{\partial \tau} = - \frac{\partial J_{bzo}}{\partial \tau} \quad (3-36)$$

Beyond this point the net current, and the magnetic field, cease to increase, and they are said to be "frozen" into the plasma. From (3-34) we estimate that this condition occurs when

$$\frac{\tau_m(\tau)}{\tau} = 1 \quad (3-37)$$

Solving this, we define the current saturation time,

$$\tau_I = \tau_m(\tau_I) = \frac{\pi a^2 \Sigma_o(\tau_I) \ln(1+b^2(\tau_I)/a^2)}{c^2} \quad (3-38)$$

Although we clearly see that the current saturation time depends upon the parameter, b , a useful approximation is

$$\ln(1+b^2/a^2) = 4$$

so that we derive an approximate form of the current saturation time,

$$\tau_I = \frac{4\pi a^2 \Sigma_o(\tau_I)}{c^2} \quad (1-3)$$

Again, we have left the conductivity unspecified. It is apparent from this discussion that the conductivity plays the critical role in the behavior of the fields. In the next section we describe a model for ionization and conductivity generation.

IV. IONIZATION MODEL

Introduction

Past sections are devoted to developing models for the electric and magnetic self-fields of a pulse of relativistic electrons propagating through air. Up to this point all terms in the field equations have been specified except for the plasma current and conductivity. Here, in this section, we specify those remaining parameters by presenting a model for the production of plasma electrons. Due to the large number of air reactions and their complex nature it is not possible to specify perfectly the charge state of the air. Indeed, some of the reaction cross sections, including cascade ionization, are not accurately known.

The model we present here was originally developed by Wittwer (Ref 19) for high altitude EMP studies. It is a fluid description of the plasma electrons with empirically determined reaction rates. We have modified the model for our purposes to include electron-ion recombination, electron-ion and electron-electron collisions, the cascade ionization time lag, and neutral gas heating. It is the only model in which all important reactions are included. Consequently we believe it is the most accurate descrip-

tion available over the pressure range of interest in this study.

This section is split into several different parts. In the first part the kinetic terms in the fluid equations are derived from the Boltzmann-Vlasov equation. In the next part we enumerate the assumptions employed in the ionization model, and in the following part the resulting equations of the model are listed. The following part is devoted to a discussion of the cascade ionization time lag and a derivation of the lag term employed in the ionization model. In the last part we discuss the importance of the model, and, as an example, we analytically estimate the saturation value of the net current.

Derivation of Fluid Equations

Our starting point for the derivation of the fluid equations is the equation of transport,

$$\frac{df}{dt} \text{ kinetic} = \frac{\delta f}{\delta t} \text{ collisions} \quad (4-1)$$

with

$$\frac{df}{dt} \text{ kinetic} = \frac{\partial f}{\partial t} + \vec{u} \cdot \vec{\nabla}_r f + \vec{a} \cdot \vec{\nabla}_u f \quad (4-2)$$

and

$$f = \frac{d^6 n}{dx dy dz du_x du_y du_z} \quad (4-3)$$

n = total number of plasma electrons

$$\vec{a} = \frac{e}{m} (\vec{E} + \frac{\vec{u}}{c} \times \vec{B}) \quad (4-4)$$

$$\vec{\nabla}_r = \hat{e}_x \frac{\partial}{\partial x} + \hat{e}_y \frac{\partial}{\partial y} + \hat{e}_z \frac{\partial}{\partial z} \quad (4-5)$$

$$\vec{\nabla}_u = \hat{e}_{u_x} \frac{\partial}{\partial u_x} + \hat{e}_{u_y} \frac{\partial}{\partial u_y} + \hat{e}_{u_z} \frac{\partial}{\partial u_z} \quad (4-6)$$

Del operators are expressed in the Cartesian coordinate system for convenience. All of the plasma electron fluid equations are derived by multiplying each term in (4-1) by $(\vec{u})^n$, where $n = 0, 1, 2$, and integrating over all velocity space.

For some Q ,

$$\int_{-\infty}^{\infty} Q \frac{df}{dt} \text{ kinetic } d\vec{u} = \frac{\partial}{\partial t} (n_e \langle Q \rangle) + \vec{\nabla}_r \cdot (n_e \langle Q \vec{u} \rangle) - n_e \langle \vec{a} \cdot \vec{\nabla}_u Q \rangle = \int_{-\infty}^{\infty} Q \frac{\delta f}{\delta t} \text{ collisions } d\vec{u} \quad (4-7)$$

where

$$n_e = \int_{-\infty}^{\infty} f d\vec{u} \quad (4-8)$$

and

$$\langle \rangle = \frac{1}{n_e} \int_{-\infty}^{\infty} \langle \rangle f d\vec{u} \quad (4-9)$$

Let

$$Q = 1$$

$$\vec{v} = \langle \vec{u} \rangle$$

then

$$\frac{\partial n_e}{\partial t} + \vec{\nabla} \cdot n_e \vec{v} = n_e \int_{-\infty}^{\infty} \frac{\delta f}{\delta t} \text{ collisions } d\vec{u} \quad (4-10)$$

The subscript, r , in the ∇ operator has been dropped for convenience. Equation (4-10) is immediately recognized as the continuity equation.

Now let

$$Q = \vec{u}$$

then

$$\begin{aligned} \frac{\partial}{\partial t} (n_e \vec{v}) + \vec{\nabla} \cdot (n_e \langle \vec{u}\vec{u} \rangle) - n_e \frac{e}{m} (\vec{E} + \frac{\vec{v}}{c} \times \vec{B}) \\ = n_e \int_{-\infty}^{\infty} \vec{u} \frac{\delta f}{\delta t} \text{ collisions } d\vec{u} \end{aligned} \quad (4-11)$$

To put this equation into a more recognizable form define

$$\vec{u} = \vec{v} + \vec{w} \quad (4-12)$$

where \vec{w} is the departure of \vec{u} from its average, \vec{v} . Then

$$\begin{aligned} \vec{\nabla} \cdot (n_e \langle \vec{u}\vec{u} \rangle) &= \vec{\nabla} \cdot n_e (\langle (\vec{v} + \vec{w})(\vec{v} + \vec{w}) \rangle) \\ &= \vec{\nabla} \cdot (n_e \vec{v}\vec{v}) + \vec{\nabla} \cdot (n_e \langle \vec{w}\vec{w} \rangle) \end{aligned} \quad (4-13)$$

since $\langle \vec{w} \rangle = 0$. Additionally,

$$\vec{\nabla} \cdot (n_e \vec{v}\vec{v}) = n_e (\vec{v} \cdot \vec{\nabla}) \vec{v} + \vec{v} (\vec{\nabla} \cdot n_e \vec{v}) \quad (4-14)$$

Therefore, equation (4-11) becomes

$$\begin{aligned} n_e \frac{\partial \vec{v}}{\partial t} + \vec{v} \left[\frac{\partial n_e}{\partial t} + \vec{\nabla} \cdot (n_e \vec{v}) \right] + n_e (\vec{v} \cdot \vec{\nabla}) \vec{v} \\ + \frac{1}{m} \vec{\nabla} \cdot \vec{P} = n_e \frac{e}{m} (\vec{E} + \frac{\vec{v}}{c} \times \vec{B}) + \int_{-\infty}^{\infty} \vec{u} \frac{\delta f}{\delta t} \text{ collisions } d\vec{u} \end{aligned}$$

or, employing (4-10) and dividing by n_e ,

$$\frac{\partial \vec{v}}{\partial t} + (\vec{v} \cdot \nabla) \vec{v} + \frac{1}{mn_e} \nabla \cdot \vec{P} = \frac{e}{m} (\vec{E} + \frac{\vec{v}}{c} \times \vec{B})$$

$$-\frac{\vec{v}}{n_e} \int_{-\infty}^{\infty} \frac{\delta f}{\delta t} \text{ collisions } d\vec{u} + \frac{1}{n_e} \int_{-\infty}^{\infty} \vec{u} \frac{\delta f}{\delta t} \text{ collisions } d\vec{u} \quad (4-15)$$

Here we have defined $\vec{P} = mn_e \langle \vec{w}\vec{w} \rangle$. It is the pressure tensor. Equation (4-15) is the momentum conservation equation.

To arrive at the energy conservation equation let

$$Q = \frac{1}{2} mu^2$$

then

$$\frac{\partial}{\partial t} (n_e \langle \frac{1}{2} m u^2 \rangle) + \nabla \cdot (n_e \langle \frac{1}{2} mu^2 \vec{u} \rangle)$$

$$-n_e \frac{e}{m} (\vec{E} + \frac{\vec{v}}{c} \times \vec{B}) \cdot \nabla_u (\frac{1}{2} mu^2) = \int_{-\infty}^{\infty} \frac{1}{2} mu^2 \frac{\delta f}{\delta t} \text{ collisions } d\vec{u} \quad (4-16)$$

Again using (4-12) to arrange terms in a familiar fashion, we have

equations to arrive at the particular equations of the ionization model.

1. Ions are assumed to be immobile. Considering either a collisionless or a collisional plasma the ratio of the ion current density to the electron current density scales either as $\frac{m_e}{m_i}$ or $(\frac{m_e}{m_i})^{1/2}$, where m_e is the electron mass and m_i is the ionic mass. In either case the ratio is less than one percent implying that the ionic current is ignorable. This has no bearing on the fluid equations of the beam electrons, but it does mean that the plasma current is carried entirely by the plasma electrons.

2. We make the cold plasma approximation. Thus, in equation (4-17), $I \ll W$ and \vec{q} is set equal to zero. In equation (4-16), the pressure tensor, \vec{P}^+ , is ignored.

3. All spatial gradients in the fluid equations are ignored. Because the plasma is highly collisional, electron drift velocities are small, and the migration distance for a plasma electron is a small fraction of the beam radius, so large gradients of the plasma electron density, and associated parameters, are not present. Results from the numerical program, BEAM1, are consistent with this assumption.

4. Ionization by Bremsstrahlung radiation is not included. For beam electron energies in the range of one to 10 MeV, the ratio of energy lost by the beam electrons via Bremsstrahlung radiation to energy lost via inelastic collisions, is less than 10%. Even if the Bremsstrahlung

radiation remained localized in the beam and converted a substantial fraction of its energy to producing electron-ion pairs, the ionization from Bremsstrahlung would be less than 10% of that produced from inelastic collisions.

5. The negative ion density is ignored. This allows us to use a single species model, consisting only of the plasma electrons, rather than a three species model, consisting of the plasma electrons and positive and negative ions. In Appendix B we show that the negative ion density is always less than 10% of the plasma electron density.

6. The attachment rate is assumed to be independent of the water vapor concentration. This is incorrect, but at this time the actual dependence of the rate on the amount of water is unclear (Ref 28), so we restrict our calculations to dry air. At altitudes higher than sea level the water vapor pressure is greatly reduced so its influence on the electron population is diminished.

7. Thermal conduction on beam time scales ($<10^{-7}$ seconds) are ignored since the thermal conduction speed is quite low. The thermal conduction speed is limited by the speed of sound, so the characteristic time for heat conduction is limited by a/v_s , where a is the beam radius and v_s is the sound speed. Assuming a beam radius of one centimeter and a sound speed of 5×10^4 cm/sec, the thermal conduction time is greater than 2×10^{-5} seconds, considerably longer than the characteristic pulse length.

8. Radiative energy losses by the plasma electrons are ignored, so the only plasma electron cooling methods considered are elastic and inelastic collisions. There are two major sources for radiation by plasma electrons, Bremsstrahlung and line radiation. The rate of Bremsstrahlung generation from plasma electrons impacting neutral air molecules is considerably less than that produced by plasma electrons impacting ions (Ref 29). Thus, the energy loss rate of plasma electrons by Bremsstrahlung is very much less than (Ref 30)

$$\frac{dW_B}{dt} \ll \frac{16}{3} \frac{NZ^2e^6}{\hbar m_0 c^3} w$$

where $\frac{dW_B}{dt}$ is the Bremsstrahlung energy production rate for fully ionized air molecules, N is the molecular density, Z is the ionic charge, and w is the plasma electron thermal speed. For sea level conditions and a plasma electron thermal energy of one eV, we have $\frac{dW_B}{dt} \ll 7 \times 10^8$ eV/sec. This rate is much less than the collisional cooling rate which is 1×10^{10} eV/sec (Appendix B). The intensity of line radiation is estimated from experimental measurements (Ref 31) to be less than 3×10^3 Watts/cm³ at sea level conditions for a 10 kA/cm^2 beam, and a calculated electron density of $1 \times 10^{16} \text{ cm}^{-3}$. This implies a bound on the electron cooling rate from the line radiation of 2×10^6 eV/sec, again much less than the collisional cooling rate.

9. We ignore the magnetic force on the plasma electrons. The conductivity tensor is,

$$\vec{\Sigma} = \frac{e^2 n_e}{m v_m} \frac{v_m^2}{v_m^2 - w_c^2} \begin{pmatrix} 1 & w_c/v_m \\ w_c/v_m & 1 \end{pmatrix}$$

where $w_c = \frac{eB_\theta}{mc}$, and is the cyclotron frequency of plasma electrons in the azimuthal magnetic field, B_θ . Thus, we assume that $w_c \ll v_m$, and the conductivity assumes the scalar form. However, below an air pressure of 50 Torr the cyclotron frequency can reach a value which is a significant fraction of the collision frequency, and will approach the value of the collision frequency at 5 Torr. We ignore this effect.

10. We adopt Wittwer's collisional terms (Ref 19). This requires a weakly ionized plasma, $n_e \ll N$, where N is the molecular gas density.

$$a. \int_{-\infty}^{\infty} \frac{\delta f}{\delta t} d\vec{u} = R + \alpha n_e \quad (4-18)$$

where R is the direct ionization rate and αn_e is the avalanche (attachment) rate. The parameter, α , is the avalanche coefficient minus the attachment coefficient.

$$b. \frac{1}{n_e} \int_{-\infty}^{\infty} \vec{u} \frac{\delta f}{\delta t} d\vec{u} = -v_m \vec{v} \quad (4-19)$$

where ν_m is the momentum transfer collision frequency.

$$c. \quad \frac{1}{n_e} \int_{-\infty}^{\infty} \left(\frac{1}{2} m u^2 \right) \frac{\delta f}{\delta t} d\vec{u} = -\nu_e (W - \epsilon) \quad (4-20)$$

Here ν_e is the energy transfer collision frequency and ϵ is the neutral gas energy.

12. We modify Wittwer's model in the following ways:

a. Electron-ion recombination is added.

Recombination plays a crucial role at atmospheric pressure by causing the plasma density to saturate. The recombination term to be added is

$$-\beta_r n_e^2$$

where β_r is the electron-ion recombination coefficient.

b. An electron-ion (Spitzer, Ref 32) collision frequency is added. Normally, this collision frequency is less than 10% of the electron-neutral collision frequency at atmospheric pressure, but can be greater at low air pressures.

c. We include an equation for the neutral gas energy, ϵ . Considerable heating of the neutral gas by the beam can take place resulting in a lower energy exchange rate and a higher electron energy, thereby changing the reaction rates that are functions of electron energy. The equation is

$$\frac{\partial \epsilon}{\partial t} = f \frac{dT}{dt} + \frac{n_e}{N} v_e (W - \epsilon) \quad (4-21)$$

where

$N = 2.7 \times 10^{19}$ molecules/cm³, and is the sea level molecular air density

$\frac{dT}{dt}$ = energy loss rate of beam electrons

f = fraction of beam deposited energy that goes directly into heating the gas molecules.

13. We include effects of cascade ionization time lag. This is given by

$$R = R_I + R_C \quad (4-22)$$

where R_I is the beam electron impact ionization rate and R_C is the cascade ionization rate. Later in this section we show that the cascade is modeled by

$$R_C = A \int_{\tau_0}^{\tau_l} \frac{R_I(\tau - \tau')}{\tau'} d\tau' \quad (4-23)$$

where τ_0 is the time of the beginning of the ionization cascade, τ_l is the time of the end of the cascade, and A has the numerical value 0.163. The parameter, τ_l , is sometimes called the "lag" time.

Equations of the Ionization Model

With the previously mentioned assumptions the resulting equations of the ionization model are, in the retarded time coordinate system,

$$\frac{\partial n_e}{\partial \tau} = R_I + R_C + \alpha n_e - \beta_r n_e^2 \quad (4-24)$$

$$\frac{\partial v_r}{\partial \tau} = \frac{eE_r}{m} - (v_m + \alpha_T) v_r \quad (4-25)$$

$$\frac{\partial v_z}{\partial \tau} = \frac{eE_z}{m} - (v_m + \alpha_T) v_z \quad (4-26)$$

$$\frac{\partial W}{\partial \tau} = e(E_r v_r + E_z v_z) - v_e (W - \epsilon) - \alpha_T W + S \quad (4-27)$$

$$\frac{\partial \epsilon}{\partial \tau} = f \frac{dT}{dt} + \frac{n_e}{N_n} v_e (W - \epsilon) \quad (4-28)$$

where

$$\alpha_T = \frac{R_I + R_C}{n_e} + \alpha - \beta_r n_e \quad (4-29)$$

and S is the external heating rate. We estimate the heating rate as

$$S = \left(\frac{R_I + R_C}{n_e} \right) Q \quad (4-30)$$

The parameter, Q , is the energy of an electron as it enters the thermal swarm. We choose a value of 7.5 eV for Q to agree with the value used by Johnston (Ref 11). Reaction rates and collision frequencies are compiled and discussed in Appendix B.

Boundary Conditions

Since we ignore all of the spatial gradients of the fluid equations we have only to specify the conditions at $\tau = t - z/\beta c = 0$. The conditions are

$$n_e = 0 \quad (4-31)$$

$$v_r = v_z = 0 \quad (4-32)$$

$$W = 7.5 \text{ eV} \quad (4-33)$$

$$\epsilon = 0.026 \text{ eV} \quad (4-34)$$

The first condition (4-31) arises by assuming that the plasma electron density is zero ahead of the pulse. The second condition (4-32), results from the assertion that the electric fields vanish at $\tau = 0$. The fields generally are not zero at that point, but are so much smaller there

than in the remainder of the pulse that the effects of the fields there are negligible. At $\tau=0$ the low energy electrons just born in the ionization process have had no time to cool, so we give them an energy of 7.5 eV. This is the motivation for the third condition (4-33). This condition, like the external heating rate, has negligible impact upon the electron energy inside the pulse. Finally, (4-34) comes from assuming that the ambient air is at a characteristic temperature of 300°K.

Cascade Ionization

We now turn our attention to deriving the cascade ionization term in the plasma electron production equation (4-24). The term is constructed by an analytic fit to a Monte Carlo simulation of the cascade phenomenon. A discussion of the numerical program that performs the simulation, program MONTY, is found in Appendix E.

When a high energy electron impacts an air molecule, and ionization takes place, the electrons produced can achieve any of a spectrum of possible energies. We illustrate this in Figure 6 with a plot of the differential ionization cross section, $\frac{d\sigma_i}{dQ}$, as a function of secondary electron energy, Q . This cross section is taken from Porter, Jackman, and Green (Ref 12 and Appendix E) and is a theoretical estimate. Other estimates of the differential ionization cross section for relativistic electrons are available (Refs 13, 33) but no experimental measurements

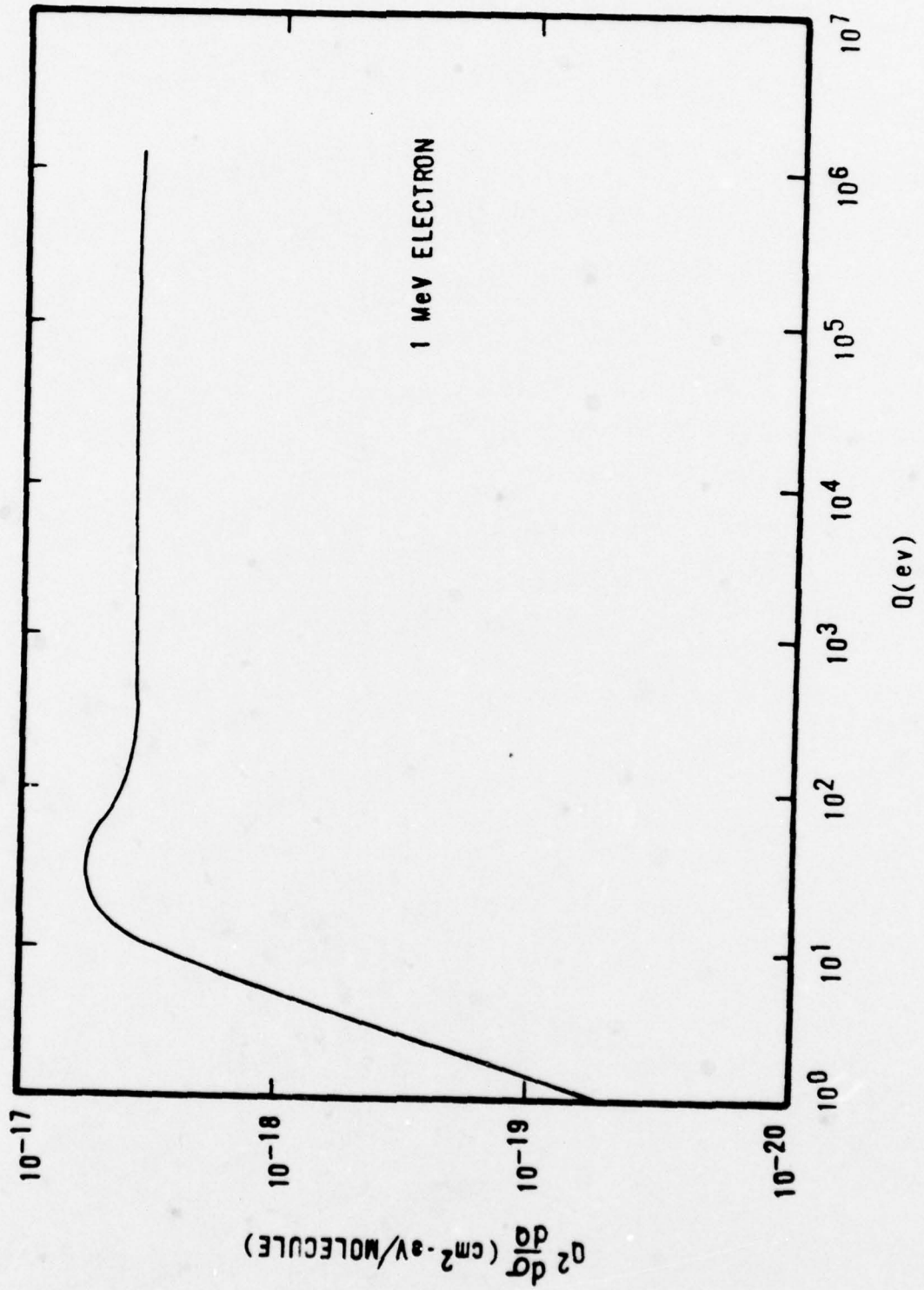


Figure 6. Differential Ionization Cross Section

have been made at relativistic energies (Ref 34). These high energy secondary electrons lose their energy by ionization and excitation of air molecules, producing a cascade of more electrons. For beam electrons in the range of one to 10 MeV, the average energy lost in an inelastic event (ionization or excitation) is 86 eV. This number is taken from the classical electron stopping power formula (Ref 35). It is empirically determined, though, that, after the cascade process is complete, one ion-pair is produced for every 34 eV lost by the beam electron (Ref 36). Thus, for every primary event the total number of electrons produced is $\frac{86}{34} = 2.5$. Consequently, an additional 1.5 electrons is produced in the ionization cascade.

Obviously, the cascade process takes a finite amount of time to be completed. This we illustrate in Figure 7. It is a plot of ionization increase as a function of time produced by a single one MeV electron. There is no applied electric field. The solid curves are results taken from program MONTY with different assumed differential cross sections. Curve A is produced by using the cross section of Porter, Jackman, and Green, while curve B is produced by using the cross section of Longmire and Longley (Ref 13) and curve C is produced with a cross section very similar to that described by Lunn (Ref 33). Curve B' is the original lag calculation performed by Longmire using his assumed cross section (Ref 13). Curve C' is from a calculation performed by Canavan, Brau, and

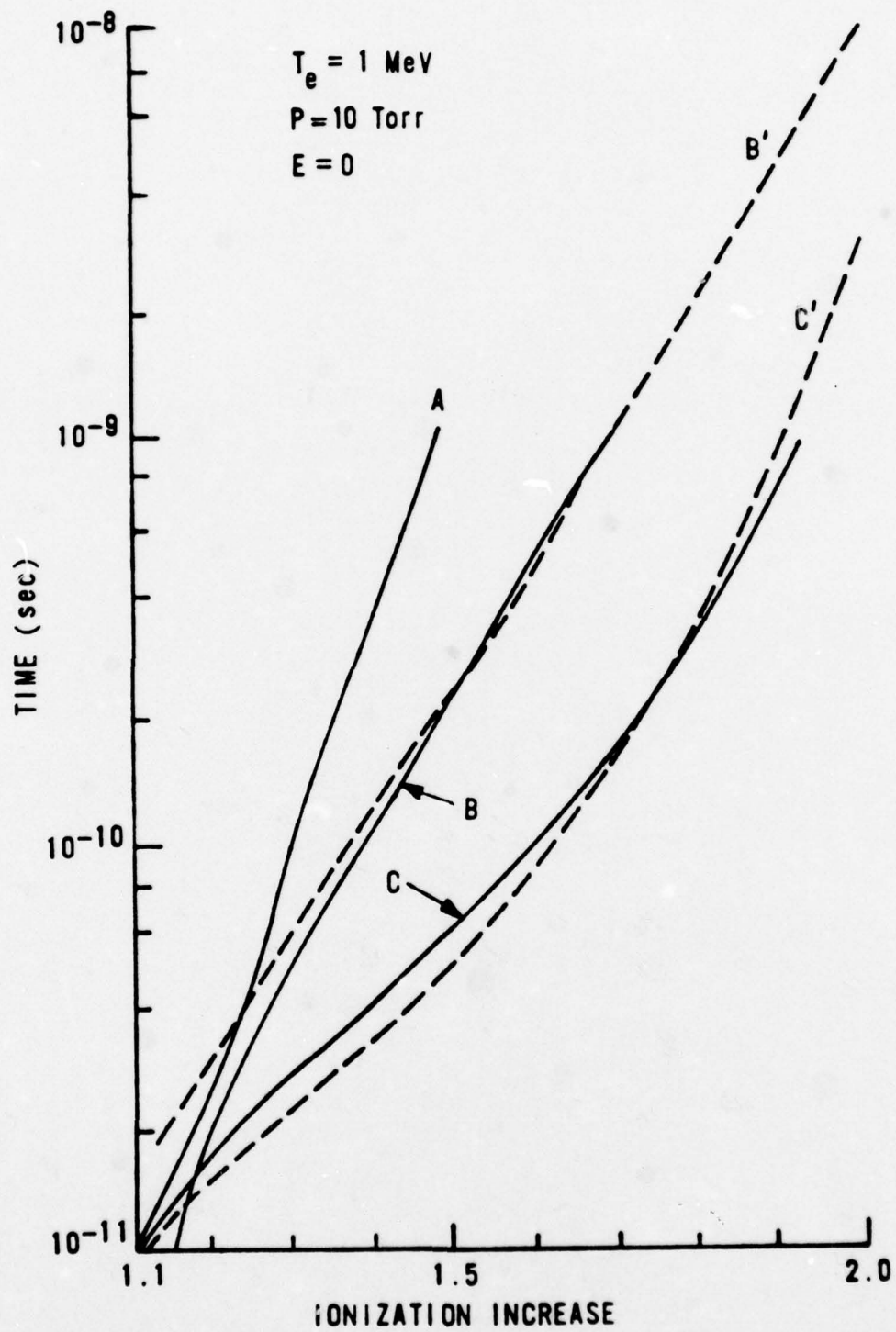


Figure 7. Cascade Ionization Time Lag

Wittwer (Ref 37) assuming the cross section of Lunn. There is little agreement of the calculated ionization increase between the different cross sections. Resolution of this discrepancy will probably have to wait until experimental measurements are available. Noting, though, that the Longmire cross section results in a rough mean ionization increase we use that calculation to find the cascade ionization lag time. Extrapolating out to an increase of 2.5 (end of the cascade) the lag time is 10^{-7} seconds. At atmospheric pressure the corresponding lag time is near 10^{-9} seconds.

With a strong applied D-C electric field the ionization rate increases drastically. This is illustrated in Figure 8. The amount of ionization above the zero field cascade level we attribute to avalanche ionization. That is, some of those electrons with energies below the ionization threshold (about 16 eV for nitrogen) are accelerated to energies above the threshold and greatly add to the zero-field ionization rate. Of course, the zero-field ionization is produced by the secondary electrons created with energies above the ionization threshold.

These observations lead us to an approximate way of including cascade in the ionization model, even for the case of non-zero electric fields. We split the distribution of secondary electrons into two parts. One part is composed of high energy secondary electrons; those electrons still losing energy in the cascade, and the other

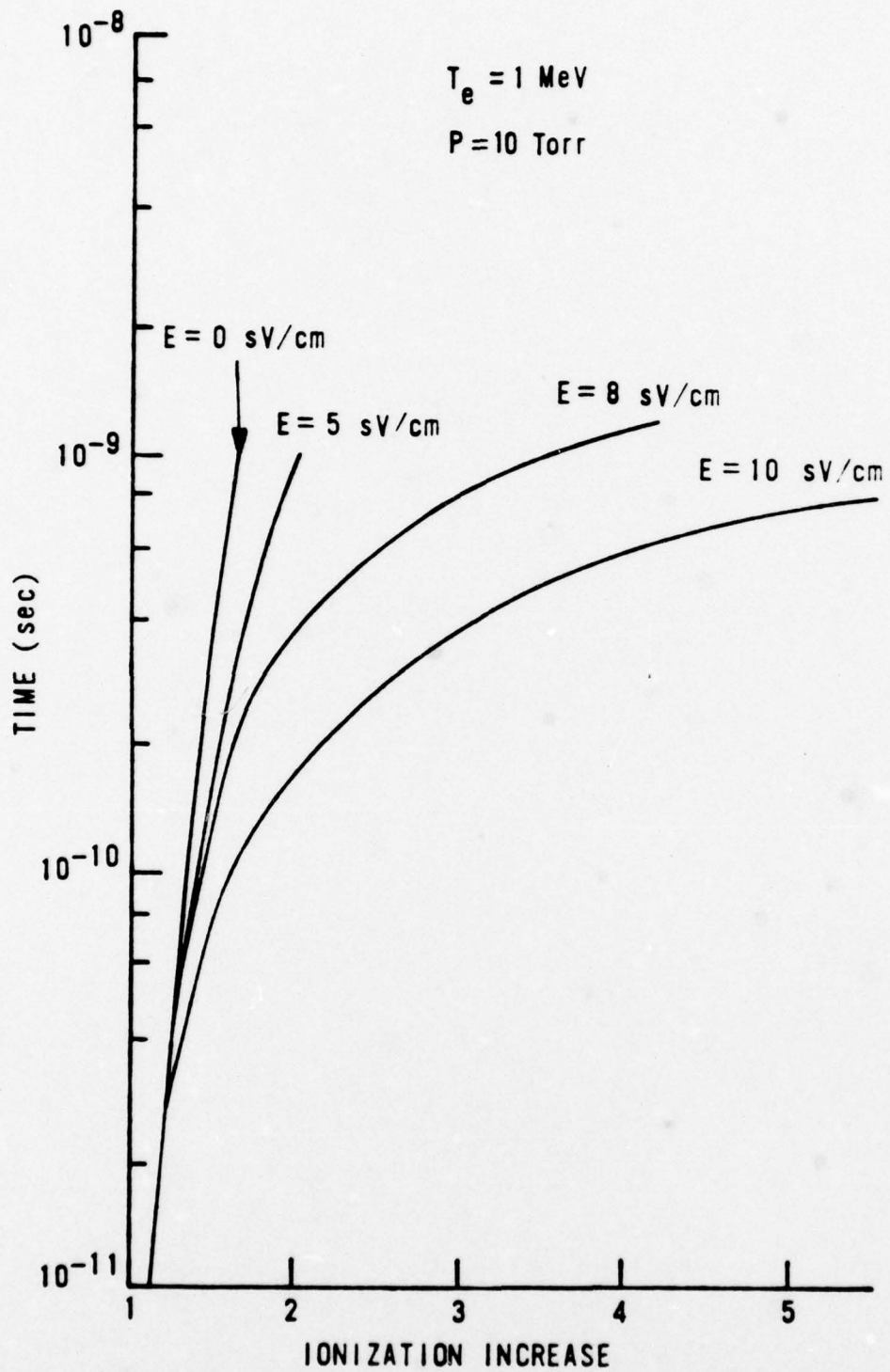


Figure 8. Ionization, Non-Zero Field

part is composed of "thermal" electrons. We use the term "thermal" loosely, but we mean it to include all those secondary electrons that have completed the cascade, and all those electrons produced in the cascade. By doing this the avalanche part of ionization should then be modeled by the avalanche in the electron production equation. We must still model the cascade rate for non-zero fields. We do this simply by assuming that the field does not alter the zero-field cascade rate. This is, of course, incorrect, but if the time is short that the field is on, then the high energy secondary electrons will absorb only an inconsequential amount of energy from the electric field. By estimating the energy absorbed from the electric field we derive a criterion for the validity of this approximation,

$$\Delta t \ll \left(\frac{mQ}{2}\right)^{1/2} / eE \quad (4-35)$$

where Δt is the length of time that the field is on. Choosing $Q = 10$ KeV and $E = 10$ sV/cm we have $\Delta t \ll 1.8 \times 10^{-9}$ seconds. We see that this criterion is not always satisfied for the parameters of this study.

Now let $L(t)$ be the ionization increase produced by the high energy secondary electrons. An analytic fit for the Longmire curve, B' of Figure 7, is

$$L(t) = \begin{cases} 0 & , t < \tau_0 \\ A \ln(t/\tau_0), & \tau_0 < t < \tau_\ell \\ 1.5 & , t > \tau_\ell \end{cases} \quad (4-36)$$

where

$$\tau_\ell = 10^{-9} (p_0/p) \text{ seconds}$$

$$\tau_0 = 10^{-13} (p_0/p) \text{ seconds}$$

$$A = 0.163$$

and p and p_0 are the ambient and sea level atmospheric pressures, respectively. The cascade ionization rate is

$$\frac{\partial L(t)}{\partial t} = \begin{cases} 0 & , t < \tau_0 \\ \frac{A}{t} & , \tau_0 < t < \tau_\ell \\ 0 & , t > \tau_\ell \end{cases} \quad (4-37)$$

Applying the results for a single relativistic electron to a beam of relativistic electrons, we have

$$\frac{\partial R_c}{\partial t} = \begin{cases} 0 & , \tau - t < \tau_0 \\ \frac{AR_I(t)}{\tau - t} & , \tau_0 < \tau - t < \tau_\ell \\ 0 & , \tau - t > \tau_\ell \end{cases} \quad (4-3)$$

Substituting $\tau' = \tau - t$, and integrating, we have

$$R_C = \int_{\tau_0}^{\tau_l} \frac{AR_I(\tau - \tau')}{\tau'} d\tau' \quad (4-23)$$

Discussion

In this section we have presented an ionization model that includes all important phenomena, including cascade ionization. Since this is the only documented model that includes all important effects we believe it is the most accurate representation available of the charge state of the plasma.

Modeling of the plasma is very important because of the dominant role played by the conductivity in determining the behavior of the fields. As an example of the role of conductivity we here make an analytic estimate of the saturation value of the net current flowing in a pulse propagating through air at sea level pressure.

In the previous section we showed that the net current flowing in the rise portion of a pulse tends to saturate whenever the magnetic diffusion time overtakes the time after passage of the front of the pulse. We estimate where this occurs in the pulse rise portion from

$$\tau_I = \frac{4\pi\Sigma(\tau_I)a^2}{c^2} \quad (1-3)$$

We take the conductivity from Appendix B,

$$\Sigma = \frac{e^2 R}{m v_m} \frac{\tau^2}{2 \Delta t} \quad (4-39)$$

This equation is derived for a linearly rising pulse current with rise time Δt . The lag time has been set to zero and avalanching has been ignored. The ionization rate, R , is evaluated at the top of the rise portion and is

$$R = \left(\frac{I_b}{\pi a^2 e \beta c} \right) D \quad (4-40)$$

where

I_b = on-axis beam electron density

$D = 2 \times 10^{12}$ electrons/cm³/sec/beam electron,

and is the beam electron ionization rate. Inserting (4-39)

and (4-40) into (1-3), we have

$$\tau_I = \frac{I_b}{I_s} \frac{\tau_I^2}{\Delta t}$$

or

$$\frac{I_b}{I_s} \frac{\tau_I}{\Delta t} = 1 \quad (4-41)$$

where

$$I_s = \frac{\beta mc^3 v_m}{2eD} \quad (4-42)$$

Choosing a value of $3 \times 10^{12} \text{ sec}^{-1}$ for v_m , we have

$$I_s = 12.8 \text{ KA}$$

The driving mechanism for the plasma current is the rise of the beam current. Then, for saturation to occur, equation (4-41) must be satisfied before the rise of the pulse is completed. Thus, we estimate the minimum beam current required for saturation by letting $\tau_I = \Delta t$. We find that

$$I_b = I_s$$

Therefore, I_s is an estimate of the saturation level of the net current of a pulse propagating at a pressure of one atmosphere. Below atmospheric pressure the saturation current will decrease because avalanche ionization increases at lower pressure causing the conductivity to rise faster. We shall see in the next section that this analytic estimate agrees within a factor of two with the numerical computation.

V. COMPUTATIONAL RESULTS

Introduction

All of the previous sections have been devoted to developing the theory necessary to understand the behavior of the EM fields of a pulse of electrons propagating in air. Considerable time was spent deriving the one- and two-dimensional EM models and the ionization model. The complexity of the resulting equations prohibit analytic solution in all but the simplest cases, so numerical programs were written to solve the equations for more complex cases.

In this section we report on the computational results of these numerical programs. The results demonstrate two major points.

1. The one-dimensional and two-dimensional EM models show basic agreement in the axial variation of the fields. This justifies the simplifying assumptions used in deriving the one-dimensional model equations from the two-dimensional model equations.

2. Results from the computations are in agreement with experimental measurements of plasma electron density and net current over a wide range of parameters.

These two points imply that all important reactions are contained in the ionization model, and that the one-dimensional description of the EM fields is adequate to predict experimentally observed parameters.

This section is split into several parts. In the next part we specify the pulse shape employed in the calculations. Following that we present, in graphical form, typical behavior of the EM fields, and we observe both charge neutralization and current saturation. The next part of this section is devoted to a comparison of the numerical results from the one- and two-dimensional models. Then we compare numerical results from our models to experimental results, and numerical predictions from other authors. In the following part of this section we show that the phenomenon of cascade ionization has virtually no effect upon the calculated fields or the observed net current. In the next part we make a series of net current predictions from the numerical models for beam currents up to 1,000 kilo-Amperes. Finally, we review the results presented and summarize them.

Pulse Shape

For all calculations performed here we assume that the beam charge density is given by,

$$\rho(r,z) = \rho_0 f(r)g(z)$$

where ρ_0 is the on-axis charge density, and

$$f(r) = (1+r^2/a^2)^{-2}$$

$$g(z) = \begin{cases} 0 & , z > 0 \\ -z/\Delta z & , 0 < z < -\Delta z \\ 1 & , -\Delta z < z < -z_0 \\ 0 & , -z_0 < z \end{cases}$$

The parameters Δz , and z_0 , are the rise length of the pulse, and the length of the constant density portion, respectively. Variation in the r direction, $f(r)$, is called the "Bennett" variation. We choose this since it is observed experimentally (Ref 27). The axial variation, $g(z)$, is chosen for its simplicity.

Behavior of Fields

In this part of the section we present results from program BEAM1. This program contains the two-dimensional EM model and the ionization model, so fields in both the axial and radial directions are evaluated. Cascade ionization is not included in BEAM1, but we discuss its effects in a later part of this section.

Typical results from the program for the axial variation of the fields is shown in Figure 9. The charge neutralization time (eq (1-2)) and the current saturation time (eq (1-3)) are indicated on the figure. We see that

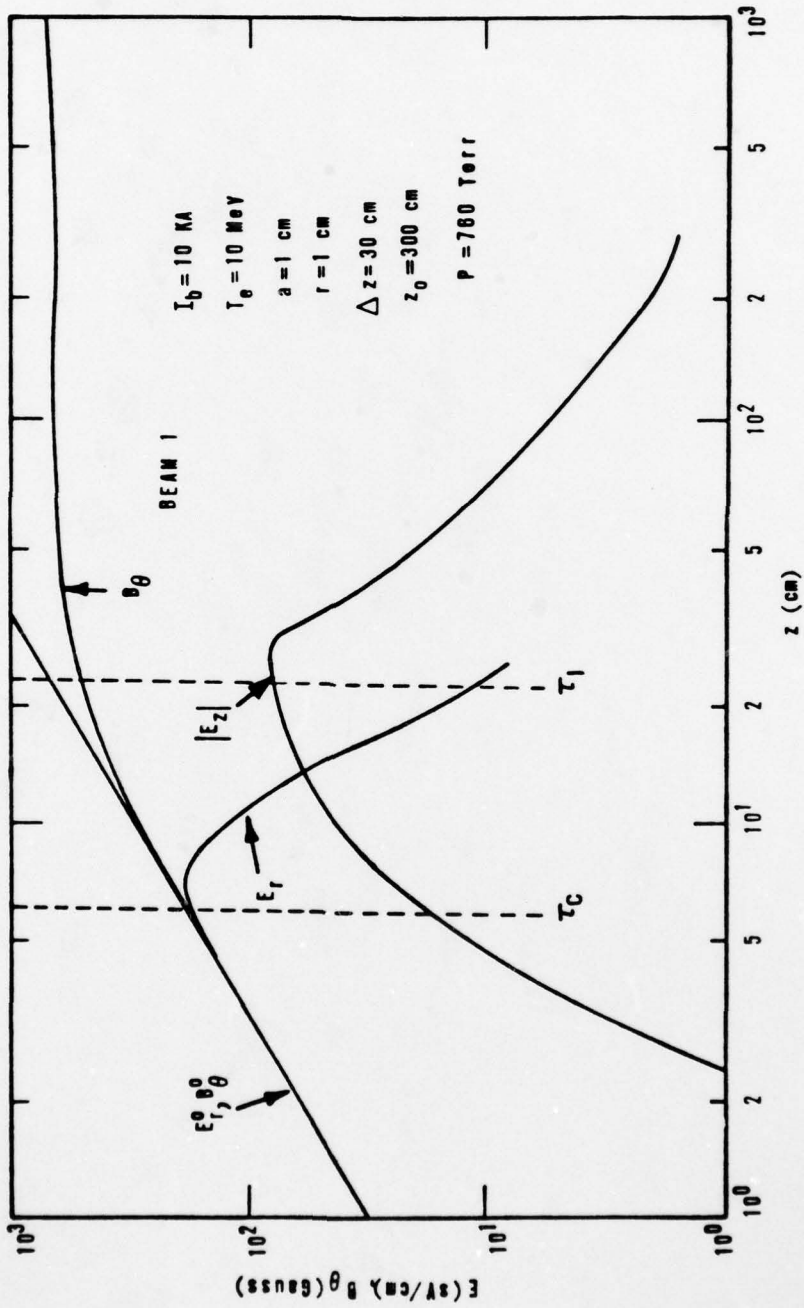


Figure 9. Behavior of Fields

the radial field begins its decay shortly after the charge neutralization time is reached. With the change in the radial electric field from its vacuum value shown as E_r^0 , the axial electric field begins to grow, reaching a maximum at the end of pulse rise. It rapidly decays in the main body of the pulse as the field loses its driving force, the time rate of change of the magnetic field, \dot{B}_θ . We see that the magnetic field ceases its increase near the point where the current saturation time is reached. In this example the net current inferred from the magnetic field is seven kilo-Amperes at the top of the rise portion, and increases to eight kilo-Amperes at the end of the pulse.

Radial variation of the fields is shown in Figures 10, 11, and 12, for three separate distances into the pulse. In Figure 10 we show the radial variation of the radial electric field. These curves are to be compared with the radial variation of the field of a pulse in a vacuum, given by (Appendix A) $\frac{r}{r^2+a^2}$. The most prominent feature of the radial field plots is the "charge neutralization wave" that moves outward as z increases. Since the beam density decreases with increasing r , the ionization rate decreases and the conductivity decreases with increasing r . Thus, the time required to short out, or neutralize, the radial field increases with increasing r . The effect of conductivity change on the axial electric field is shown in Figure 11. We notice that in the pulse

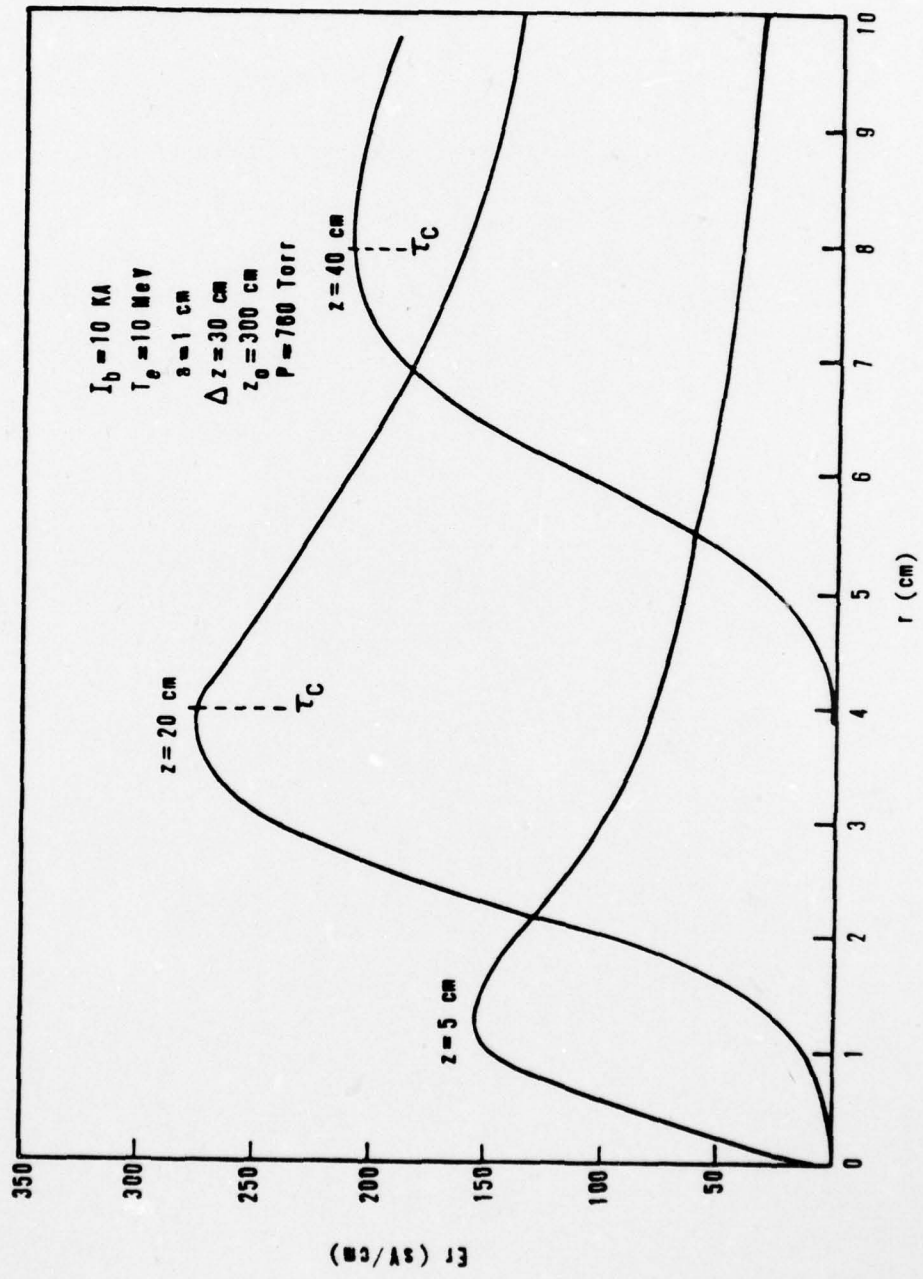


Figure 10. Radial Variation of Radial Electric Field

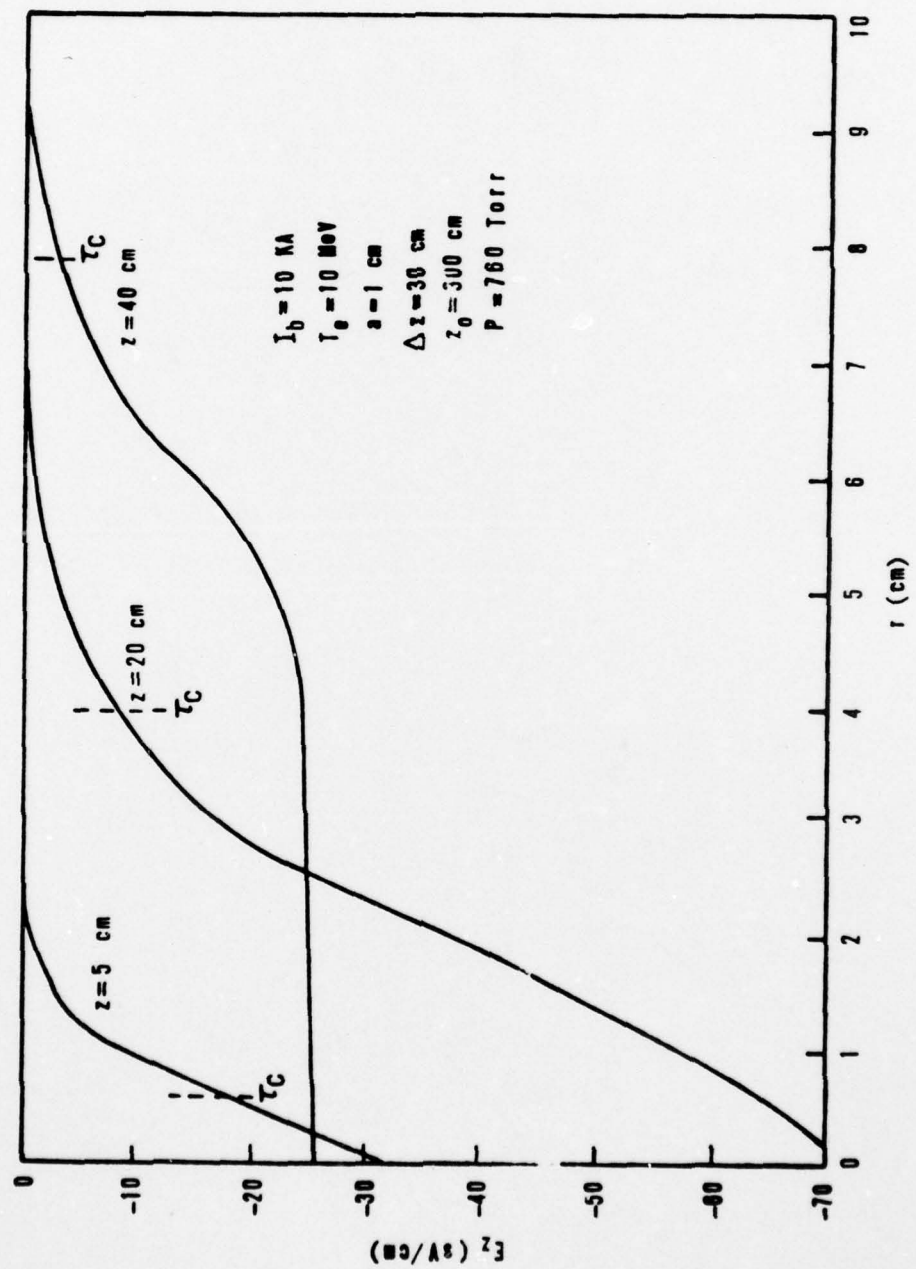


Figure 11. Radial Variation of Axial Electric Field

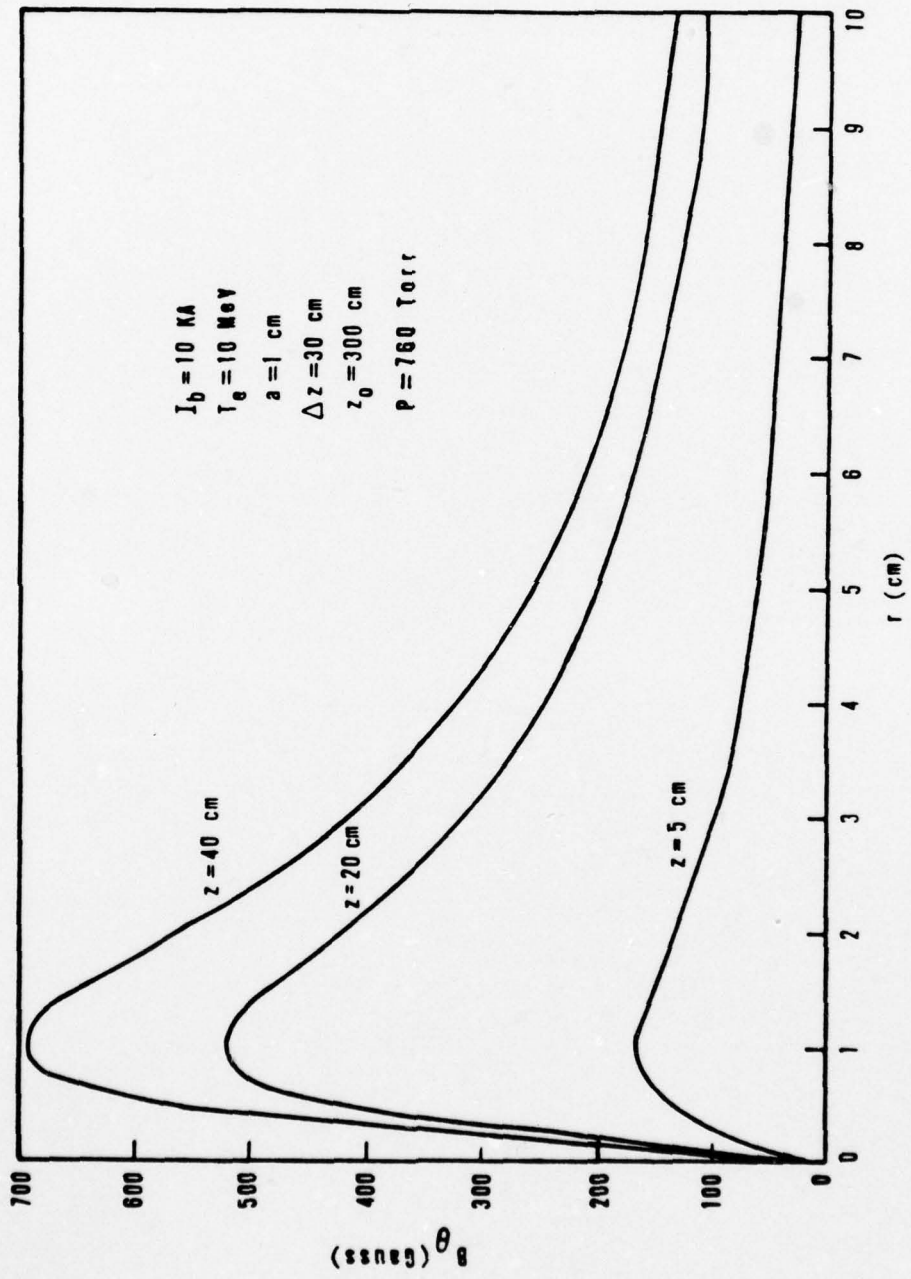


Figure 12. Radial Variation of Azimuthal Magnetic Field

rise portion (at $z=5$ cm and $z=20$ cm) the axial field has a large radial gradient, but the gradient nearly vanishes in the main body of the pulse ($z=40$ cm). Effects of conductivity change on the azimuthal magnetic field are shown in Figure 12. We compare these radial plots with the radial variation of the magnetic field for a pulse in a vacuum, also given by (Appendix A) $\frac{r}{r^2+a^2}$. We notice that there is little change in the shape of the radial profile. However, the magnitude of the field at $r = a$ and $z = 40$ cm has been decreased to 70% of its vacuum value.

Comparison of the One- and Two-Dimensional Models

In general, agreement between the one- and two-dimensional models is close for an air pressure of one atmosphere. In Figure 13 we have plotted the axial variation of the fields from program BEAM2, which solves the one-dimensional model equations. These curves should be compared with the comparable curves from program BEAM1, plotted in Figure 9. As in the BEAM1 calculation we here ignore cascade ionization. Axial profiles of the radial electric field and the magnetic field calculated by BEAM2 are virtually identical with the profiles calculated by BEAM1. We do observe some differences in the axial variation of the axial electric field. The one-dimensional model predicts that the axial field begins slightly earlier, peaks earlier, and begins decay earlier, than the two-dimensional model predicts. These differences are

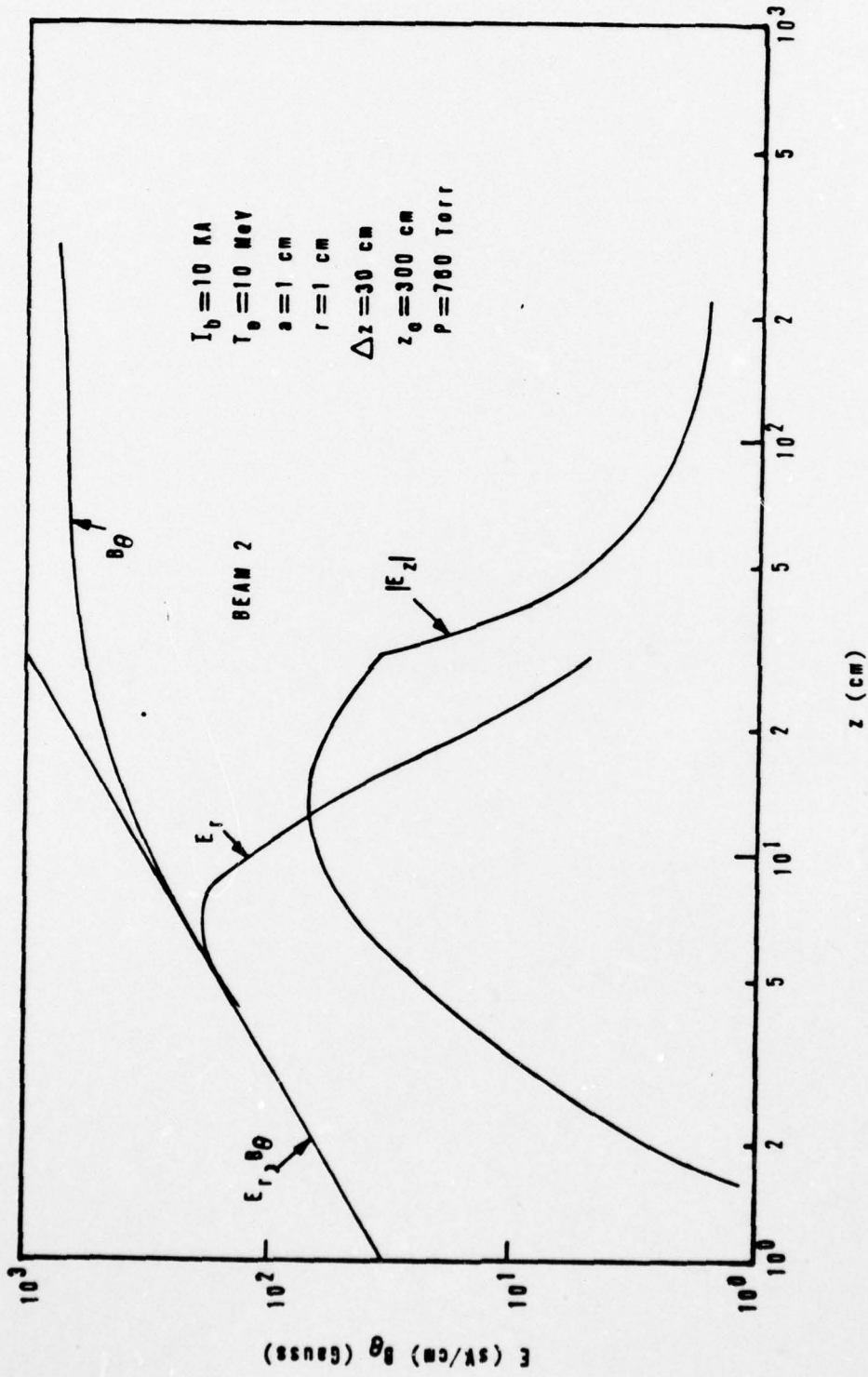


Figure 13. Behavior of Fields, BEAM2

attributed to the approximate integration over the radial electric field performed in deriving the one-dimensional model equations. Since the axial electric field does not enter directly into the evaluation of the plasma current, the small calculated differences are of little consequence.

A comparison of the radial variation of the axial field as computed by BEAM1, and as analytically estimated from the one-dimensional model, is shown in Figure 14. We have normalized the one-dimensional model results to agree with results from BEAM2 at $r=a$. We do this to facilitate comparison of the radial variations. The analytic estimate of the radial variation is found from Ohm's law,

$$E_z(t,r) = \frac{J_{pzo}(t)h(r)}{\Sigma(t)f(r)} = \frac{J_{pzo}(t)}{\Sigma(t)} [1 - \ln(1+r^2/a^2) / \ln(1+b^2/a^2)]$$

Values of the parameter, b , are taken from BEAM1 results. The curves for case $z=20$ cm show good agreement. This is typical in the rise portion of the pulse. In the main body of the pulse ($z=40$ cm), though, the analytic approximation does not predict the pronounced flattening of the radial profile that results from BEAM1 show. The flattening indicates that the radial profile of the plasma current density is nearer to the radial profile of the conductivity than is indicated by $h(r)$ in equation (3-21).

At lower pressures the agreement between the fields as computed by the two programs is not as exact, but is

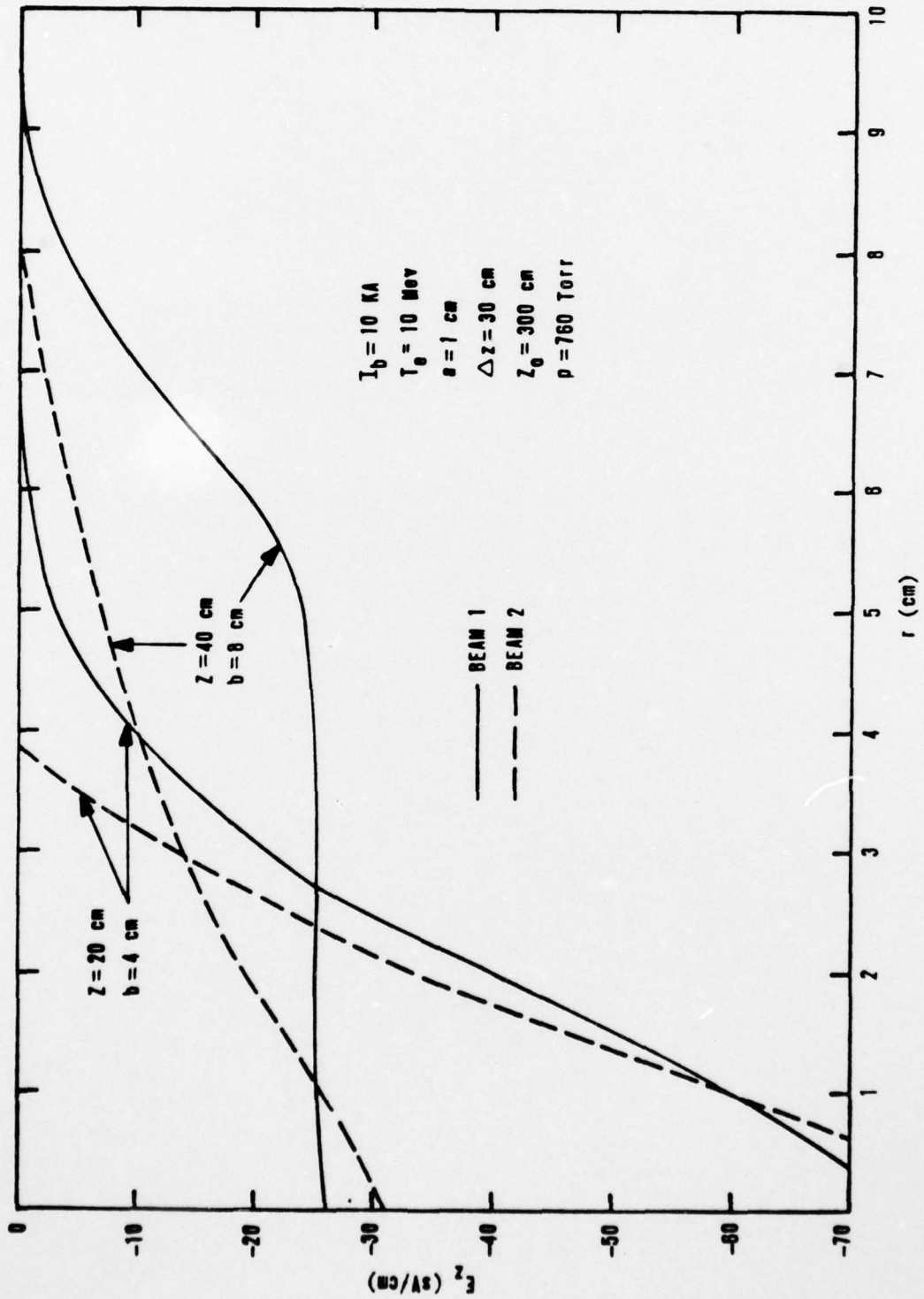


Figure 14. Comparison of Calculated and Analytically Estimated Radial Variation of Axial Electric Field, 760 Torr

still close. Figure 15 compares the axial variation of the fields predicted by the two models at a pressure of 76 Torr. At the top of the pulse rise the one-dimensional model predicts a magnetic field of 300 Gauss while the two-dimensional model predicts a field of 400 Gauss. This corresponds to plasma currents of seven kilo-Amperes and six kilo-Amperes, respectively, so what appears as a 25% difference in the predicted magnetic field is really only a 15% difference in the predicted plasma current. This difference lessens further into the pulse. We again see that results from BEAM2 predict a slightly different behavior for the axial field early in the pulse than does BEAM1. Agreement is very close in the main body of the pulse.

In Figure 16 we compare the predicted radial variation of the axial field for the two different models. Again, the one-dimensional model predicts a slope which is too large, but in this case the two-dimension model predicts less flattening of the field at 40 centimeters into the pulse than is predicted at an air pressure of 760 Torr. This change in the radial profile of the field is caused by a change in the radial profile of the plasma density from a Bennett profile. The two computed profiles for the plasma density are shown in Figure 17. Increased avalanche ionization in the wings of the beam are responsible for the change. This change also results in a small overestimate of the on-axis conductivity in the one-

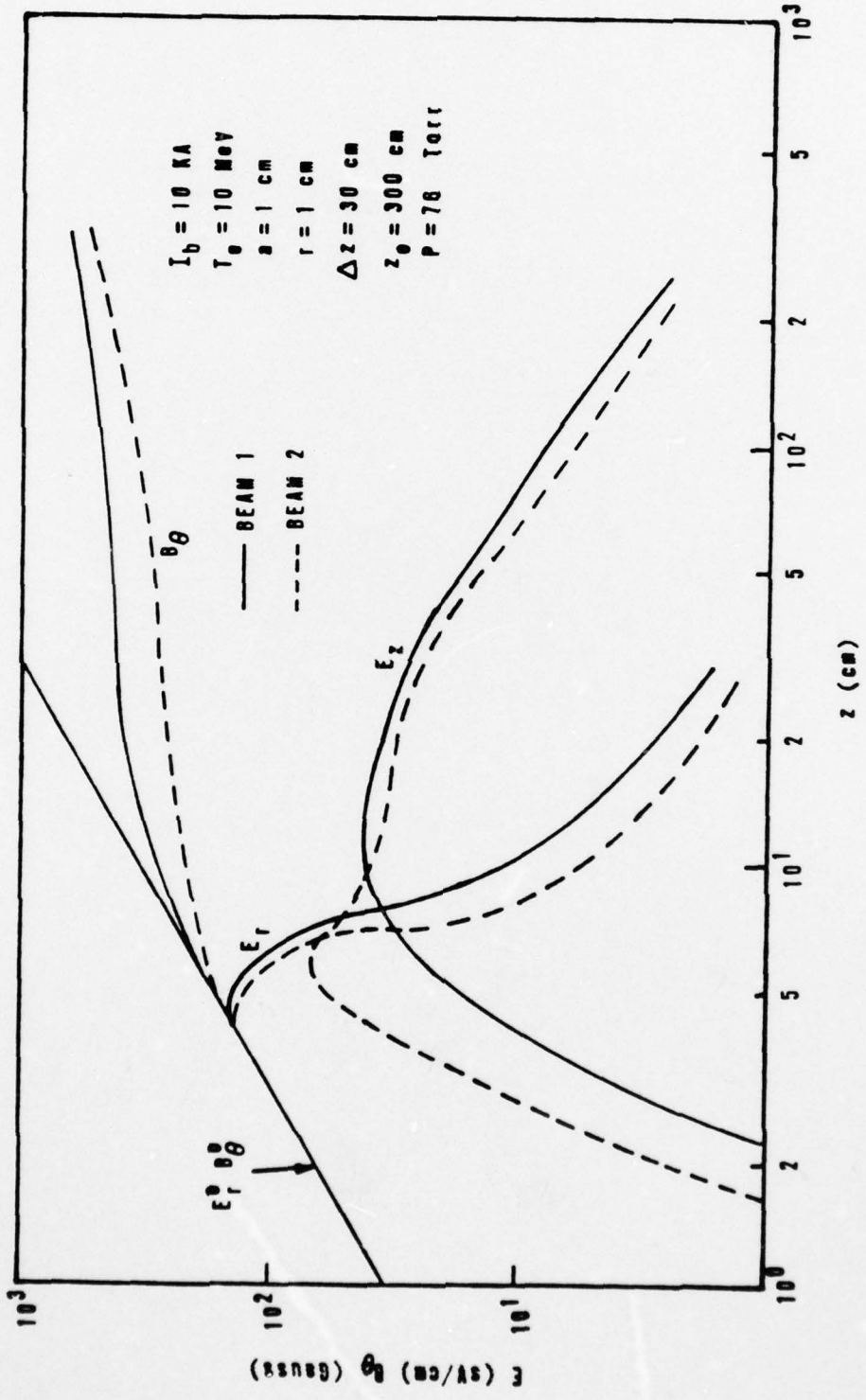


Figure 15. Comparison of Calculated Axial Behavior of Fields

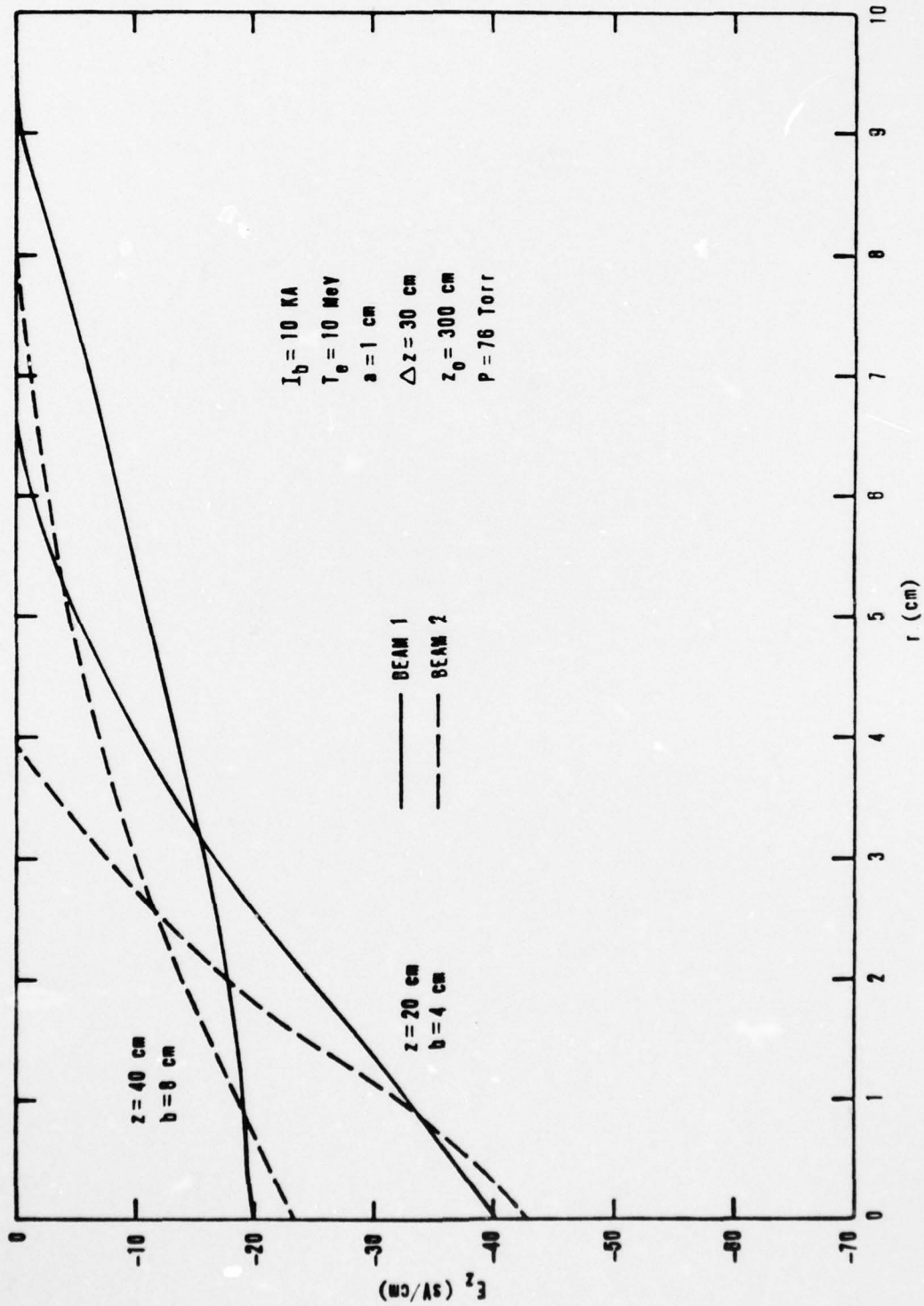


Figure 16. Comparison of Calculated and Analytically Estimated Radial Variation of Axial Electric Field, 76 Torr

AD-A071 621

AIR FORCE INST OF TECH WRIGHT-PATTERSON AFB OHIO SCH--ETC F/6 20/3
ELECTRIC AND MAGNETIC FIELDS OF AN INTENSE PULSE OF RELATIVISTI--ETC(U)
1979 K A DREYER

UNCLASSIFIED

AFIT/DS/PW/79-1

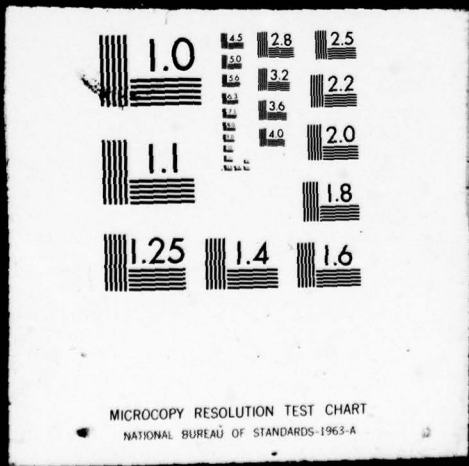
NL

2 of 3
AD
A071621



2 OF 3

AD
A071621



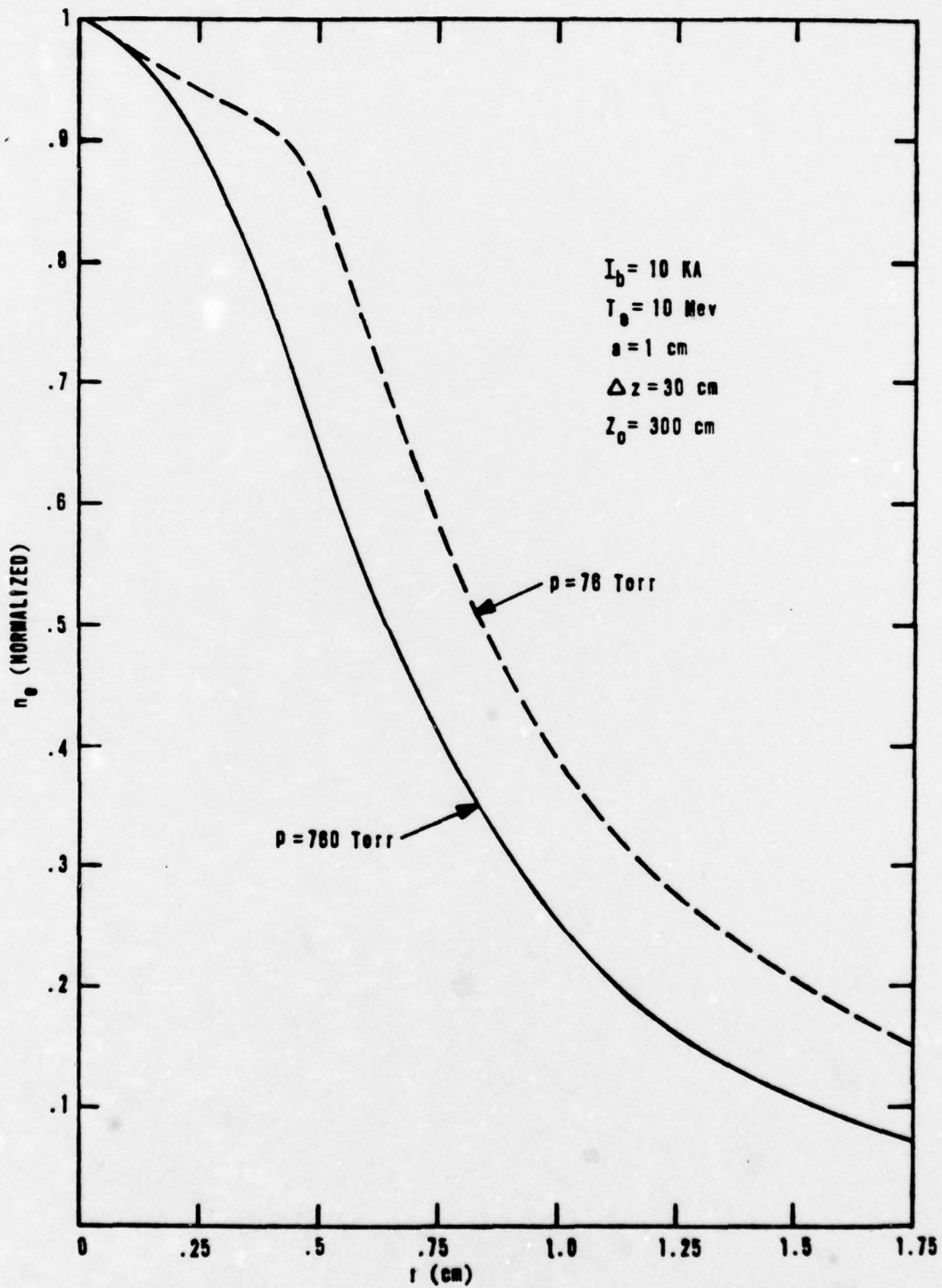


Figure 17. Comparison of Radial Variation of Electron Density at 760 and 76 Torr

dimensional model resulting in the slight overestimate of the plasma current that we observe.

Comparison With Experiment and Previous Calculations

The most detailed description of the conductivity generation yet devised for electron beam propagation in air is the model employed by Johnston in his first beam calculations (Ref 11). He considered 45 molecular species and 325 possible reactions that could affect conductivity. We here present a conductivity calculation of his and compare it to results from program BEAM1 in Figure 18. Both curves show the saturation of conductivity by electron-ion recombination and attachment. Since the calculation is performed for a pressure of one atmosphere virtually all plasma electrons are produced by direct ionization. Thus, avalanche ionization rates are not important here.

We also compare Johnston's predicted electron and neutral gas energies with results from program BEAM1 in Figure 19. The calculated neutral gas energies compare well, but the electron energy curves show considerable disagreement toward the end of the pulse. We attribute this difference to an effective energy transfer rate of Johnston's model that is too low. Johnston does not use a bulk energy transfer rate but a rate is specified for each of the 45 molecular species, so it is not possible to make a direct comparison of the electron cooling rates. It is apparent, though, that the high electron energy predicted

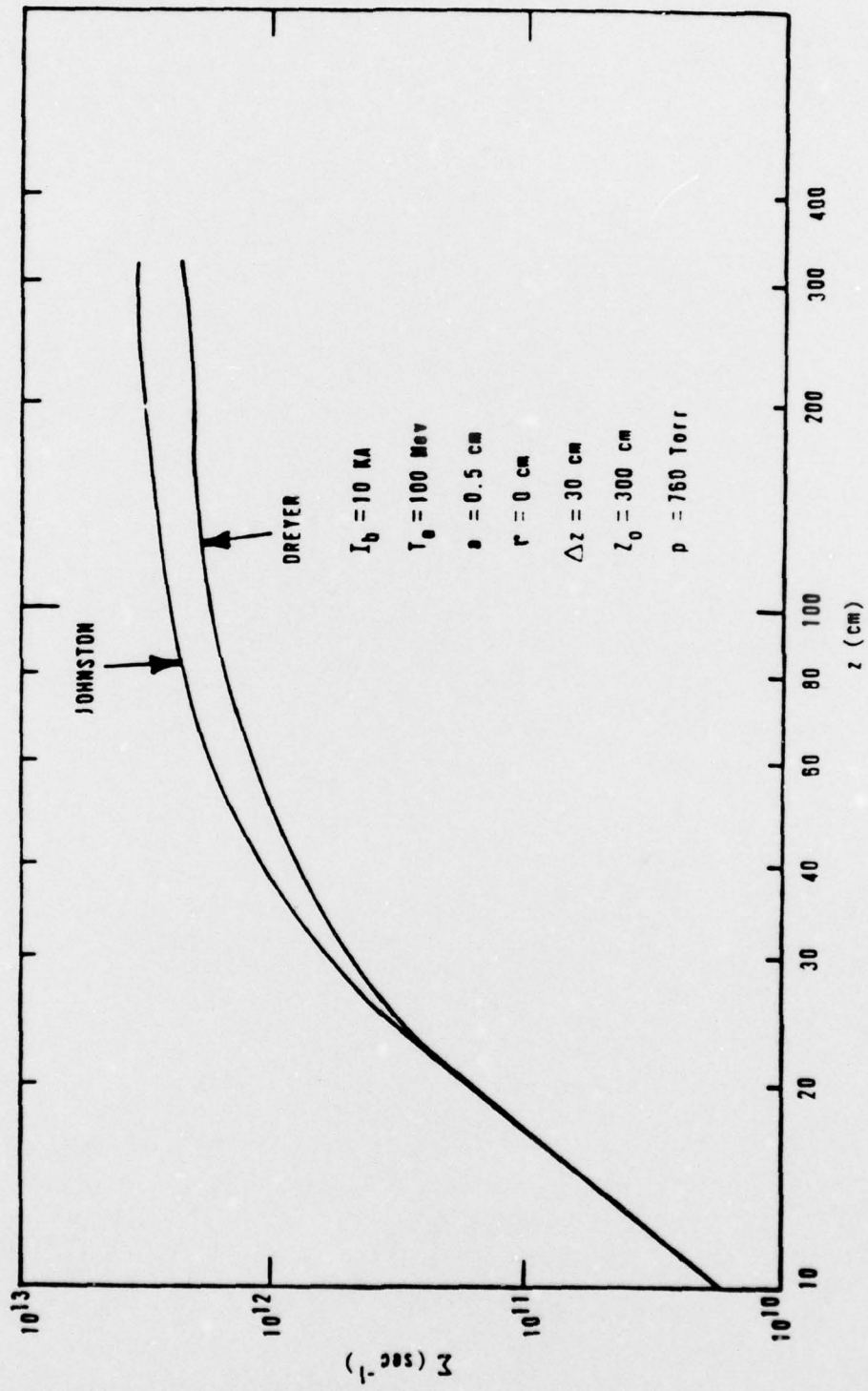


Figure 18. Comparison of Conductivity Calculations from Johnston and Dreyer

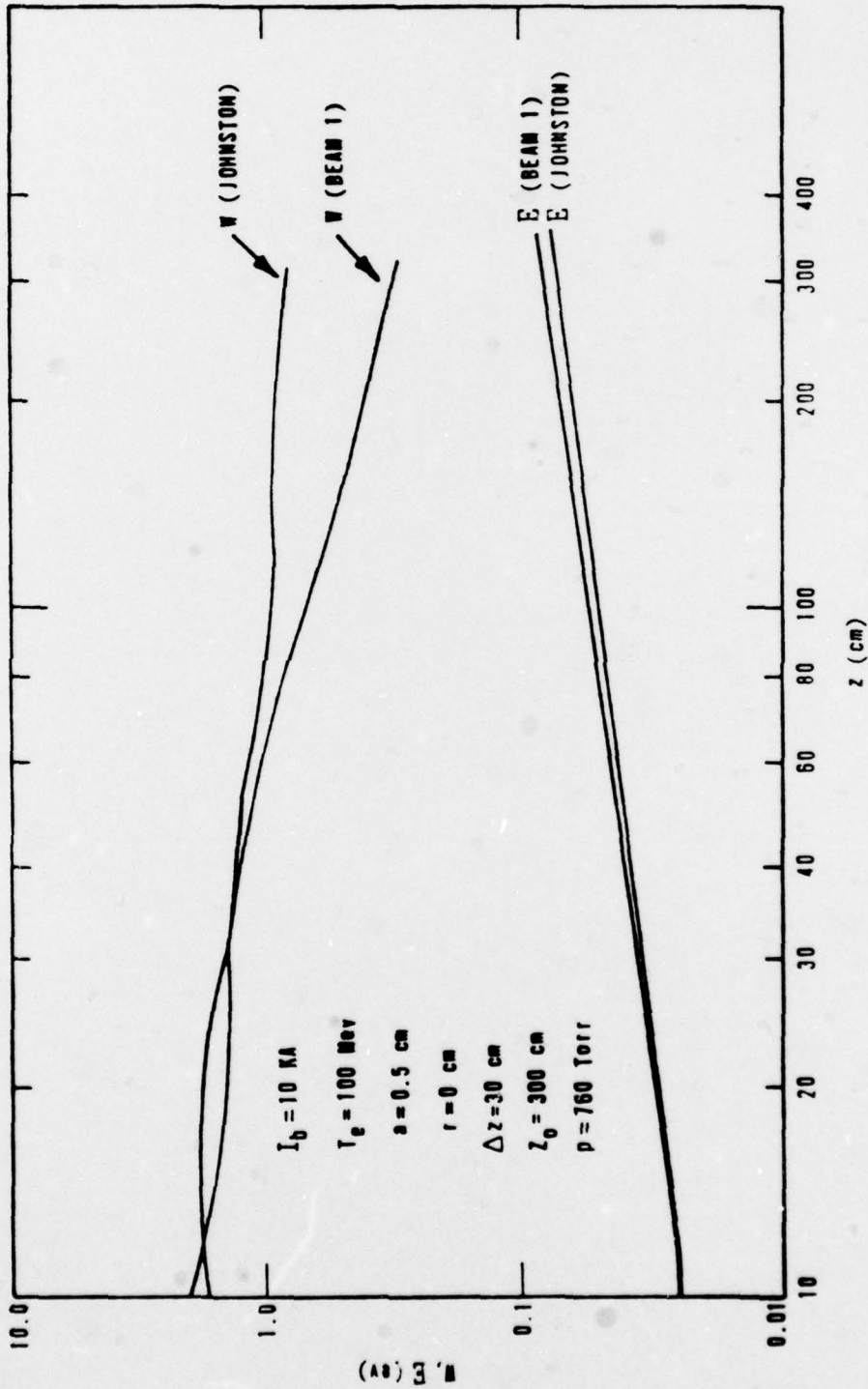


Figure 19. Comparison of Electron and Neutral Gas from Johnston and Dreyer

by the Johnston model could lead to an overestimate of the avalanche rate and conductivity, if applied to air pressures much lower than atmospheric.

Recently, Johnston has produced a simplified version of his original ionization model, named BMCOND (Refs 38, 39 and 40). Johnston has optimized the model for electron beam propagation at a pressure of one atmosphere and chosen reaction rates so that parameters agree with his original model. In addition to Johnston, Lee (Ref 17) has developed a fully coupled electromagnetic and ionization model, called EMPULSE. The EM model employs the vector potential only, rather than the fields. His ionization rate is taken from air breakdown data taken by Felsenthal and Proud (Ref 18). He does not include recombination or attachment in his calculation of the plasma charge state.

We compare the results from these models to net current and plasma electron density measurements by Briggs et al (Ref 4) on an FX-25 electron beam machine, and we compare with results from program BEAM1 and BEAM2. This comparison is shown in Figures 20, 21, and 22. From Figure 20 we see that the experimental data shows a lower net current flow at low pressures than at a pressure of one atmosphere. This decrease in net current is attributed to the increased avalanche ionization rate and the corresponding increase in the conductivity. Lee's model is adequate in the range of five to 20 Torr, but agreement is poor above 50 Torr where electron attachment begins to

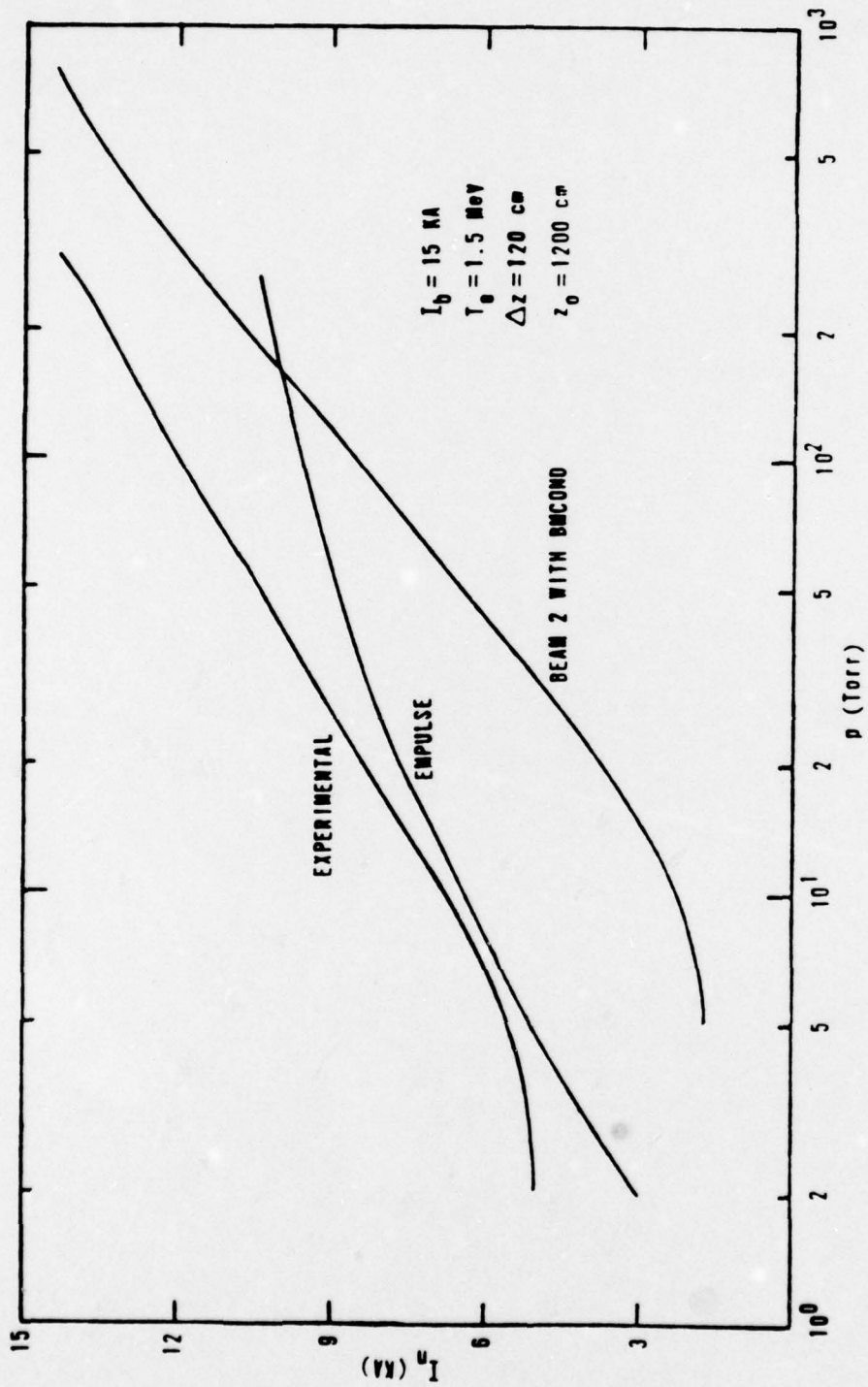


Figure 20. Comparison of Experimental Net Current with Calculated Values from EMPULSE and BMCOND

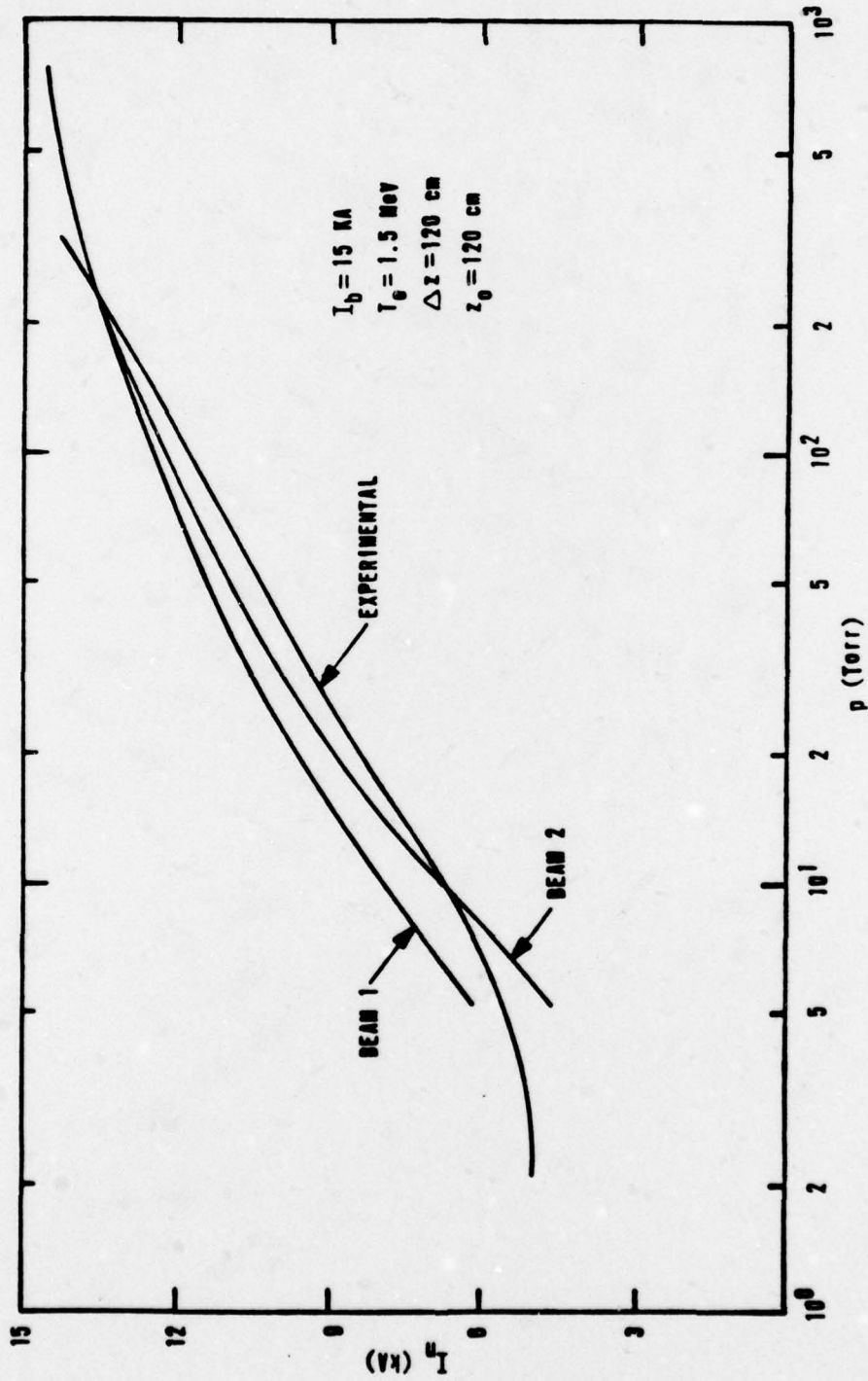


Figure 21. Comparison of Experimental Net Current with Calculated Values from BEAM1 and BEAM2

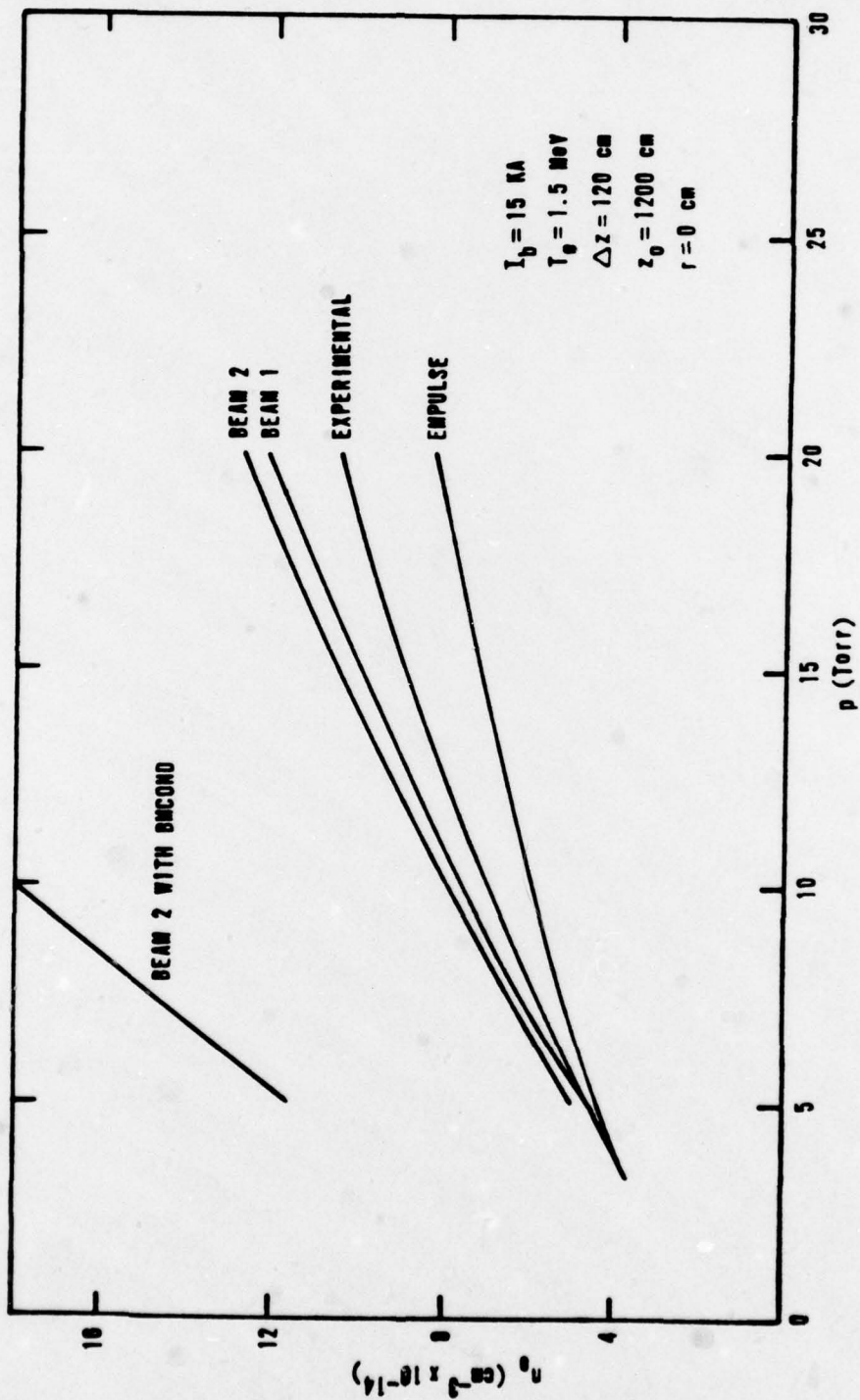


Figure 22. Comparison of Experimental Electron Density with Calculated Values

significantly change the conductivity. We have replaced our ionization model in program BEAM2 with Johnston's model, BMCOND. Results are also shown on Figure 20. At all pressures below one atmosphere the computed net current is much too low. In Figure 21 we compare net current predictions from BEAM1 and BEAM2 (with our ionization model) with the experimental measurements. Agreement between results from BEAM1 and BEAM2 are within 25% everywhere, and agreement between the numerical results and the experimental values is within 20% everywhere. Considering the uncertainties in the experimental measurement and in modeling the pulse shape, the agreement is remarkable.

In Figure 22 we compare predicted on-axis plasma electron density results from all of the calculational models with the experimental data. We see that predicted densities from BEAM1 and BEAM2 lie about the same distance above the experimental curve as do predicted densities from EMPULSE. Predicted values from BMCOND are several times those values observed experimentally. As in Johnston's detailed ionization model, BMCOND predicts values for the electron energy that are much higher than predicted by the model of this study. The higher electron energy results in much higher avalanche rate and a much higher plasma electron density.

We make one final comparison between calculated and experimental results. In Table III we present a comparison of the observed net current from the FX-100

electron beam machine to results from BEAM1 and BEAM2. Only two experimental points are available (Ref 41), but the agreement is again quite close.

TABLE III
COMPARISON OF THEORY AND FX-100 DATA

Beam Current	$I_b = 60 \text{ kA}$
Electron Energy	$T_e = 4 \text{ MeV}$
Rise Length	$\Delta z = 300 \text{ cm}$
Constant Density	$z_o = 1500 \text{ cm}$

Pressure	Measured Net Current	Calculated Net Current BEAM1	Calculated Net Current BEAM2
760 Torr	31 kA	35 kA	34 kA
5 Torr	9 kA	13 kA	6 kA

Again, the cascade ionization time lag has been set equal to zero in these calculations that are compared to experimental data. Since the measurement of the plasma electron density occurred at a time of 10^{-6} seconds after the pulse had passed (Ref 4), the cascade was completed by the time the measurement was taken. Calculated values that were compared to experimental data were taken at the rear of the pulse. Thus we have agreement between the calculated plasma density and the observed density. Effects of the ionization cascade are discussed in the

next part of this section.

Effects of Cascade Ionization Time Lag

All of the computational results from BEAM2 that were compared to experimental data were run again with cascade ionization included. There were virtually no differences in the computed values of magnetic field. At atmospheric pressure computed values of the electron density were virtually identical with computed values assuming a zero lag time. At low pressures (less than 100 Torr) differences in the electron density were observed in the constant density portion of the pulse, but the plasma electron density in the rise portion of the pulse showed virtually no change. Thus, the fields are essentially unaltered when including the cascade ionization time lag.

There are two causes for this insensitivity of the fields to the cascade process. At a pressure near one atmosphere a substantial fraction of the cascade is completed in a very short time. Although the time required to complete the cascade, and produce an additional 1.5 electrons per primary event, is 10^{-9} seconds at 760 Torr, half of the additional electrons (0.75) are produced within 10^{-11} seconds (see Figure 7 of the previous section). Therefore, 70% of all ionization produced per primary ionization is produced within 10^{-11} seconds, at atmospheric pressure. Considering that the radial electric field does not begin its decay until a few tenths of a

nanosecond, the cascade approaches completion long before the radial field begins decay. Consequently, the lag phenomenon has little effect on the fields for a pulse traveling through air at a pressure of one atmosphere.

The second cause is that at low pressures (less than 100 Torr) avalanche ionization dominates over direct ionization in the rise portion of a pulse. For example, in the test case of a 10 kilo-Ampere beam propagating in 76 Torr air the predicted value of the electric field is near 50 kV/cm over most of the pulse rise. This field strength heats up the electrons to an energy near 5 eV. The avalanche coefficient at this electron energy is $7.5 \times 10^9 \text{ sec}^{-1}$ (Appendix B). Thus, an estimate for the e-folding time for electron production is 1.3×10^{-10} seconds.

The dominance of avalanche ionization over direct ionization is illustrated in Figure 23. Here we compare the plasma electron density calculated with lag to the plasma electron density calculated without lag (zero lag time). Values are taken from program BEAM2. When the elapsed time is too short and the fields not strong enough to induce significant avalanche, the electron density predicted by the calculation without lag is 2.5 times larger than that predicted by the calculation with lag. But at 10 centimeters into the pulse, or about 3×10^{-10} seconds, avalanching dominates in both cases, and the predictions merge. After the axial field decays suffi-

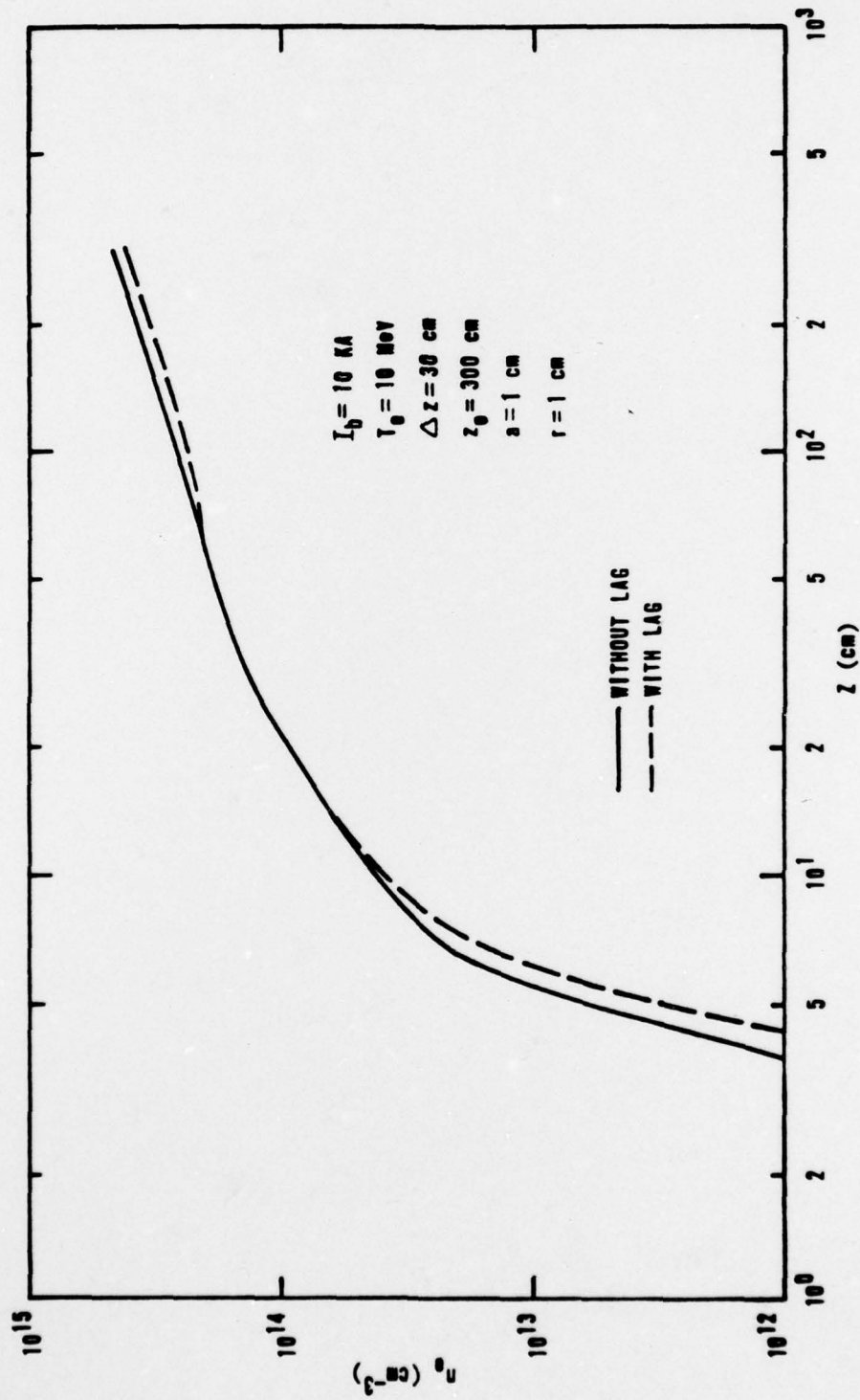


Figure 23. Comparison of Calculated Electron Density With and Without Cascade Ionization Lag

ciently so that the avalanche ionization rate is less than the impact ionization rate, the two sets of calculated values diverge once again. This occurs shortly after the end of the pulse rise portion. For this case it occurs after about 50 centimeters into the pulse. Since the major changes of the fields from their vacuum values occur in the rise portion of the pulse, the fields calculated with and without the cascade ionization time lag are virtually identical.

Saturation of Net Current

As we have seen, calculations of beam fields prior to this study have generally been restricted to beam currents of 10 to 15 kilo-Amperes, or less. At these currents little current saturation is seen at a pressure of one atmosphere. It is only when the air pressure is dropped to 100 Torr, or below, that current saturation is quite evident. In this work we extend the range of beam currents up to 1,000 kilo-Amperes. In doing this we demonstrate the strength of the saturation effect for different beam currents and air pressures, and we determine, for the first time, the magnitude of the net current that flows through a pulse for beam currents larger than 15 kilo-Amperes. Values of net current are inferred from computed values of the magnetic field computed by program BEAM2.

The calculations are summarized in Figures 24 and 25. We have chosen to maintain a constant current density of

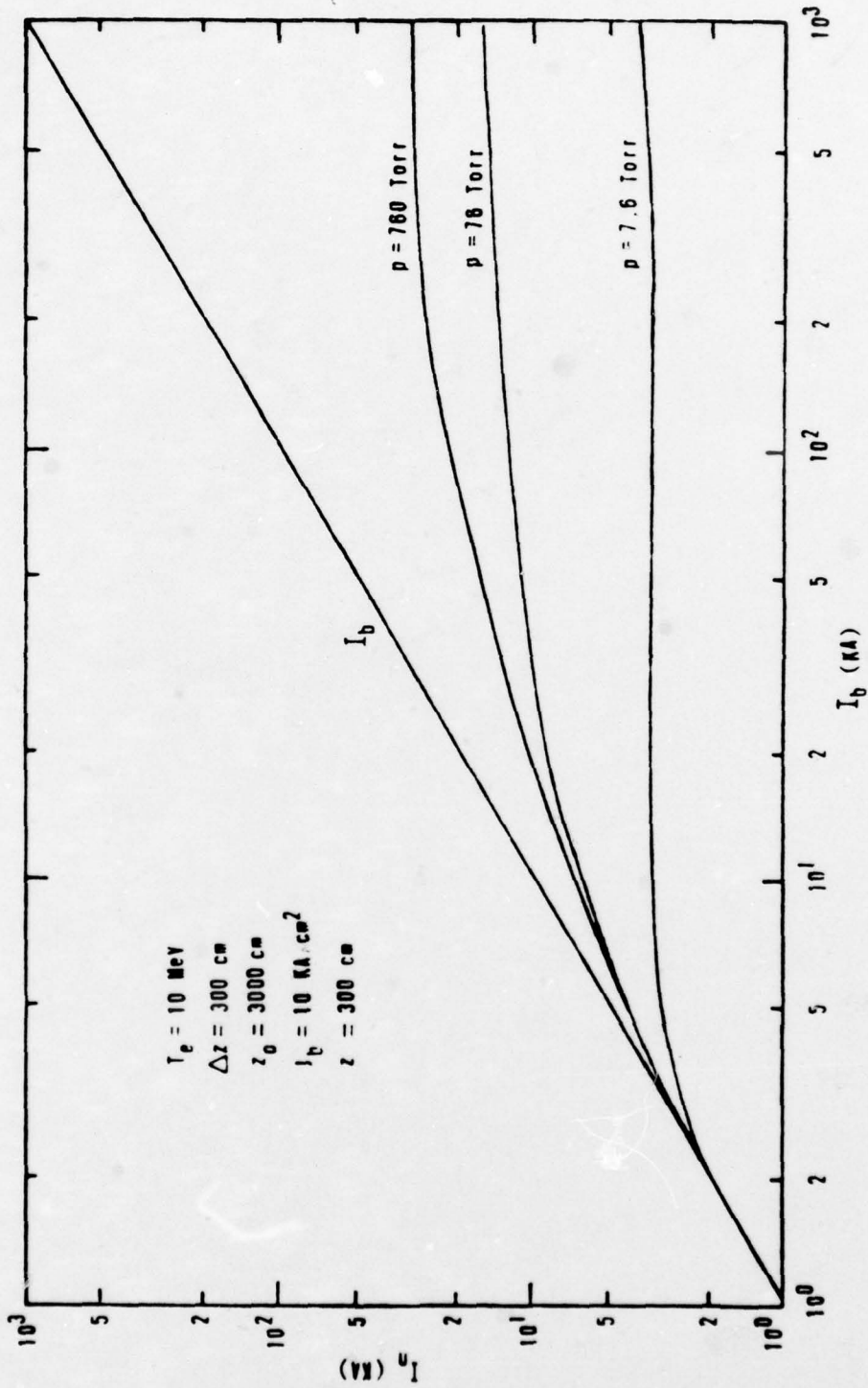


Figure 24. Net Current at the Top of the Current Rise

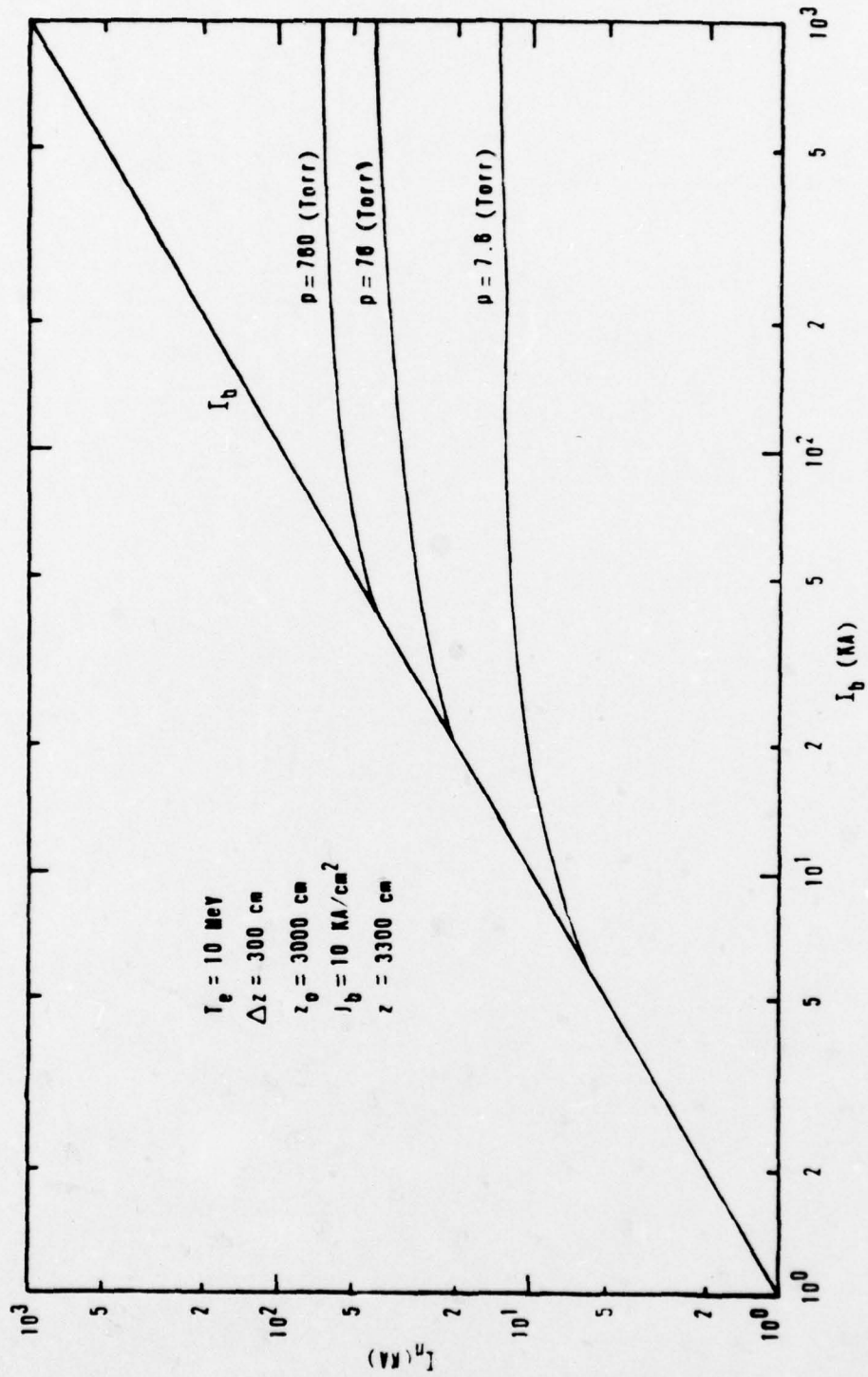


Figure 25. Net Current at the Rear of the Pulse

10 kA/cm² in this calculation so the radius varies from 0.31 centimeters for the one kilo-Ampere pulse to a maximum of 10 centimeters for the 1,000 kilo-Ampere pulse. In Figure 24, we have plotted the net current at the top of the rise portion of the pulse. The maximum current shown in the Figure is 25 kilo-Amperes, produced by a beam with a current of 1,000 kilo-Amperes, propagating through atmospheric pressure air. Thus, the plasma current is 975 kilo-Amperes, or 97.5% of the beam current. The net current is not constant within the pulse, but continues a slow increase. In Figure 25 we have plotted the net current at the rear of the pulse. We see that the maximum current observed is 70 kilo-Amperes for a 1,000 kilo-Ampere beam current. This is an increase over the 25 kilo-Amperes computed at the top of the rise portion. We note, too, that the net current decreases substantially with air pressure. For the 1,000 kilo-Ampere beam the net current at the top of the rise portion at a pressure of 7.6 Torr is three kilo-Amperes, while at a pressure of 760 Torr the net current is 25 kilo-Amperes.

Discussion

From the results presented in this section we have established four major points.

1. The general agreement between predictions of the models and experimental measurements demonstrates the validity of the models.

2. Considering the good agreement between the one-dimensional and the two-dimensional models we conclude that the one-dimensional model provides an adequate description of the fields, over the range of parameters considered in this study.

3. Since avalanche ionization dominates at low pressures, the cascade ionization time lag is of no consequence in determining the behavior of the fields.

4. For the first time we calculate current saturation at atmospheric pressure, and predict net current flow in a pulse for beam currents up to 1,000 kilo-Amperes.

VI. MAJOR CONCLUSIONS AND RECOMMENDATIONS

Major Conclusions

Considering the theory developed in earlier sections, and results presented in the last section, we draw four major conclusions from this study.

1. The theoretical models developed in the course of this work accurately portray the electrodynamics of a propagating electron beam. In particular, our ionization model is the only one that is valid over a wide range of air pressures and beam parameters. Agreement between available experimental data and the predictions of the model are generally within 15% and no worse than 30%.

2. Considering the good agreement between the one-dimensional and the two-dimensional EM models, and the excellent agreement between the predictions of the one-dimensional model and experimental data, we conclude that the one-dimensional model provides an adequate description of conductivity generation, net current flow, and the axial variation of the EM fields over the pressure range of five to 760 Torr. The analytically predicted radial variation of the axial electric field closely resembles the numerically predicted radial variation in the pulse rise portion, but does not predict the pronounced

flattening that the numerical model predicts in the constant portion of the pulse. We observe a factor of 50 reduction in computing time when solving the one-dimensional model equations over the two-dimensional model equations.

3. At low pressures (less than 100 Torr) avalanche ionization dominates over direct ionization, so the cascade ionization time lag has virtually no effect upon the behavior of the fields. In essence, the avalanche compensates for any changes introduced into direct ionization, so it is not necessary to include a non-zero cascade ionization lag time in field calculations. One would expect a similar result for other gases with ionization cross sections similar to nitrogen.

4. As beam current is increased, and all other parameters are held constant, the magnetic diffusion time also increases. This causes the net current flowing in the beam to saturate. At atmospheric pressure this saturation is most evident above beam currents of 15 kilo-Amperes. At lower air pressures current saturation occurs at lower beam currents. Above a beam current of 15 kilo-Amperes large increases in beam current produce only small increases in the net current.

Recommendations

The ionization and EM models derived here were developed to study atmospheric propagation of an intense

pulse of relativistic electrons. However, the EM models are applicable to any kind of charged particle beams, including proton beams or heavy ion beams. Much of the ionization model could also be used for propagation studies of other kinds of charged particles. The plasma electron-air molecule reactions (avalanche, attachment, recombination), and the collision frequencies are obviously independent of the type of charge particle beam. Only the direct ionization rates need to be changed. It would be very useful to apply the models of this study, with the appropriate changes in direct ionization, to other types of charged particle beams currently of interest.

No matter what type of beam the researcher is interested in the primary consideration in propagation studies must be the response of beam particles to their self-fields. While this study does not allow the beam particles to move with the fields, results from this study provide an estimate of the response. However, to accurately assess the beam evolution, both the fields and the beam particle motions must be calculated simultaneously to allow their interaction. Preliminary investigations in this area are underway.

REFERENCES

1. Thode, L. E., "Energy Lost by a Relativistic Electron Beam Due to Two-Stream Instability." Phys. of Fluids 19:2, 305-315 (1976).
2. Faltens, A. and D. Keefe, "Acceleration System for Heavy-Ion Beams for Inertial Confinement Fusion." Proceedings of 2nd International Topical Conference on High-Power Electron and Ion Beam Research and Technology, Cornell University, Ithaca, New York, October 5-7, 1977.
3. Briggs, R. and R. Hester, Preliminary Experimental Results on the Streaming Instability, UCID 5079, Lawrence Livermore Laboratories, Livermore, California, November 9, 1965.
4. Fessenden, T. J., R. J. Briggs, J. C. Clark, E. J. Lauren and D. O. Trimble, FX-25 Beam Propagation Experiments, UCID 17840, Lawrence Livermore Laboratories, Livermore, California, June 20, 1978.
5. Miller, B. R., Hermes-II Pressure Window Measurements, unpublished manuscript, Sandia Corporation, Albuquerque, New Mexico, 1978.
6. Dreyer, K. A., FX-100 Pressure Window Measurements, Air Force Weapons Laboratory Technical Report (to be published), Kirtland Air Force Base, New Mexico, 1979.
7. Lee, E. P., Hose Instability at Arbitrary Conductivity, UCID-16734, Lawrence Livermore Laboratories, Livermore, California, March 7, 1975.
8. Lee, E.P., Hose Theory, UCID-16268, Lawrence Livermore Laboratories, Livermore, CA., May 16, 1973.
9. Lee, E. P., F.W. Chambers, L. L. Lodestro and S.S. Yu. "Stable Propagation of an Electron Beam in Gas." Proceedings of 2nd International Topical Conference on High-Power Electron and Ion Beam Research and Technology, Cornell University, Ithaca, New York, October 5-7 1977.
10. Thode, L. E. "Plasma Heating by Scattered Relativistic Electron Beams: Correlations Among Experiment, Simulation, and Theory," Phys. of Fluids 19:6, 831-848 (1976).

11. Johnston, R.R., Task II - Studies in Non-Equilibrium Air Plasma - EO and RF Observables, SAI-072-647-PA, Science Applications, Inc: Palo Alto, CA, 20 December 1975.
12. Porter, H.S., C.H. Jackman and A.E.S. Green, "Efficiencies for Production of Atomic Nitrogen and Oxygen by Relativistic Proton Impact in Air." J. of Chem. Phys. 65:1, 154-167 (1976).
13. Longmire, C.L. and H.J. Longley, Improvements in the Treatment of Compton Current and Air Conductivity in EMP Problems. DNA 3192T, Mission Research Corporation: Santa Barbara, CA., September 25, 1973.
14. Paulouskii, G.V., G.V. Karpou, G.G. Katraev, N.I. Leonova, and E.N. Snuinore, "Cylindrical Channel in a High-Current Discharge in Air." Soviet Phys. Tech. Phys. 20:182-186 (1975).
15. Leonow, S.N. and R.A. Liukoneru, "Temperature and Densities in a High-Current Discharge in Air." Sov. Phys. Tech. Phys. 21:1287-1288 (1976).
16. Longmire, C.L., Private communication, 1976.
17. Lee, E. P., The New Field Equations, UCID-17286, Lawrence Livermore Laboratory: Livermore, CA, October 4, 1976.
18. Felsenthal, P. and J.M. Proud, "Nanosecond-Pulse Breakdown in Gases." Phys, Rev. 134:A1796-A1804 (1965)
19. Wittwer, L. High Altitude Conductivity Models for Electromagnetic Pulse Calculations, AFWL-TR-74-191, Air Force Weapons Laboratory: Kirtland AFB, NM.
20. Alfven, H. "On the Motion of Cosmic Rays in Interstellar Space." Phys Rev. 55:2, 425-432 (1939).
21. Dogliani, H.O. and K.A. Dreyer, Alfven Limit for a Bennett Profile, AFWL-DYP-TN-104, Air Force Weapons Laboratory, Physics Division, Advanced Concepts Branch: Kirtland AFB, NM, 1977.
22. Miller, B.R. and K.A. Dreyer, "Net Current and Emission by Open Shutter Photography," submitted to Nuclear Technology Digest for publication, Air Force Weapons Laboratory, Kirtland AFB, NM, 1979.
23. Potter, D., Computational Physics. John Wiley and Sons: New York, 1973.

24. Carnahan, B., H.A. Luther and J.O. Wilkes, Applied Numerical Methods. John Wiley and Sons: New York, 1969.
25. Karzas, W. J. and R. Latter, "Detection of the Electromagnetic Radiation from Nuclear Explosions in Space." Phys. Rev. 137:5B, 1369-1378 (1965).
26. Dennemeyer, R., Introduction to Partial Differential Equations and Boundary Value Problems. Mc-Graw-Hill: New York, 1968.
27. Lee, E.P. Kinetic Theory of a Relativistic Beam, UCRL-76420, Lawrence Livermore Laboratory: Livermore, CA, July 25, 1975.
28. Radasky, W.A., An Examination of The Adequacy of the Three-Species Air Chemistry Treatment for the Prediction of Surface Burst EMP. DNA 3880T, Mission Research Corporation: Santa Barbara, CA (1975).
29. Zel'dovich, Ya. B. and Yu. P. Raizer, Physics of Shock Waves and High-Temperature Hydrodynamic Phenomena, Vol. I. Academic Press: New York, 1966.
30. Jackson, J. D., Classical Electrodynamics, John Wiley and Sons, Inc.: New York, 1962.
31. Ali, A. W., J. R. Greig, I. M. Vitkovitsky, R. M. Fiorito, and R. M. Fernsler, "Interaction of an Intense Relativistic Electron Beam with the Atmosphere", Contributed paper submitted to XIV International Conference on Phenomena in Ionized Gases: Grenoble, France, July 9-13, 1979.
32. Spitzer, L., Physics of Fully Ionized Gases. 2nd ed., Interscience Publishers. New York, 1962.
33. Lunn, P.W., Electron Energy Deposition in Gases, M.S. Thesis, Colorado State University: Fort Collins, CO, April 1973.
34. Opal, C.B., E.C. Beatty and W.K. Peterson, "Tables of Secondary-Electron-Production Cross Sections." Atomic Data 4: 209-253 (1972).
35. Evans, R.D., The Atomic Nucleus. McGraw-Hill: New York, 1955.
36. Price, W.J., Nuclear Radiation Detection. McGraw-Hill: New York, 1964.

37. Canavan, G.H., J.E. Brau and L..A. Wittwer, Sensitivity of Self-Consistent High-Altitude Electromagnetic Pulse Calculations to Preionization and Improved Source and Ionization Models, AFWL-TR-74-48, Air Force Weapons Laboratory, Kirtland AFB, NM 1973.
38. Johnston, R.R., Private Communication, 1978.
39. Lemke, R. Comparison of the Beam Induced Air Conductivity Model (BMCOND) with the Fluid Model (FM), AFWL-DYP-TN-78-117, Air Force Weapons Laboratory, Kirtland AFB, NM, 1978.
40. Lemke, R. Numerical Comparison of the Beam-Induced Air Conductivity Model with the Fluid Model, AFWL-DYP-TN-78-122, Air Force Weapons Laboratory, Kirtland AFB, NM, 1978.
41. Ames, G., R. Little, K. Childen, and M. Kime, TREF Electron Beam Development Program, FR-74-10008, Simulation Physics, Inc., Burlington, MA, 1974.
42. Gradshteyn, J.S., and T.M. Ryzik, Table of Integrals Services, and Products, 4th ed, Academic Press: New York, 1965.
43. Bortner, M.H. and T. Baurer, ed., Reaction Rate Handbook. DNA 1948H, General Electric: Santa Barbara, CA, March 1972.
44. Frost, L.S. and A.V. Phelps, "Rotational Excitation and Momentum Transfer Cross Sections for Electron in H₂ and N₂ from Transport Coefficients". Phys. Rev. 127: 5,1621-1633 (1962).
45. Englehardt, A.S. and A. V. Phelps, "Elastic and Inelastic Collision Cross Sections in Hydrogen and Deuterium from Transport Coefficients." Phys. Rev. 131:5, 2115-2128 (1963).
46. Englehardt, A.G. A.V. Phelps and C.G. Risk, "Determination of Momentum Transfer and Inelastic Collision Cross Sections for Electrons in Nitrogen Using Transport Coefficients." Phys. Rev. 135:6A, A1566-1574, (1964).
47. Hoake, R.O. Jr. and A.V. Pehlps, "Momentum Transfer and Inelastic Collision Cross Sections for Electrons in O₂, CO, and C.", Phys. Rev. 158:1, 70-84 (1967).
48. Phelps, A.V., "Rotational and Vibrational Excitation of Molecules by Low-Energy Electrons", Rev. of Mod. Phys. 40:2, 399-410 (1968).

49. Fite, W.L. and R.J. Brachmann, Proceedings of the Fourth International Conference on the Physics of Electronic and Atomic Collisions, Science Book-crafters, Inc., New York, 1965, p. 100.
50. O'Malley, T.F., "Calculation of Dissociative Attachment in Hot O₂", Phy. Rev. 155:1, 159-63 (1966).
51. Pearson, C.E., ed. Handbook of Applied Mathematics. p. 325, Van Nostrand Reinhold Company: New York, 1974.
52. Henrici, P. Elements of Numerical Analysis. p. 72, John Wiley and Sons, Inc: New York, 1964.
53. Rees, M.H., and R.A. Jones, "Time Dependent Studies of the Auroa-II. Spectroscopic Morphology." Plan. Space Sci. 21: 1213-1235 (1973).
54. Shyn, T.W., R.S. Stolarski and G.R. Carignan, "Angular Distribution of Electrons Elastically Scattered from N₂." Phys. Rev. A 6:3, 1002-1012 (1972).
55. Toburen, L.H., "Distributions in Energy and Angle of Electrons Ejected from Molecular Nitrogen by 0.3 to 1.7 Mev Protons." Phys. Rev. A 3:1, 216-228 (1971).
56. Opal, C.B., E.C. Beaty and W.K. Peterson, "Tables of Secondary-Electron-Production Cross Sections." Atomic Data 4: 209-253 (1972).
57. Green, A.E.S. and T. Sawada, "Ionization Cross Sections and Secondary Electron Distributions." J. of Atmos. and Terr. Phys. 34: 1719-1728 (1972).
58. Edgar, B.C., W.T. Miles and A.E.S. Green, "Energy Deposition of Protons in Molecular Nitrogen and Applications to Proton Aural Phenomena", J. of Geophy. Res. 78: 28, 6595-6606 (1973).

APPENDIX A
EM FIELDS OF A BEAM IN A VACUUM

In sections II and III the EM models that are employed in this study were developed. In both the one- and two-dimensional models the EM fields of a beam propagating through a vacuum arise in a natural way. In this Appendix we calculate the fields of a beam in a vacuum.

To simplify calculations we assume that all beam particles move in the longitudinal direction at the same speed, and that the fields as seen in the beam frame are time independent. These two assumptions allow the vacuum fields to be determined from a scalar potential, ϕ .

The method employed here is to find the fields of a pulse of relativistic charged particles as seen in the pulse frame of reference, then perform a Lorentz transformation of the fields back to the laboratory frame of reference. Letting the star denote the value of the parameters in the pulse system, and the unstarred parameters be measured in the laboratory system, the transformation equations are (Ref 30)

$$X_{\alpha}^{*} = a_{\alpha\beta} X_{\beta}$$

$$\begin{aligned}
J_{\alpha}^{*} &= a_{\alpha\beta} J_{\beta} \\
x_{\alpha} &= (x, y, z, ict) \\
J_{\alpha} &= (J_x, J_y, J_z, ic\rho) \\
a_{\alpha\beta} &= \begin{pmatrix} 1 & 0 & 0 & 0 \\ 0 & 1 & 0 & 0 \\ 0 & 0 & \gamma & i\beta\gamma \\ 0 & 0 & -i\beta\gamma & \gamma \end{pmatrix}
\end{aligned}$$

Thus, we have,

$$r^{*} = (x^{*2} + y^{*2})^{1/2} = r \quad (\text{A-1})$$

$$z^{*} = \gamma z + i\beta\gamma(ict) = \gamma(z - \beta ct) \quad (\text{A-2})$$

$$ic\rho^{*} = i\gamma(c\rho - \beta J_z)$$

$$\rho^{*} = \gamma\left(\rho - \frac{\beta}{c} J_z\right) = \gamma\left(\rho - \frac{\beta}{c} \rho\beta c\right)$$

$$\rho^{*} = \gamma\rho(1 - \beta^2) = \rho/\gamma \quad (\text{A-3})$$

The inverse transformation of the fields is found from the four-tensor,

$$F_{\alpha\beta} = \begin{pmatrix} 0 & B_z & -B_y & -iE_x \\ -B_z & 0 & B_x & -iE_y \\ -B_y & B_x & 0 & -iE_z \\ iE_x & iE_y & iE_z & 0 \end{pmatrix}$$

which transforms according to (Ref 30)

$$F_{\alpha\beta} = b_{\alpha\gamma} b_{\beta\delta} F_{\gamma\delta}^*$$

where

$$b_{\alpha\gamma} = \begin{pmatrix} 1 & 0 & 0 & 0 \\ 0 & 1 & 0 & 0 \\ 0 & 0 & \gamma & -i\beta\gamma \\ 0 & 0 & i\beta\gamma & \gamma \end{pmatrix}$$

Performing the indicated tensor multiplication results in

$$E_x = \gamma (E_x^* + \beta B_y^*)$$

$$E_y = \gamma (E_x^* - \beta B_x^*)$$

$$E_z = E_z^*$$

$$B_x = \gamma (B_x^* - \beta E_y^*)$$

$$B_y = \gamma (B_y^* + \beta E_x^*)$$

$$B_z = B_z^*$$

Realizing that the magnetic field is zero in the starred system the transformation equations reduce to

$$E_r = (E_x^2 + E_y^2)^{1/2} = \gamma E_r^* \quad (\text{A-4})$$

$$E_z = E_z^* \quad (\text{A-5})$$

$$B_\theta = (B_x^2 + B_y^2)^{1/2} = \beta \gamma E_r^* = \beta E_r \quad (\text{A-6})$$

Here we have used

ρ = pulse charge density

β = v/c

γ = $(1-\beta^2)^{-1/2}$

In the main body of the pulse the fields are assumed to take on the values of a beam with infinite longitudinal extent. That is,

$$E_z = 0 \quad (\text{A-7})$$

$$E_r = \frac{4\pi}{r} \int_0^r r' \rho(r') dr' \quad (\text{A-8})$$

$$B_\theta = \beta E_r = \frac{4\pi\beta}{r} \int_0^r r' \rho(r') dr' \quad (\text{A-9})$$

It is in the rise portion of the pulse that our main interest lies, so the remainder of this Appendix deals with a close look at the fields in this region.

Two different approaches are employed here to find the fields. The first is to make various approximations in order to find analytic forms that nearly reproduce the actual field values. The second approach is to perform a more exact numerical calculation. Comparison between the two approaches shows close agreement.

Analytic Approximation

In order to find approximate forms for the fields our method is to make an ordering argument to show that the axial electric field is usually much weaker than the radial electric field. This allows the equations to be decoupled, and the fields found. The ordering of the fields is, of course, valid in the laboratory frame of reference as well. However, we make the ordering argument in the beam frame, and demonstrate its validity there, because the argument is much simpler in the beam frame.

Employing a Cartesian coordinate system for simplicity, the wave equation for the fields in the beam frame is

$$\vec{\nabla} \times (\vec{\nabla} \times \vec{E}^*) = \nabla^2 \vec{E}^* - 4\pi \vec{\nabla} \rho^* = 0 \quad (\text{A-10})$$

The formal solution is

$$\vec{E}^* = -4\pi \int_{-\infty}^{\infty} \frac{\vec{\nabla}' \rho^*(\vec{r}^{*'}) d\vec{r}^{*'}}{|\vec{r}^* - \vec{r}^{*'}|} \quad (\text{A-11})$$

If the charge density, ρ^* , is a reasonably smooth function of r^* (or x^* and y^*) and most of the charge is contained inside a radial distance a , then

$$\frac{\partial \rho^*}{\partial x^*} \sim \frac{\partial \rho^*}{\partial y^*} \sim \frac{\rho^*}{a^*} \quad (\text{A-12})$$

where " \sim " means "on the order of". Likewise, if ρ^* varies smoothly in the longitudinal direction, then

$$\frac{\partial \rho^*}{\partial z^*} \sim \frac{\rho^*}{\Delta z^*} \quad (\text{A-13})$$

where Δz^* is the length of the rise portion in the pulse frame. For this study we restrict ourselves to

$$\Delta z^* \gg a^* \quad (\text{A-14})$$

Then

$$\frac{\rho^*}{a^*} \gg \frac{\rho^*}{\Delta z^*} \quad (\text{A-15})$$

and

$$\frac{\partial \rho^*}{\partial x^*} \sim \frac{\partial \rho^*}{\partial y^*} \gg \frac{\partial \rho^*}{\partial z^*} \quad (\text{A-16})$$

Therefore,

$$E_x^* \sim E_y^* \gg E_z^* \quad (\text{A-17})$$

or

$$E_r^* \gg E_z^* \quad (\text{A-18})$$

The ordering argument (A-18) allows the fields to be derived. The divergence equation is

$$\frac{1}{r^*} \frac{\partial}{\partial r^*} (r^* E_r^*) + \frac{\partial E_z^*}{\partial z^*} = 4\pi\rho^* \quad (\text{A-19})$$

Making another ordering argument,

$$\frac{1}{r^*} \frac{\partial}{\partial r^*} (r^* E_r^*) \sim \frac{E_r^*}{a^*} \quad (\text{A-20})$$

$$\frac{\partial E_z^*}{\partial z^*} \sim \frac{E_z^*}{\Delta z^*} \quad (\text{A-21})$$

we have

$$\frac{1}{r^*} \frac{\partial}{\partial r^*} (r^* E_r^*) \gg \frac{\partial E_z^*}{\partial z^*} \quad (\text{A-22})$$

Thus

$$\frac{1}{r^*} \frac{\partial}{\partial r^*} (r^* E_r^*) = 4\pi\rho^* \quad (\text{A-23})$$

and

$$E_r^* = \frac{4\pi}{r^*} \int_0^{r^*} r'^* \rho^*(r'^*, z^*) dr'^* \quad (\text{A-24})$$

Transforming now to the laboratory frame,

$$E_r = \frac{4\pi}{r} \int_0^r r' \rho(r', t-z/\beta c) dr' \quad (\text{A-25})$$

$$B_\theta = \beta E_r = \frac{4\pi\beta}{r} \int_0^r r' \rho(r', t-z/\beta c) dr' \quad (\text{A-26})$$

Notice that the forms for E_r and B_θ in the rise portion of the pulse are the same as that in the main body of the pulse. This is a direct consequence of the smallness of E_z in the rise portion which results from

$$\frac{a^*}{\Delta z^*} = \frac{a}{\gamma \Delta z} \ll 1 \quad (\text{A-27})$$

Therefore, as long as (A-27) holds the above approximate solutions for E_r and B_θ are valid.

With both the radial electric field and the azimuthal magnetic field specified, the longitudinal electric field can be determined within an integration constant. From Faraday's Law,

$$\vec{\nabla} \times \vec{E} = - \frac{1}{c} \frac{\partial \vec{B}}{\partial t} \quad (\text{A-28})$$

we have, in cylindrical coordinates,

$$\frac{1}{c} \frac{\partial B_\theta}{\partial t} = \frac{\partial E_z}{\partial r} - \frac{\partial E_r}{\partial z} \quad (\text{A-29})$$

Since

$$z - \beta ct = \text{Constant} \quad (\text{A-30})$$

then,

$$\frac{\partial E_r}{\partial z} = - \frac{1}{\beta c} \frac{\partial E_r}{\partial t} \quad (\text{A-31})$$

and

$$\frac{\partial E_z}{\partial r} = \frac{1}{c} \frac{\partial B_\theta}{\partial t} - \frac{1}{\beta c} \frac{\partial E_r}{\partial t} \quad (\text{A-32})$$

$$\frac{\partial E_z}{\partial r} = \frac{1}{c} \frac{\partial}{\partial t} (\beta E_r - \frac{1}{\beta} E_r) \quad (\text{A-33})$$

$$\frac{\partial E_z}{\partial r} = - \frac{1}{\beta c} \frac{\partial E_r}{\partial t} (1 - \beta^2) = - \frac{1}{\beta c \gamma^2} \frac{\partial E_r}{\partial t} \quad (\text{A-34})$$

Finally,

$$E_z(r, z, t) = E_z(0, z, t) - \frac{1}{\beta c \gamma^2} \frac{\partial}{\partial t} \int_0^r E_r dr \quad (\text{A-35})$$

An order of magnitude estimate for E_z , and a rough scaling law, can also be derived. Recalling the formal solution to the pulse fields in (A-11), by invoking a volume oriented mean value theorem one can write

$$E_r^* = I \left| \frac{1}{r^*} \frac{\partial}{\partial r^*} (r^* \rho^*) \right|_{\vec{r}^* = \vec{r}_1^*} \quad (\text{A-37})$$

and

$$E_z^* = I \left| \frac{\partial \rho^*}{\partial z^*} \right|_{\vec{r}^* = \vec{r}_2^*} \quad (\text{A-37})$$

where

$$I = -4\pi \int_{-\infty}^{\infty} \frac{d\vec{r}^{*'}}{|\vec{r}^* - \vec{r}^{*'}|}$$

and \vec{r}_1^* and \vec{r}_2^* are the points where the equality expressed in (A-36) and (A-37) hold, respectively. Estimating the mean value derivatives by

$$\left| \frac{1}{r^*} \frac{\partial}{\partial r^*} (r^* \rho^*) \right|_{\vec{r}^* = \vec{r}_1^*} \sim \frac{\rho^*}{a} \quad (\text{A-38})$$

and

$$\left| \frac{\partial \rho^*}{\partial z^*} \right|_{\vec{r}^* = \vec{r}_2^*} \sim \frac{\rho^*}{\Delta z} \quad (\text{A-39})$$

we have

$$\frac{E_r^*}{E_z^*} \sim \frac{\rho^*/a^*}{\rho^*/\Delta z^*} = \frac{\Delta z^*}{a^*} \quad (\text{A-40})$$

Thus

$$E_z = E_z^* \sim \frac{a^*}{\Delta z^*} \sim \frac{a}{\gamma^2 \Delta z} E_r \quad (\text{A-41})$$

If

$$E_r = 10^3 \text{ sV/cm}$$

$$a = 1 \text{ cm}$$

$$\Delta z = 100 \text{ cm}$$

$$\gamma = 10$$

then

$$E_z \sim 0.1 \text{ sV/cm}$$

Notice that (A-41) predicts inverse scaling with Δz and inverse square scaling with γ . In the next section this scaling will be shown to be approximately, although not rigorously, valid.

In summary, for the radial and longitudinal profiles of this study, the pulse fields in the rise portion of the pulse are estimated to be

$$E_r = 2\pi\rho_0 \frac{t-z/\beta c}{\Delta t} \frac{r}{1+r^2/a^2} \quad (\text{A-42})$$

$$B_\theta = \beta E_r \quad (\text{A-43})$$

$$E_z = E_z(r=0) - \frac{\pi a^2 \rho_0}{2\gamma^2 \Delta z} \ln(1+r^2/a^2) \quad (\text{A-44})$$

Numerical Calculation

A numerical method that accurately calculates the fields in the pulse rise portion is developed here. By

employing a three-dimensional exponential Fourier transform pair, five of the six integrations can be exactly evaluated analytically leaving only one numerical integration.

The exponential Fourier transform pair is defined by

$$\phi^*(\vec{K}) = F\{\phi(\vec{r}^*)\} = \int_{-\infty}^{\infty} \int_{-\infty}^{\infty} \int_{-\infty}^{\infty} \phi^*(\vec{r}^*) \exp \{-i[x^*K_x + y^*K_y + z^*K_z]\} dx^* dy^* dz^* \quad (A-45)$$

$$\phi^*(\vec{r}^*) = F^{-1}\{\phi^*(\vec{K})\} = \left(\frac{1}{2\pi}\right)^3 \int_{-\infty}^{\infty} \int_{-\infty}^{\infty} \int_{-\infty}^{\infty} \phi^*(\vec{K}) \exp \{+i[x^*K_x + y^*K_y + z^*K_z]\} dK_x dK_y dK_z \quad (A-46)$$

where ϕ^* is the scalar potential and again the starred variables are measured in the pulse frame of reference.

By defining

$$\begin{aligned} x^* &= r^* \cos\theta^* \\ y^* &= r^* \sin\theta^* \\ K_x &= K_r \cos\theta_K^* \\ K_y &= K_r \sin\theta_K^* \end{aligned}$$

we have

$$x^*K_x + y^*K_y + z^*K_z = r^*K_r \cos(\theta^* - \theta_K) + z^*K_z \quad (\text{A-47})$$

in cylindrical coordinates. The Fourier transform pair then becomes

$$\phi^*(\vec{K}) = \int_{-\infty}^{\infty} \int_0^{2\pi} \int_0^{\infty} \phi^*(\vec{r}^*) \cdot$$

$$\exp \{-i[r^*K_r \cos(\theta^* - \theta_K) + z^*K_z]\} r^* dr^* d\theta^* dz^* \quad (\text{A-48})$$

$$\phi^*(\vec{r}^*) = \left(\frac{1}{2\pi}\right)^3 \int_{-\infty}^{\infty} \int_0^{2\pi} \int_0^{\infty} \phi^*(\vec{K}) \cdot$$

$$\exp \{i[r^*K_r \cos(\theta^* - \theta_K) + z^*K_z]\} K_r dK_r d\theta_K dK_z \quad (\text{A-49})$$

In the pulse frame, Poisson's equation for the potential is

$$\nabla^2 \phi^* = -4\pi\rho_0^* f(r^*)g(z^*) \quad (\text{A-50})$$

Operating on (A-50) with the transform yields

$$F \{\nabla^2 \phi^*(\vec{r}^*)\} = -(K_r^2 + K_z^2) \phi^*(\vec{K})$$

$$= 4\pi\rho_0^* \int_{-\infty}^{\infty} \int_0^{2\pi} \int_0^{\infty} f(r^*)g(z^*)$$

$$\exp \{-i[r^*K_r \cos(\theta^* - \theta_K) + z^*K_z]\} r^* dr^* d\theta^* dz^* \quad (\text{A-51})$$

Solving for ϕ^* and operating with the inverse transform gives

$$\phi(\vec{r}^*) = \frac{\rho_o^*}{2\pi^2} \int_{-\infty}^{\infty} \int_0^{2\pi} \int_0^{\infty} \exp [i(r^*K_r \cos(\theta^* - \theta_k) + z^*K_z)] \cdot$$

$$\left\{ \int_{-\infty}^{\infty} \int_0^{2\pi} \int_0^{\infty} f(r^*)g(z^*) \exp[-i(r^*K_r \cos(\theta^* - \theta_k) + z^*K_z)] \right\} \cdot$$

$$(r^*dr^*d\theta^*dz^*) \frac{K_r dK_r d\theta_k dK_z}{K_r^2 + K_z^2} \quad (A-52)$$

Some of the integrations in (A-52) can be performed if the order of integration is changed. This is possible since $f(r)$ and $g(z)$ are piece-wise continuous. The following integrals can be evaluated (Ref 42)

$$\int_0^{2\pi} \exp\{-i[r^*K_r \cos(\theta^* - \theta_k)]\} d\theta^* =$$

$$2\pi J_0(r^*K_r) \quad (A-53)$$

$$\int_0^{2\pi} \exp\{i[r^*K_r \cos(\theta^* - \theta_k)]\} d\theta_k =$$

$$2\pi J_0(r^*K_r) \quad (A-54)$$

$$\int_{-\infty}^{\infty} \frac{\exp\{iK_z[z^*-z^{*'}]\}}{K_r^2 + K_z^2} dK_z =$$

$$\frac{\pi}{K_r} \exp\{-k_r |z^*-z^{*'}|\} \quad (\text{A-55})$$

where $J_0(r^*K_r)$ is the zeroth order Bessel function with real argument, and $|z^*-z^{*'}|$ means "magnitude of $z^*-z^{*'}$ ". The potential function now is

$$\phi(\vec{r}^*) = 2\pi\rho_0 \int_0^{\infty} \int_{-\infty}^{\infty} \int_0^{\infty} f(r^{*'})g(z^{*'}) \cdot$$

$$\exp\{-K_r |z^*-z^{*'}|\} J_0(r^{*'}K_r) J_0(r^*K_r) r^{*'} dr^{*'} dz^{*'} dK_r \quad (\text{A-56})$$

To proceed further requires explicit expressions for $f(r)$ and $g(z)$. Using the Bennett profile for $f(r)$,

$$\int_0^{\infty} f(r^{*'}) J_0(r^{*'}K_r) r^{*'} dr^{*'} = a^4 \int_0^{\infty} \frac{r^{*'} J_0(r^{*'}K_r) dr^{*'}}{(r^{*'}{}^2 + a^2)^2}$$

$$= \frac{a^3 K_r}{2} K_1(a^*K_r) \quad (\text{A-57})$$

where K_1 is the modified Bessel function of the second kind, of order one. Thus,

$$\phi(\vec{r}^*) = \pi \rho_0 a^{*3} \int_{-\infty}^{\infty} \int_{-\infty}^{\infty} g(z^{*'}) \exp(-K_r |z^* - z^{*'}|) \cdot$$

$$J_0(r^* K_r) J_1(a^* K_r) K_r dk_r dz^{*'} \quad (A-58)$$

At this point let us define

$$h(z^*, K_r) = \int_{-\infty}^{\infty} g(z^{*'}) \exp(-K_r |z^* - z^{*'}|) dz^{*'} \quad (A-59)$$

When considering the longitudinal density profile for this study (A-59) becomes complicated, but is directly integrable. Recognizing that

$$E_r^* = - \frac{\partial \phi^*}{\partial r^*} \quad (A-60)$$

and

$$E_z^* = - \frac{\partial \phi^*}{\partial z^*} \quad (A-61)$$

we arrive at

$$E_r^*(r^*, z^*) = \pi \rho_0^* a^{*3} \int_0^{\infty} h(z^*, K_r) J_1(r^* K_r) K_1(a^* K_r) K_r^2 dK_r \quad (A-62)$$

and

$$E_z^*(r^*, z^*) = -\pi \rho_0 a^3 \int_0^{\infty} \frac{\partial h(z^*, K_r)}{\partial z^*} J_0(r^* K_r) K_1(a^* K_r) K_r dK_r \quad (A-63)$$

Finally, employing the Lorentz transformation relations back to the pulse frame, we have

$$E_r(r, z) = \pi \rho_0 a^3 \int_0^{\infty} h(z, K_r) J_1(r K_r) K_1(a K_r) K_r^2 dK_r \quad (A-64)$$

$$E_z(r, z) = \frac{\pi \rho_0 a^3}{\gamma^2} \int_0^{\infty} \frac{\partial h(z, K_r)}{\partial z} J_0(r K_r) K_1(a K_r) K_r dK_r \quad (A-65)$$

These forms for the fields are found by numerically integrating over K_r . Comparisons between the analytic and numerically calculated fields are illustrated in Figures 26 and 27.

In equation (A-65) the dependence of E_z upon Δz occurs from both the $1/\Delta z$ slope of $g(z)$ in the rise portion of the pulse and the integrating of $g(z) e^{-K_r |z-z'|}$ over the longitudinal extent of the pulse. Although the scaling of E_z is only approximate, computer integrations of (A-65) verify the approximate scaling of Δz . Consequently, E_z scales approximately inversely with Δz and inversely with the square of gamma.

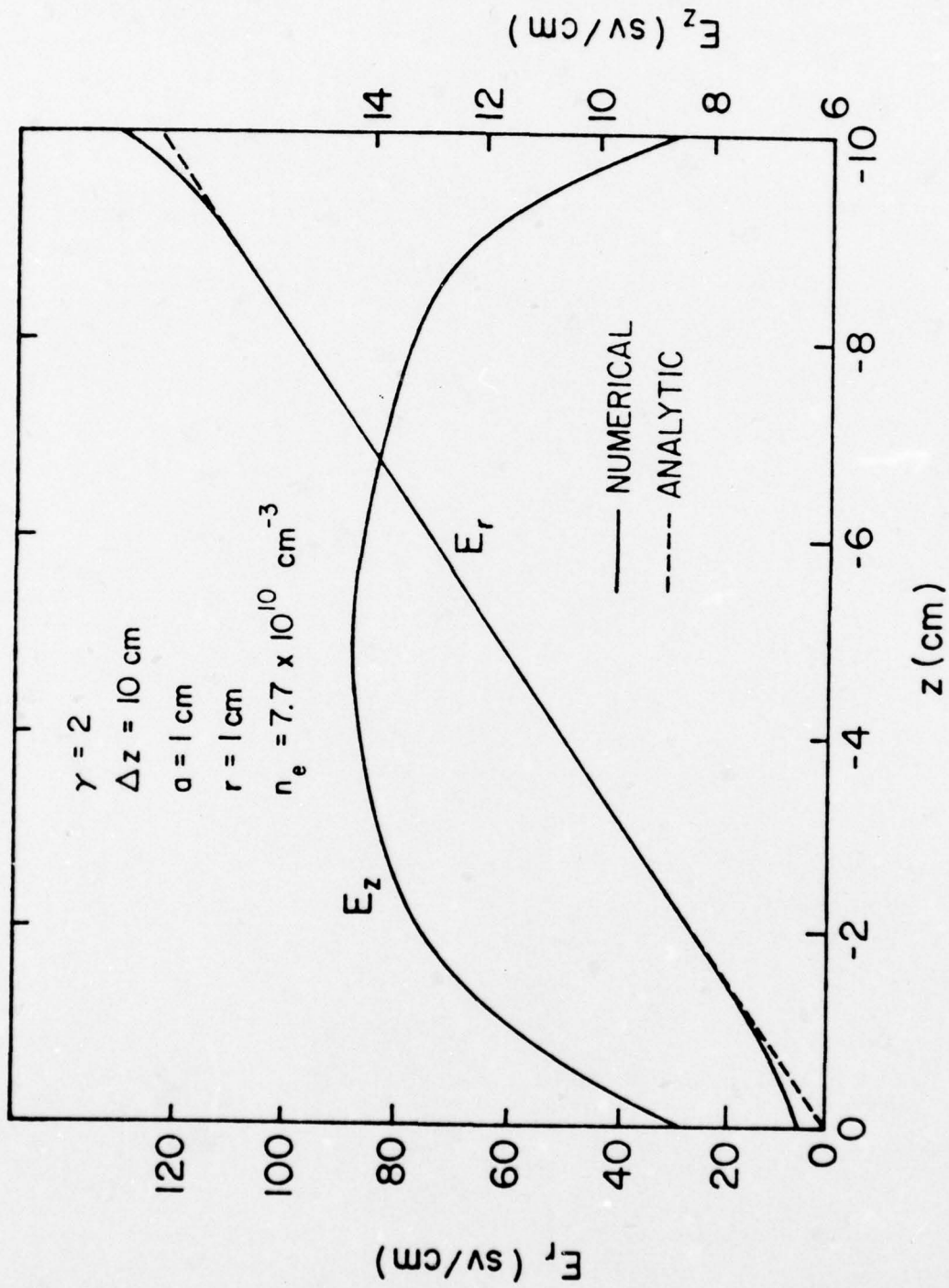


Figure 26. Longitudinal Variation of Vacuum Fields

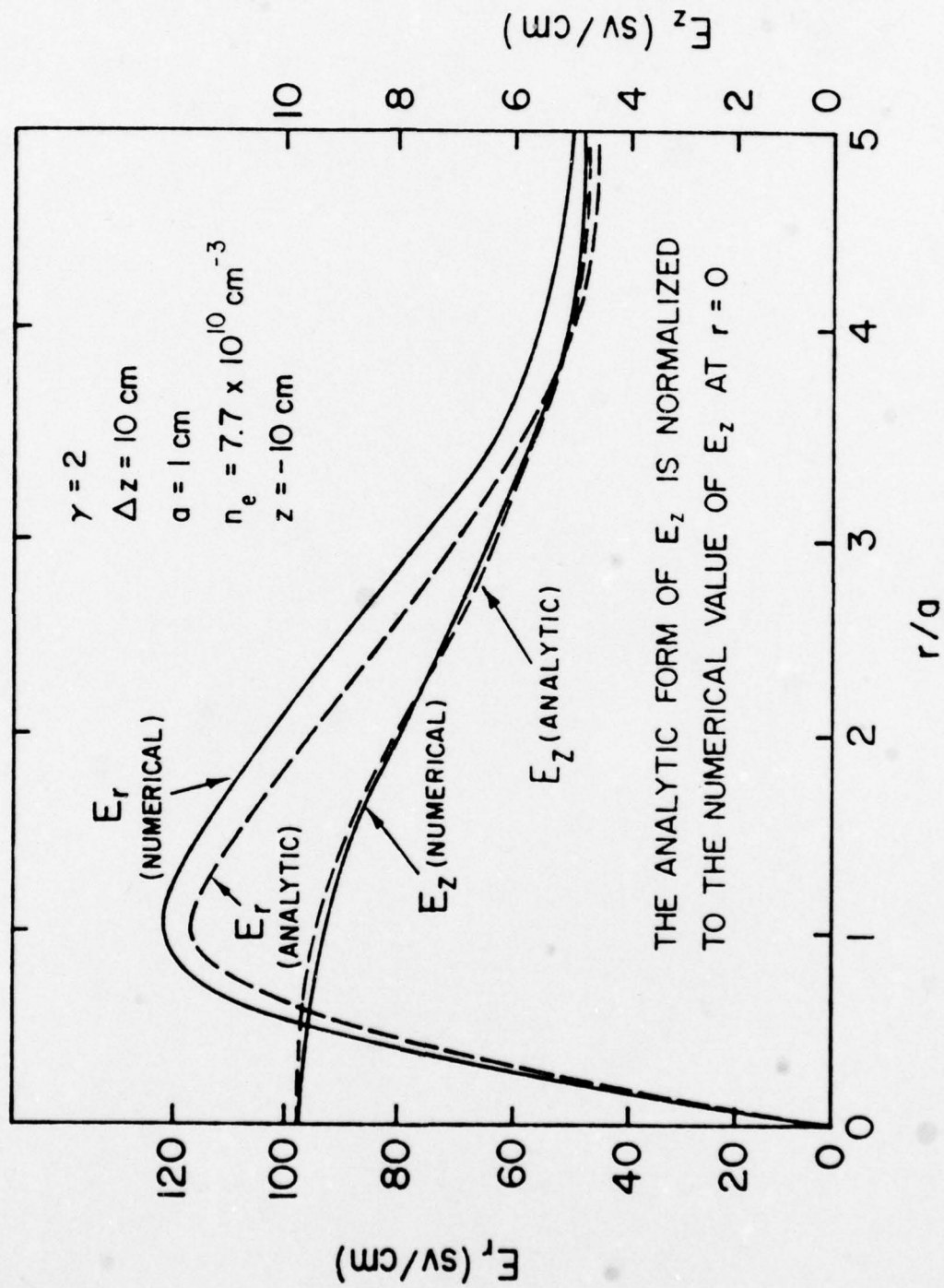


Figure 27. Radial Variation of Vacuum Fields

APPENDIX B
REACTION RATES

As a pulse of electrons enters the atmosphere it interacts strongly with air molecules to produce free electrons. These electrons can then be accelerated by existing electric fields to energies which may be sufficient for the electrons to produce additional free electrons by electron-atom impact ionization. We present here a discussion of the ionization, recombination, and attachment processes used in this work.

Rate Equations

The equations of the ionization model are, from Section IV,

$$\frac{\partial n_e}{\partial t} = \alpha(W)n_e + R_I + \int_{\tau_0}^{\tau} \frac{AR_I(\tau-t)}{\tau} d\tau \quad (B-1)$$

$$\frac{\partial v_r}{\partial t} = \frac{eE_r}{m_e} - (v_m(W) + \alpha_T) v_r \quad (B-2)$$

$$\frac{\partial v_z}{\partial t} = \frac{eE_z}{m_e} - (v_m(W) + \alpha_T) v_z \quad (B-3)$$

$$\frac{\partial W}{\partial t} = e(E_r v_r + E_z v_z) - (v_\epsilon (W) + \alpha_T)W + v_\epsilon \epsilon + S \quad (B-4)$$

$$\frac{\partial \epsilon}{\partial t} = f \left(\frac{dT}{dt} \right) + v_\epsilon \frac{n_e}{N} (W - \epsilon) \quad (B-5)$$

where

n_e = plasma electron density

α = net avalanche (recombination) coefficient

$\alpha_T = \alpha + (1/n_e)R$

R_I = impact ionization rate

v_r = radial plasma electron velocity

v_z = longitudinal plasma electron velocity

E_r = radial electric field

E_z = longitudinal electric field

e = electronic charge

m_e = electron rest mass

v_m = momentum transfer collision frequency

v_ϵ = energy transfer collision frequency

W = characteristic plasma electron energy

S = external heating rate of plasma electrons

ϵ = background neutral gas characteristic energy

$\frac{dT}{dt}$ = energy loss rate of beam particles per unit length per neutral particle

f = fraction of beam energy loss that goes directly to neutral particles

N = neutral particle density

The empirical parameters are given by:

Electron-neutral momentum transfer collision frequency

$$\frac{\nu_{mn}}{N} = 1.25 \times 10^{-7} W^{0.935} (1 + 0.093 W^{1.5})^{0.405} /$$
$$(1 + 1.26 W^{1.67})^{0.373} \quad (B-6)$$

Electron-ion momentum transfer collision frequency

$$\nu_{mi} = 1.46 \times 10^{-6} (n_e / W^{3/2}) \ln[1.55 \times 10^{10} (W^3 / n_e)^{1/2}] \quad (B-7)$$

Electron-neutral energy transfer collision frequency

$$\frac{\nu_E}{N} = 1.3 \times 10^{-11} (1 + 4.4 \times 10^4 W^5)^{0.32} /$$
$$(1 + 1.93 \times 10^3 W^{10})^{0.138} + 4.13 \times 10^{-10} W^{5.22} /$$
$$(1 + 0.06 W^7)^{0.456} (1 + 1.68 \times 10^{-3} W^4)^{0.097} \quad (B-8)$$

Avalanche coefficient

$$\frac{\alpha_i}{N} = 3.76 \times 10^{-15} W^{8.7} / (1 + 2.92 \times 10^{-4} W^5)^{1.412} \quad (\text{B-9})$$

Three body dissociative attachment

$$\frac{\alpha_{3A}}{N^2} = 2.78 \times 10^{-31} / (1 + 12.5W) \quad (\text{B-10})$$

Two body dissociative (electron-ion) recombination

$$\frac{\alpha_r}{N_{O_2}^+} = 2.1 \times 10^{-7} \left(\frac{0.026}{W} \right)^{0.63} \quad (\text{B-11})$$

Two body dissociative attachment

$$\frac{\alpha_{2A}}{N} = 4.85 \times 10^{-12} / (1 + 3.45W^{-4.8})^{1.29} \quad (\text{B-12})$$

$$v_m = v_{mn} + v_{mi} \quad (\text{B-13})$$

$$\alpha = \alpha_i - \alpha_{3A} - \alpha_{2A} - \alpha_r \quad (\text{B-14})$$

Impact ionization rate

$$R_I = \frac{4\pi e^4 ZN}{(1.6 \times 10^{-12}) \phi_e m_e \beta c} \left[\ln \left(-\frac{m_e \beta^2 c^2 T_e \gamma^2}{\phi_e^2} \right) - \beta^2 \right] \quad (\text{B-15})$$

electrons/cm³/sec

In these equations

T_e = beam electron energy

Z = 7.2, effective atomic number for air

m_e = electronic rest mass

c = speed of light

β = v/c

γ = $(1-\beta^2)^{-1/2}$

ϕ_e = empirical factor and is 86 eV

This form for the impact ionization rate is found from the classical stopping power formula for relativistic electrons (Ref 35), and by assuming that, for every 86 eV of energy lost, one ion-pair is immediately formed. This assumption is consistent with the observation that, after cascade ionization is completed, one ion-pair is produced for every 34 eV lost by the beam electron (Ref 36). The parameters ν_{mn} , ν_e , α_i , α_{3A} , and α_{2A} are the same as those originally developed by Wittwer (Ref 19), but the parameters ν_{mi} and α_r were added to include the effects of higher electron densities. The electron-ion collision frequency, ν_{mi} , is adopted from Spitzer (Ref 32) and Lee (Ref 8), while the dissociative recombination rate, α_r , is taken from the DNA Reaction Rate Handbook (Ref 43). Figures 28 and 29 plot the parameters for sea level density air.

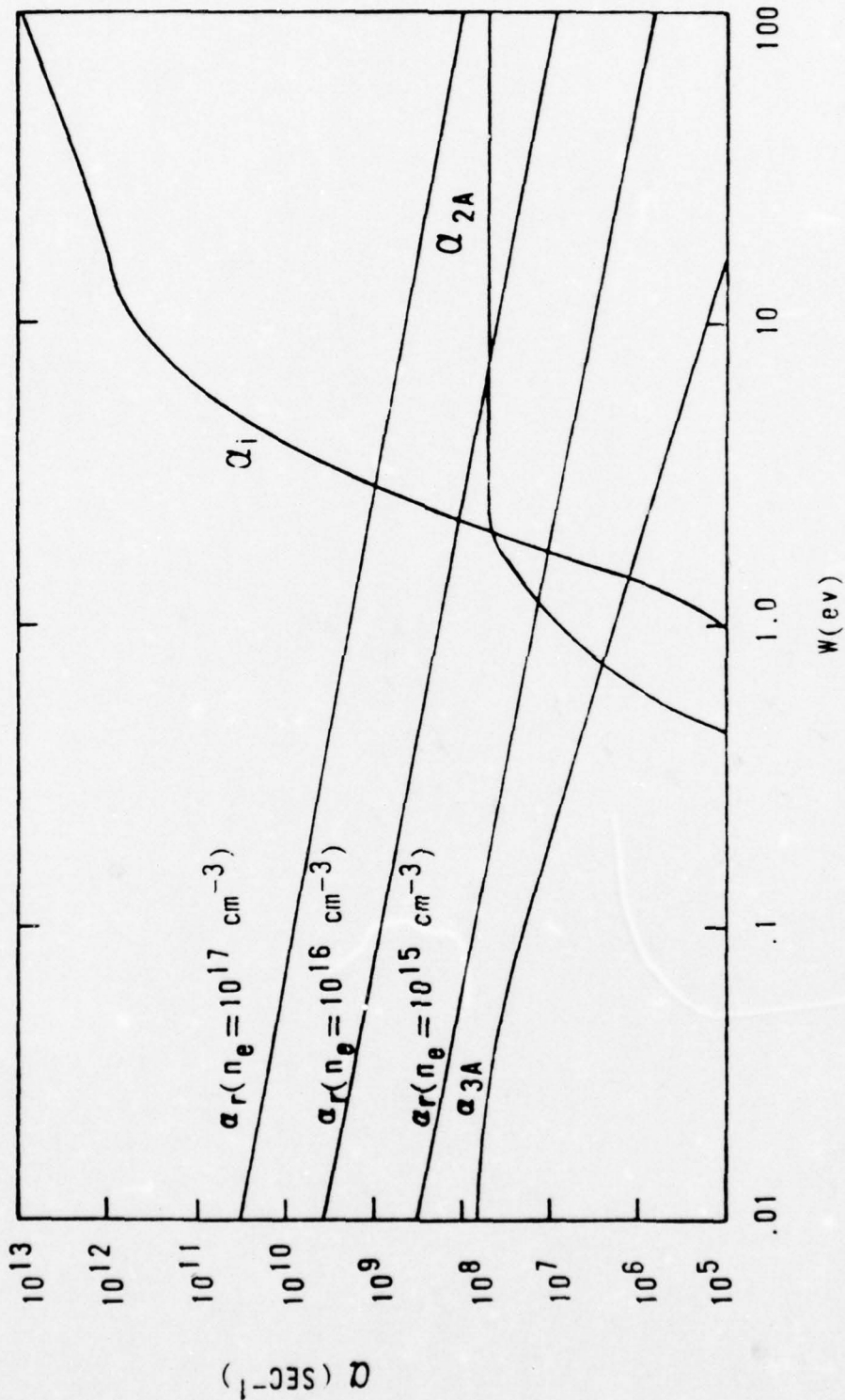


Figure 28. Avalanche, Attachment, and Recombination Coefficients

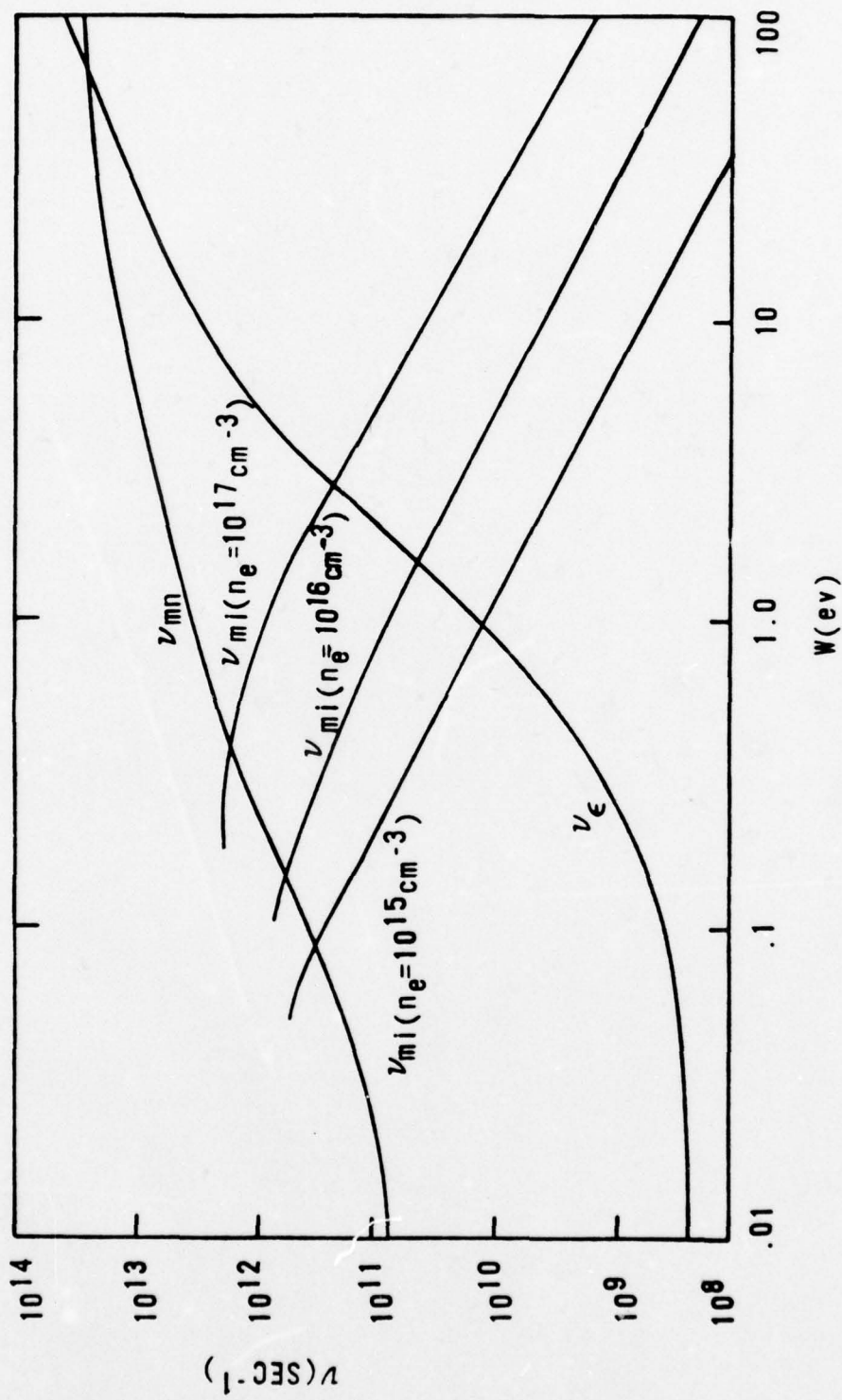


Figure 29. Collision Frequencies

In a series of papers Phelps and others (Refs 44-48) developed a method for calculating these empirical parameters for various mixtures of gases. His goal was to determine the unknown cross-sections. His method was to employ a Boltzmann code, solve for the equilibrium distribution function and, from this, calculate the experimentally observed parameters. The unknown cross sections were varied until the calculations agreed with experimental data. From these calculated values of empirical parameters Wittwer has developed the fits for air.

Other sources indicate a fair agreement with the parameters of the fluid model as given by Wittwer. For example, the DNA Reaction Rate Handbook (Ref 43) gives a value for the momentum transfer collision frequency at a one electron volt energy of $1.7 \times 10^{12} \text{ sec}^{-1}$. The fluid model value of the collision frequency given here is $2.7 \times 10^{12} \text{ sec}^{-1}$. As a further example of how the collision frequencies vary between models, Figure 30 compares the energy dependence of the collision frequencies of the DNA Reaction Rate Handbook value to those values of the fluid model.

Recently, Radasky (Ref 28) has published Longmire's fit to experimental data for the avalanche (ionization) rate as a function of the electric field for sea level conditions. The fit is

$$\alpha_i = (5.7 \times 10^8 y^5) / (1 + 0.3y^{2.5}) \quad (\text{B-16})$$

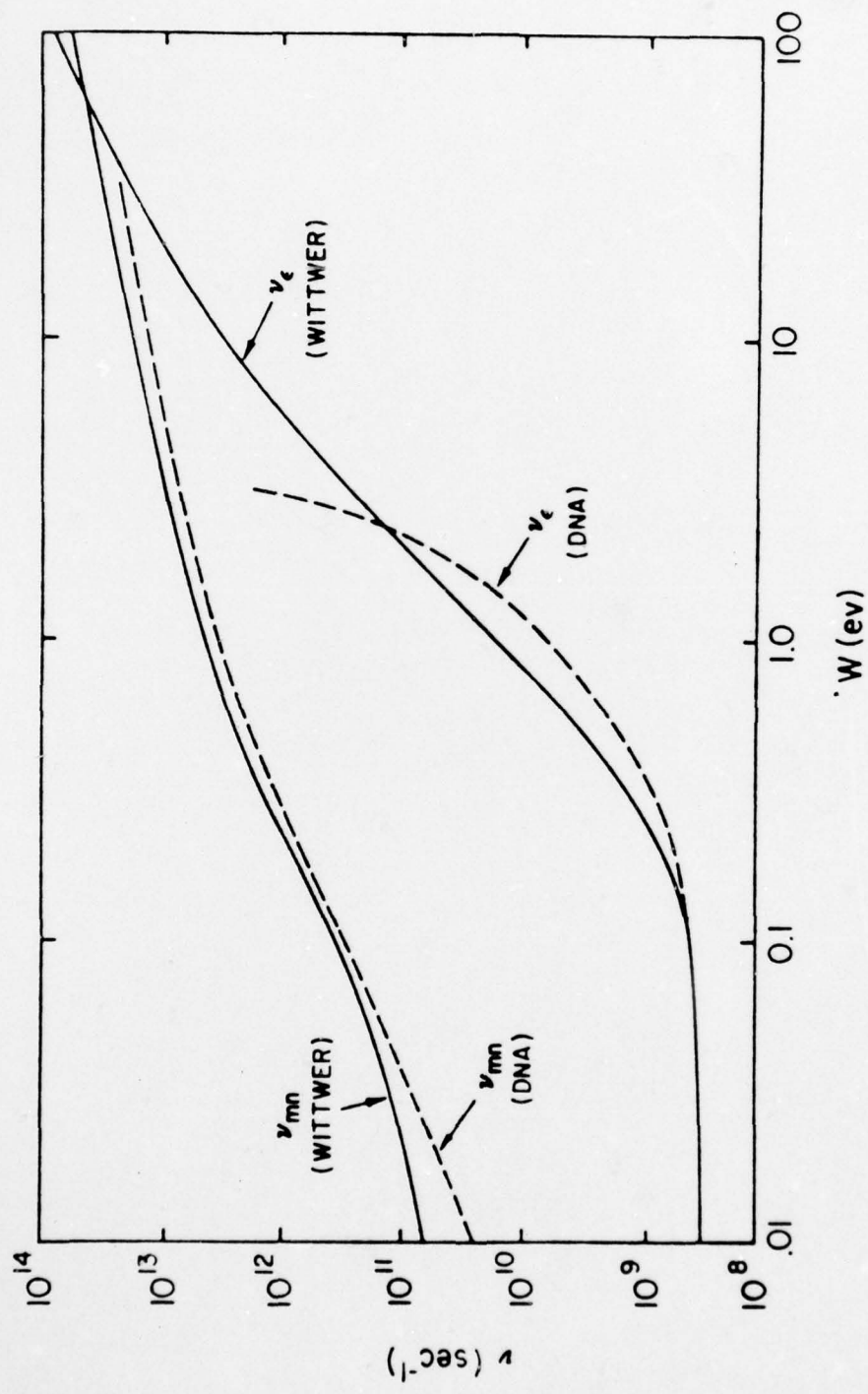


Figure 30. Comparison of Collision Frequency Models

where

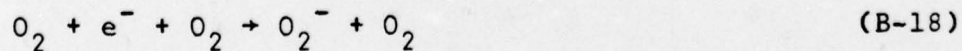
$$y = \frac{|\vec{E}| \text{ (sV/cm)}}{100}$$

Employing the equilibrium relationship between the electric field and characteristic energy for air, from Wittwer (Ref 19),

$$W(\text{ev}) = 2.5 \times 10^{-2} (1 + 0.11(EN_0/N)^{3.6})^{0.658} /$$
$$(1 + 5.65 \times 10^{-5} (EN_0/N)^5)^{0.37} \quad (\text{B-17})$$

allows a direct comparison between the two ionization coefficients. Figure 31 is a plot of the two rates. Notice that below 5 eV the Longmire model predicts an ionization coefficient almost twice that of Wittwer's. Above 10 eV the two fits rapidly diverge.

The dominant three body dissociative attachment reactions have been delineated by Radasky (Ref 28). They are



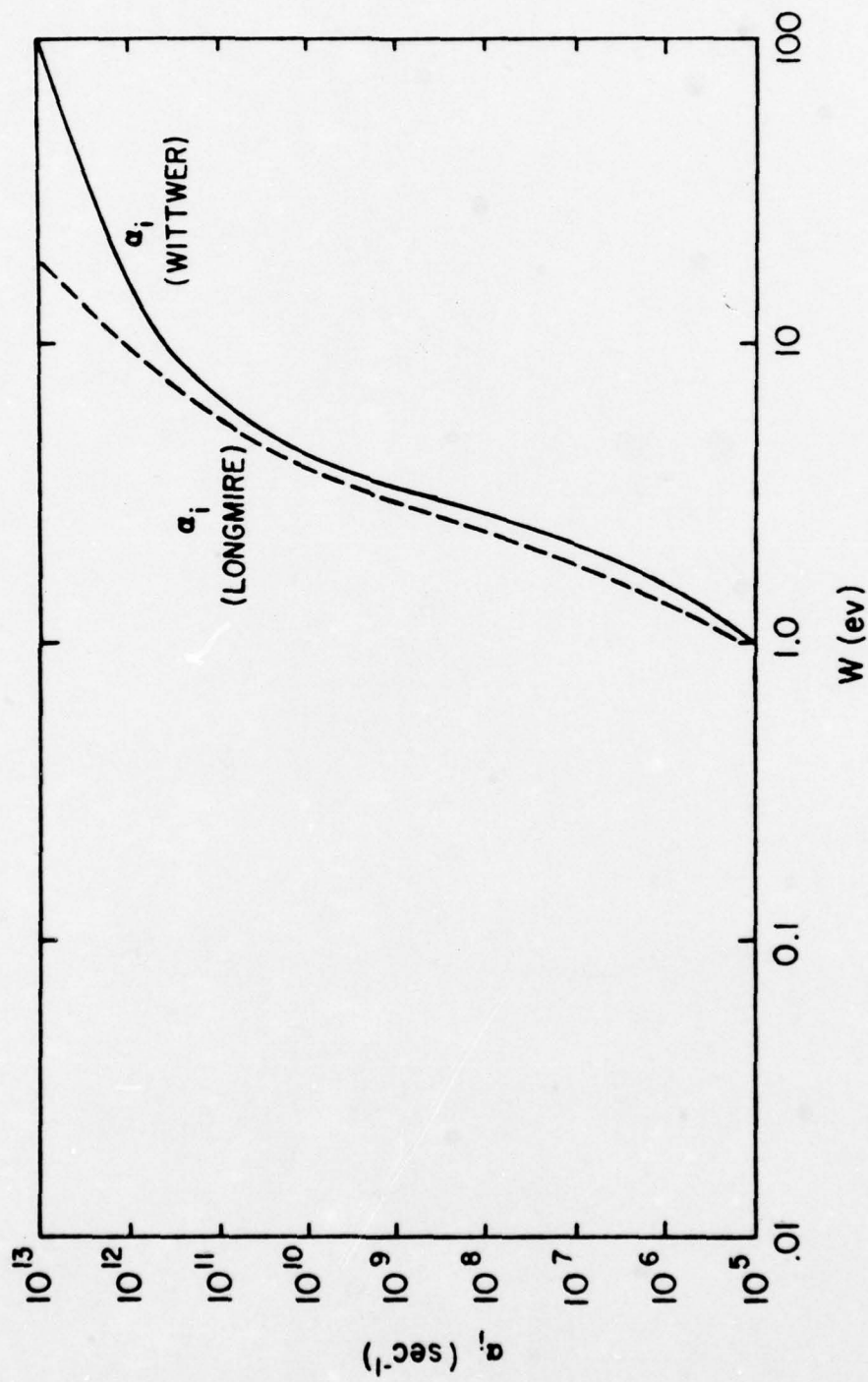


Figure 31. Comparison of Avalanche Models



with respective reaction rates (DNA Reaction Rate Handbook),

$$\frac{\alpha_1}{(N_{\text{O}_2})^2} = 1.85 \times 10^{-30} \text{ cm}^6/\text{sec} \quad (\text{B-21})$$

$$\frac{\alpha_2}{N_{\text{N}_2} N_{\text{O}_2}} = 1.0 \times 10^{-31} \text{ cm}^6/\text{sec} \quad (\text{B-22})$$

$$\frac{\alpha_3}{N_{\text{O}_2} N_{\text{H}_2\text{O}}} = 1.4 \times 10^{-29} \text{ cm}^6/\text{sec} \quad (\text{B-23})$$

for a neutral particle temperature of 300°K. These rates were determined by experiments in which the electrons and neutrals were in thermal equilibrium, so the dependence on electron energy is not given. Assuming a mixture of 80% N₂ and 20% O₂ the first two attachment rates combine to

$$\alpha_{1,2} = 6.4 \times 10^7 \text{ sec}^{-1} \quad (\text{B-24})$$

at sea level density. The maximum fraction of the air that is water vapor (100% relative humidity) is 0.07. With this fraction the attachment rate for the third reaction is

$$\alpha_3 = 1.4 \times 10^8 \text{ sec}^{-1} \quad (\text{B-25})$$

Wittwer's three body attachment rate for thermal electrons at 300°K gas temperature is

$$\alpha_{3A} = 2 \times 10^8 \text{ sec}^{-1} \quad (\text{B-26})$$

For most cases of interest in this study, however, the two body attachment rate and the recombination rate dominate.

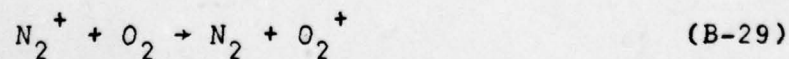
The two body dissociative recombination reaction that is employed in the fluid model is



with the reaction rate

$$\frac{\alpha_r}{N_{O_2^+}} = 2.1 \times 10^{-7} \left(\frac{0.026}{W} \right)^{0.63} \quad (\text{B-28})$$

Since the positive ion charge transfer reaction



occurs at a very rapid rate ($\sim 10^{10} \text{ sec}^{-1}$ at sea level density) virtually the only positive ions are O_2^+ ions.

The density of O_2^+ ions is equal to the density of electrons by charge balance if the density of negative ions produced by the attachment is small. For the cases considered in this study it can be proven that this is the case. Writing a rate equation for negative ions,

$$\frac{\partial n_-}{\partial t} = \alpha_A n_e - \Delta n_+ n_- \quad (B-30)$$

where

n_- = negative ion density

n_+ = positive ion density

α_A = total attachment rate

Δ = total ion-ion recombination rate

the asymptotic solution is

$$\frac{n_-}{n_e} < \frac{n_-^A}{n_e} = \frac{1}{2} \left\{ \left(1 + \frac{4\alpha_A}{n_e \Delta} \right)^{\frac{1}{2}} - 1 \right\} \quad (B-31)$$

where n_-^A is the asymptotic solution.

Using sea level values of α_A and Δ

$$\alpha_A \sim 2 \times 10^8 \text{ sec}^{-1}$$

$$\Delta \sim 2 \times 10^{-6} \text{ cm}^3/\text{sec}$$

$$n_e \sim 10^{16} \text{ cm}^{-3}$$

we have

$$\frac{n_-}{n_e} < .1 < 1 \quad (\text{B-32})$$

Thus

$$n_+ = N_{O_2^+} = n_e \quad (\text{B-33})$$

At densities lower than sea level densities the three-body dissociative attachment rate falls off very rapidly leaving only two body dissociative attachment to produce negative ions. However, even that attachment rate falls below 10^7 sec^{-1} at a factor of twenty reduction below sea level density. Since pulse lengths are typically considered to be on the order of 10^{-7} seconds in length, or less, the attachment process is negligible within the pulse for densities one-twentieth, or lower, of sea level density.

The reaction



is the primary reaction considered by Wittwer in finding the net two body dissociative attachment rate. Johnston

(Ref 11) employs a reaction rate which is vanishingly small, while Radasky (Ref 28) does not even include the reaction for EMP calculations. Experimental measurements by Fite and Brachman (Ref 49) and theoretical calculations by O'Malley (Ref 50) of the reaction cross section as a function of electron temperature are consistent with Wittwer's reaction rate.

Analytic Approximation

The set of five fluid equations, plus the auxiliary equations for the empirical parameters form a set that must be solved numerically, if all effects are to be considered. Yet, for many cases of interest in this work, certain approximations yield analytic results which permit an adequate description of the system.

Written in vector form, equations (B-2) and (B-3) are

$$\frac{\partial \vec{v}}{\partial t} = \frac{e\vec{E}}{m_e} - (\nu_m (W) + \alpha_T) \vec{v} \quad (\text{B-35})$$

For sea level conditions most of the pulse parameters considered in this work produce electron energies on the order of one eV. This value of energy yields a collision frequency of $2.7 \times 10^{12} \text{ sec}^{-1}$. For large values of n_e ($>10^{13} \text{ cm}^{-3}$), α_T is much smaller than ν_m . Assuming a constant value of ν_m , for time scales much longer than $1/\nu_m$ the solution to (B-35) is

$$\vec{v} = \frac{e\vec{E}}{m_e v_m} \quad (\text{B-36})$$

Under these assumptions the electron drift velocity is parallel to the electric field and given by (B-36).

Additionally, since

$$\vec{J}_p = en_e \vec{v} = \frac{e^2 n_e}{m_e v_m} \vec{E} \quad (\text{B-37})$$

a plasma conductivity can be defined

$$\Sigma = \frac{|\vec{J}_p|}{|\vec{E}|} = \frac{e^2 n_e}{m_e v_m} \quad (\text{B-38})$$

Consequently, for these situations, the plasma current density in Maxwell's equations can be replaced by ΣE .

The electron density can also be estimated analytically for many cases of interest. Assuming a linearly rising beam density in the pulse head, zero lag time, and attachment and recombination times that are much longer than the pulse rise time, then (B-1) becomes, in the pulse rise portion,

$$\frac{\partial n_e}{\partial \tau} = R \frac{\tau}{\Delta t} \quad , \quad \tau < \Delta t \quad (\text{B-39})$$

where

$$\tau = t - z/\beta c$$

Δt = pulse rise time

One gets

$$n_e = \frac{R}{2\Delta t} \tau^2, \tau < \Delta t \quad (\text{B-40})$$

and

$$\Sigma = \frac{e^2 R}{m_e v_m} \frac{\tau^2}{2\Delta t} \quad (\text{B-41})$$

for a constant v_m .

In the main body of the pulse attachment and recombination processes cannot be ignored. Again assuming a zero ionization lag time,

$$\frac{\partial n_e}{\partial \tau} = R - \alpha_A n_e - \beta_r n_e^2, \tau > \Delta t \quad (\text{B-42})$$

where

$$\beta_r = \frac{\alpha_r}{n_e} \quad (\text{B-43})$$

This is just the Ricatti equation (Ref 51). The solution

is

$$n_e(\tau) = \frac{\exp(D_2 - D_1)(\tau - \Delta t) + AD_1/D_2}{\exp(D_2 - D_1)(\tau - \Delta t) + A} \left(\frac{D_2}{\beta_r}\right) \quad (\text{B-44})$$

where

$$A = - \left(\frac{n_e(\tau = \Delta t)\beta_r^{-D_2}}{n_e(\tau = \Delta t)\beta_r^{-D_1}} \right) \quad (\text{B-45})$$

$$D_1 = - \frac{\alpha_A}{2} \left[1 + \left(1 + \frac{4\beta_r R}{\alpha_A^2} \right)^{\frac{1}{2}} \right] \quad (\text{B-46})$$

$$D_2 = - \frac{\alpha_A}{2} \left[1 - \left(1 + \frac{4\beta_r R}{\alpha_A^2} \right)^{\frac{1}{2}} \right] \quad (\text{B-47})$$

for α_A and β_r constant.

The conclusion is drawn immediately that the electron density is bounded by

$$n_e \leq \frac{D_2}{\beta_r} = \frac{\alpha_A}{2\beta_r} \left\{ \left[1 + \frac{4\beta_r R}{\alpha_A^2} \right]^{\frac{1}{2}} - 1 \right\} \quad (\text{B-48})$$

Employing Wittwer's values of α_A at one eV and the author's value of β_r at one eV, for sea level densities

$$\alpha_A = 3.4 \times 10^7 \text{ sec}^{-1}$$

$$\beta_r = 2.1 \times 10^{-8}$$

and assuming an ionization rate of

$$R = 10^{25} \text{ electrons/sec}$$

we have, for a one MeV electron beam,

$$n_e = 2.1 \times 10^{16} \text{ cm}^{-3} \quad (\text{B-49})$$

This occurs on a time scale of roughly

$$\tau - \Delta t = \frac{3}{D_2 - D_1} = \frac{3}{\alpha_A} \left[1 + \frac{4\beta_r R}{\alpha_A^2} \right]^{-\frac{1}{2}} \quad (\text{B-50})$$

or

$$\tau - \Delta t = 3.3 \times 10^{-9} \text{ sec} \quad (\text{B-51})$$

For this case, the maximum conductivity is

$$\Sigma_{\text{max}} = 2.7 \times 10^{12} \text{ sec}^{-1} \quad (\text{B-52})$$

APPENDIX C
PROGRAM BEAM1

In this Appendix we discuss the actual numerical method that is used in program BEAM1 to solve the two-dimensional EM equations of Section II, and the ionization model equations of Section IV. We present the finite difference equations and the algorithms employed for their solution.

Finite Difference Equations

From Section II, the differential equations of the EM model are

$$\frac{\partial E_r}{\partial \tau} + 4\pi\Sigma E_r = \frac{\partial E_r^0}{\partial \tau} \quad (C-1)$$

$$\frac{1}{r} \frac{\partial}{\partial r} \left[r \left(\frac{\partial E_z}{\partial r} + \frac{1}{\beta c} \frac{\partial E_r}{\partial \tau} \right) \right] = \frac{4\pi}{c^2} \frac{\partial}{\partial \tau} (J_{bz} + \Sigma E_z) \quad (C-2)$$

$$\frac{1}{r} \frac{\partial}{\partial r} (r B_\theta) = \frac{4\pi}{c} \frac{\partial}{\partial \tau} (J_{bz} + \Sigma E_z) \quad (C-3)$$

Since the electric field is completely decoupled from the magnetic field, we only solve for the magnetic field after

the electric field is determined. The finite difference equations employed for the first two differential equations are

$$\begin{aligned} \frac{E_{ri}^{n+1} - E_{ri}^n}{\Delta\tau} + 4\pi \left(\frac{\Sigma_i E_{ri}^{n+1} + \Sigma_i E_{ri}^n}{2} \right) \\ = \frac{E_{ri}^{on+1} - E_{ri}^{on}}{\Delta\tau} \end{aligned} \quad (C-4)$$

$$\begin{aligned} \frac{E_{zi+1}^{n+1} + E_{zi-1}^{n+1} - 2E_{zi}^{n+1}}{(\Delta r)^2} + \frac{1}{r_i} \frac{(E_{zi+1}^{n+1} - E_{zi-1}^{n+1})}{2\Delta r} \\ + \frac{1}{\beta c r_i} \left(r_{i+1} \frac{\partial E_{ri+1}^{n+1}}{\partial \tau} \Big|^{n+1/2} - r_{i-1} \frac{\partial E_{ri-1}^{n+1}}{\partial \tau} \Big|^{n+1/2} \right) \\ = \frac{4\pi}{c} \left(\frac{J_{bzi}^{n+1} - J_{bzi}^n}{\Delta\tau} + \frac{\Sigma_i E_{zi}^{n+1} - \Sigma_i E_{zi}^n}{\Delta\tau} \right) \end{aligned} \quad (C-5)$$

B_θ is found by Simpson's rule integration (Ref 24) over r of equation (C-3). Here the i subscript denotes the i th grid point in the radial direction and the subscript, n , denotes the n th grid in the τ direction.

The finite difference equations for the ionization model equations are constructed by noting that the form of

each of the differential equations is

$$\frac{\partial f(r, \tau)}{\partial \tau} = p(r, \tau) f(r, \tau) + h(r, \tau) \quad (C-6)$$

Integrating over one time step,

$$f_i^{n+1} = f_i^n e^{\bar{p}\Delta\tau} + \bar{h} (1 - e^{\bar{p}\Delta\tau}) \quad (C-7)$$

where

$$\bar{p} = \frac{1}{2} (p(r_i, \tau_{n+1}) + p(r_i, \tau_n)) \quad (C-8)$$

$$\bar{h} = \frac{1}{2} (h(r_i, \tau_{n+1}) + h(r_i, \tau_n)) \quad (C-9)$$

The subscript i denotes the i th radial position, and the subscript n denotes the n th grid point in the τ direction, as before.

These finite difference equations have certain characteristics that we point out here. The first point to notice is that all parameters are evaluated at the same grid points. Since the electric field and the conductivity are related through the plasma electron energy, the equations are iterated for consistency. Secondly, we notice that, to evaluate $(\Sigma E_r)_i^{n+1/2}$ we take the mean of $(\Sigma E_r)_i^n$

and $(\Sigma E_r) i^{n+1}$. This results in second order accuracy in the difference equation for E_r . The third important point is that an implicit differencing scheme is used in the axial field difference equation. We do this to alleviate the obvious linear instability of an explicit scheme (Ref 24). However, since the axial field is coupled to the conductivity in a non-linear fashion numerical instability is still possible, and has been observed for some sets of beam parameters not included in this study. The instability results in catastrophic disruption of the calculation. Due to the complex nature of the differential equations we have not been able to perform a stability analysis, or otherwise determine stability criteria.

Solution Algorithm

The finite difference equations for the EM fields are solved in a straightforward manner. In equation (C-4) the conductivity, vacuum values of the field, and values of E_{ri}^n are known, so we directly solve for E_{ri}^{n+1} . With the radial electric field just determined, and the conductivity and beam current density known, equation (C-5) becomes a tri-diagonal equation for E_z in r when written in matrix form. This we solve by a method of back substitution (Ref 24).

As previously mentioned, in order to maintain consistency between the electric field and the conductivity, solutions are iterated. The iteration procedure is to

guess a value of the current density, \vec{J} , from which we find the conductivity by Ohm's law, then calculate new values of \vec{E} and \vec{J} . Iterations continue until no appreciable change between iterates is observed. Normally, only four to six iterations are necessary to achieve convergence. We illustrate this procedure in Figure 32.

To achieve the rapidity of convergence that we see, and to minimize computing time, we use a scheme to accelerate convergence. This procedure, sometimes called "Aitken's Δ^2 -Method" (Ref 52), is given by

$$\bar{X}_n = \frac{X_{n+1}^2 - X_n X_{n+2}}{2X_{n+1} - X_n - X_{n+2}} \quad (C-10)$$

where

$$X_{n+1} = f(X_n) \quad (C-11)$$

and \bar{X}_n is the new estimate for X_n . This method is applied to the radial and axial components of the fields separately, and at each radial position. One could have used a variation of this method that is applied to all radial positions simultaneously, but this would have greatly increased computing time.

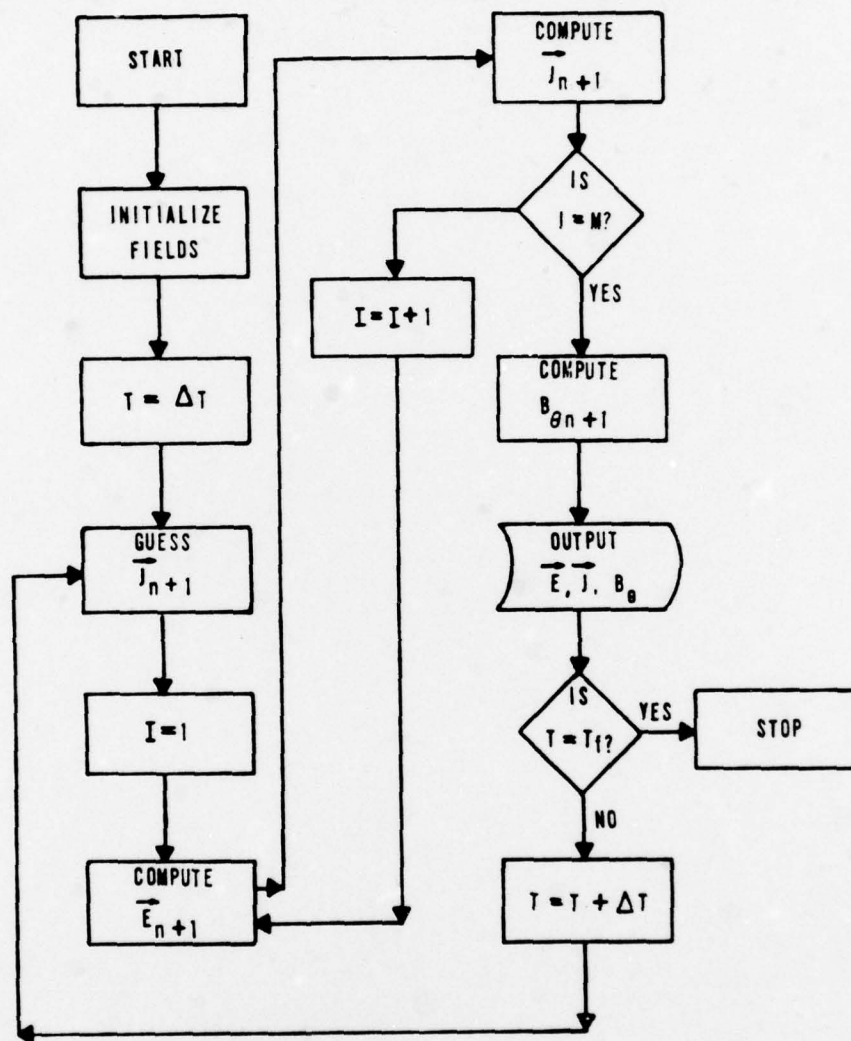


Figure 32. Flow Chart for Program BEAM1

Iterations are also applied to the ionization model equations. A look at the equations (Section IV) shows that they are all coupled through the plasma electron energy, so iterating through the equations provides a consistent solution. This procedure is illustrated in Figure 33.

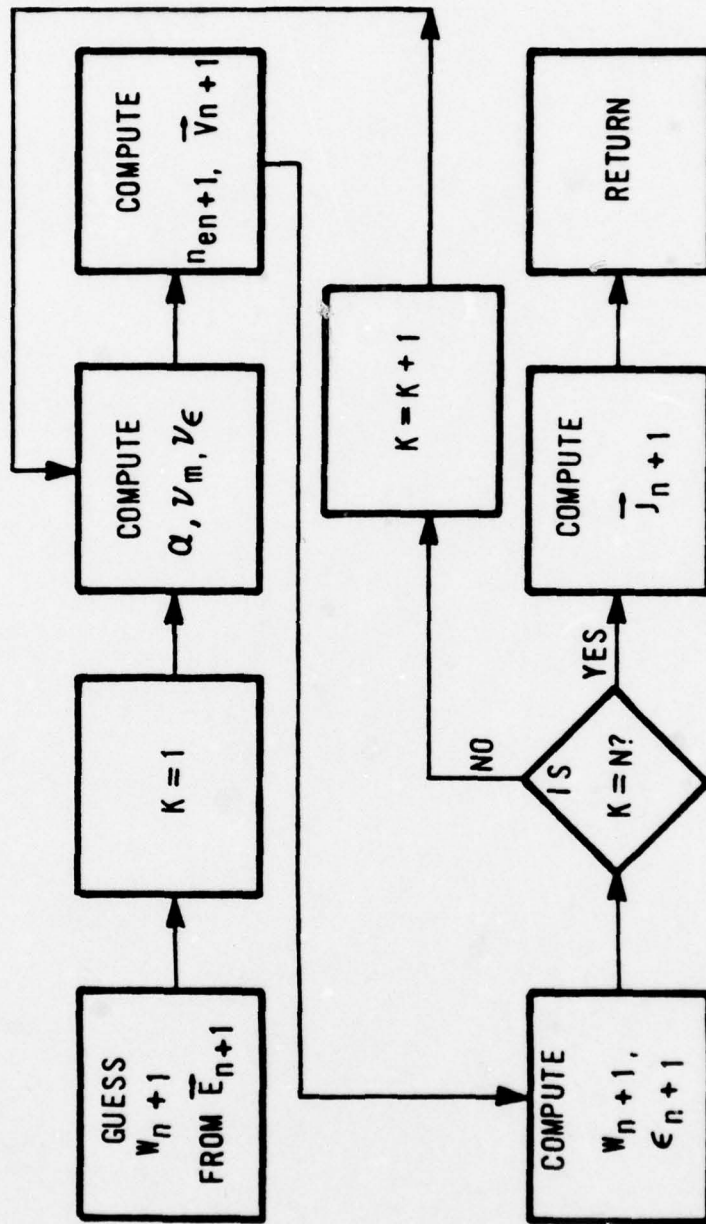


Figure 33. Flow Chart for Solution of Ionization Model Equations

APPENDIX D

PROGRAM BEAM2

In this Appendix we present the numerical method used in program BEAM2 for solving the one-dimensional EM model equations of Section III. Since the one-dimensional model is considerably simpler than the two-dimensional model, the numerical method in program BEAM2 is considerably simpler than the numerical program in BEAM1. The interested reader is directed to Appendix C for a discussion of the numerical method for solving the ionization model equations.

From Section III, the pertinent equations are

$$\frac{\partial E_r}{\partial \tau} + 4\pi\Sigma E_r = \frac{\partial E_r^o}{\partial \tau} \quad (D-1)$$

$$\frac{\partial J_{pzo}}{\partial \tau} + \frac{J_{pzo}}{\tau_{mo}} = - \frac{\partial J_{bzo}}{\partial \tau} + \frac{c}{\pi a \beta} \frac{\partial E_r(a)}{\partial \tau} \quad (D-2)$$

$$E_z(r) = \frac{J_{pzo}}{\Sigma_o} \left[1 - \frac{\ln(1+r^2/a^2)}{\ln(1+b^2/a^2)} \right] \quad (D-3)$$

$$B_\theta(r) = \frac{2I_b(r)}{cr} + \frac{2I_p(r)}{cr} \quad (D-4)$$

with

$$\tau_{m0} = \frac{\pi a^2 \Sigma_0 \ln(1+b^2/a^2)}{c^2} \quad (D-5)$$

$$I_b(r) = \frac{\pi r^2 J_{bzo}}{1+r^2/a^2} \quad (D-6)$$

and

$$I_p(r) = \frac{\pi r^2 J_{pzo}}{1+r^2/a^2} \left\{ 1 - \frac{[1 - (a^2/r^2) \ln(1+r^2/a^2)]}{\ln(1+b^2/a^2)} \right\} \quad (D-7)$$

The zero subscripts denote that the values of the parameter are taken at $r=0$.

Because there are only two differential equations, we have only two finite difference equations

$$E_r^{n+1} = [E_r^n (1-D_e) + E_r^{on+1} - E_r^{on}] / (1+D_e) \quad (D-8)$$

$$J_{pzo}^{n+1} = [J_{pzo}^n (1-D_m) - (J_{bzo}^{n+1} - J_{bzo}^n) + \frac{c}{\pi a \beta} (E_r^{n+1}(a) - E_r^n(a))] / (1+D_m)$$

where

$$D_e = 2\pi \Sigma^{n+\frac{1}{2}} \Delta\tau \quad (D-10)$$

$$D_m = \frac{c^2 \Delta\tau}{2\pi a^2 \Sigma_o^{n+\frac{1}{2}} \ln(1+b^2/a^2)} \quad (D-11)$$

Here the superscript n denotes the n th grid point in the r direction, and the zero subscripts again denote the on-axis values of the parameters.

We solve equation (D-8) at $r=a$ since the radial electric field must be known at that point to find the on-axis plasma current density in (D-9). Conductivity is also evaluated at $r=a$ for use in finding the radial field in (D-8), but the on-axis value in (D-9) is inferred from the assumed Bennett variation of conductivity. Since conductivity depends upon field strength we also evaluate the axial electric field at $r=a$.

As in program BEAM1, program BEAM2 iterates to maintain consistency between the electric field and the conductivity. The same accelerated converge technique that is used in BEAM1, and described in Appendix C is applied here to the radial electric field and the plasma current density. Normally six iterations are sufficient for convergence of all parameters to less than 1% difference between iterates. The numerical technique described here appears quite stable. No evidence of numerical instability has been observed.

APPENDIX E
PROGRAM MONTY

In this Appendix we examine the numerical program that simulates the interaction of the plasma electrons with air molecules, and an externally applied electric field. The program, named Monty, simulates the collisions of the plasma electrons against the air molecules by randomly sampling over the interaction cross sections. Hence, it employs Monte Carlo techniques. We also present a catalogue of the experimental and theoretical cross sections used in the simulation.

Simulation Method

The most difficult aspect of the simulation is the extraordinarily large number of possible interactions between the plasma electrons and air molecules; so many that a great deal of simplification is necessary to make a mathematically tractable problem. Since N_2 comprises almost 80% of the air molecules the assumption is made that the air consists wholly of N_2 molecules. This appears to be a reasonable assumption since O_2 , comprising about 20% of the air molecules, has excitation and ionization cross sections that are similar in many respects to N_2 . Program MONTY, which uses these cross sections, is limited by

available computing time to short time scales (10^{-8} second or less) and low pressures (76 Torr or less) so the only interactions considered are

1. Molecular vibrational excitation
2. Electronic excitation
3. Ionization
4. Elastic Scatter

In this study the energies of interest lie above one electron Volt so rotational interactions are not included. Other possible interactions, such as attachment and recombination, occur on much longer time scales and are of no consequence for the parameters considered in program MONTY.

We achieve more simplifications by restricting the problem to be zero-dimensional in real space (homogeneous), time dependent, and one-dimensional in velocity space. All spatial variations are ignored. Thus, the trajectories of the plasma electrons are computed in velocity space from the force equation,

$$\frac{dv}{dt} = \frac{eE}{\gamma(v)m} \quad (E-1)$$

The electric field is externally applied, and is assumed to always act parallel to the velocity vector. Obviously, by reducing the dimensionality of the simulations some information is lost. But our goal is to generate the history of the ionization cascade. This history is relatively insensitive to the spatial distribution of particles.

To sample over the cross sections we employ the "Golden Rule" of Monte Carlo to generate interaction probabilities in a continuous manner. Let P be the probability of interaction at time t . P and t are related by

$$P = e^{-N\sigma_T vt} \quad (\text{E-2})$$

where N is the molecular number density of air, v is the plasma electron speed, and σ_T is the total interaction cross-section, and is a sum of the total vibrational excitation, electronic excitation, ionization, and elastic scatter cross sections. The probability of an interaction occurring between the initial time and t is found by integrating (E-2) over time and normalizing. This is often called the "cumulative" probability, and is

$$C_N = 1 - e^{-N\sigma_T vt} \quad (\text{E-3})$$

Here we assume that σ_T and v are constants. We also note that the function, C_N , is normalized so that it lies on the interval (0,1). We determine the time of interaction by generating a random number, ξ , setting that number equal to the cumulative probability, and inverting to find t ,

$$t = - \frac{\ln(1-\xi)}{N\sigma_T v} \quad (\text{E-4})$$

After an interaction is determined to occur the type of interaction, and the velocity and direction of the interacting particles must also be determined. The type of interaction is chosen by randomly sampling over the discrete probability distribution composed of the relative probabilities of each of the four possible interactions. These probabilities are a function of the electron energy, and are updated by the program after each time step. Once the type of interaction is chosen the energy lost in the interaction is determined by randomly sampling over the partial cross sections for that interaction. From the energy lost, and knowing the type of interaction, a new velocity is calculated for the plasma electron. If an ionization occurs, both the speed of the parent and daughter electron are specified. For all interactions direction is not specified by random sampling, but by predetermined rules. For example, for elastic scatter of plasma electrons with a kinetic energy of 100 eV, or less, off a nitrogen molecule, half the interactions result in forward scattered electrons. By specifying that every other electron be scattered in the forward direction, and every other electron be scattered in the backward direction we maintain the directional partition.

Solution Algorithm

In program MONTY velocity space is split into a number of bins of variable length. Normally, 90 to 100 bins are

employed, depending upon the beam electron energy being considered. The high energy electrons produced by impact ionization necessitate a bin structure of variable length. The minimum width of the bin is 0.5 electron Volts at an energy of one electron Volt, and increases up to a maximum bin width of 300 keV for a one MeV beam electron. The variable bin structure gives the necessary resolution for energies below 100 eV where many different interactions occur, yet it spans the range of electron energies.

The time domain is also discretized. Electron histories are followed through a given time step, and at the end of that time step the accumulated weight of every electron in each bin is scored. Thus, scoring occurs at the end of every time step, and a new distribution function is calculated at the end of each time step.

We here summarize the algorithm used in program MONTY.

1. The electron distribution produced by beam electron impact ionization is scored at time $t=0$. This is the source for the ionization cascade.

2. A sample of electrons is taken from each bin. The same number is sampled from each bin and scoring weights are adjusted for the relative density of electrons in each bin.

3. The electrons are accelerated by the electric field, and interactions are determined by random sampling. Depending upon the size of the time interval and the probability of interaction, an electron may encounter several

interactions within a time step, or, possibly, it may encounter no interactions at all. For each interaction new state variables are determined for the interacting electron. If an ionization event occurs the state variables plus the birth time of the newly born electrons are stored. After all initially sampled electron histories are completed, the histories of the newly born electrons are completed for that time step.

4. At the end of the time step the accumulated scoring weight of each electron is scored in the bin that is in at the end of the time step. This generates a new electron distribution.

5. We then repeat the procedure, beginning with step 2, the desired number of times.

Experimental Cross Section Data

A large amount of experimental cross-section measurements are available for low energy electrons (< 1 KeV) onto N_2 . The data employed in program MONTY are listed in Tables IV through VII. The vibrational, excitation, ionization, and momentum transfer cross-section are taken from Englehardt, Phelps and Risk (Ref 46), and the electronic excitation cross sections are taken from Rees and Jones (Ref 53). All cross sections are in units of 10^{-16} cm^2 , and all energies are in units of electron volts. Figure 34 is a plot of the total cross-sections, and Figure 35 is a plot of their respective reduced reaction rates (σv).

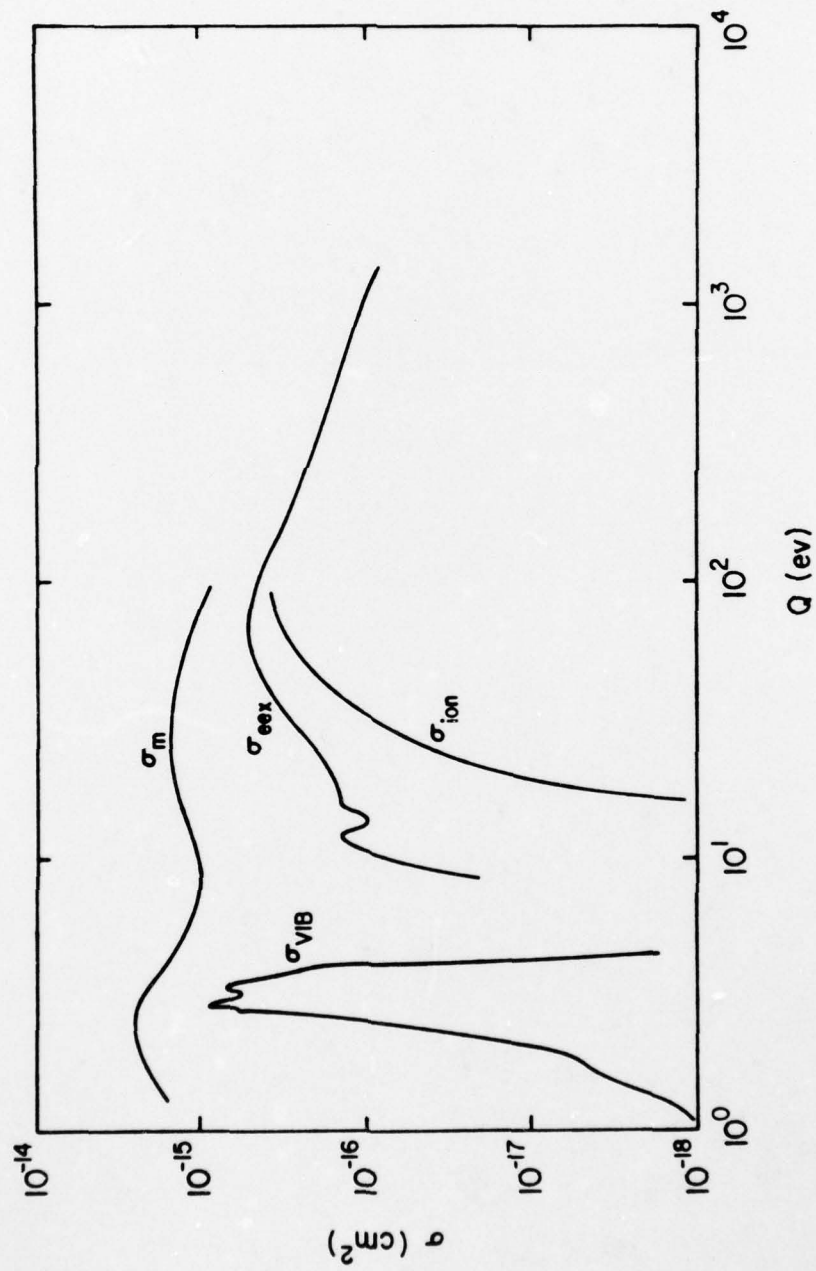


Figure 34. Experimental Molecular Nitrogen Cross Sections

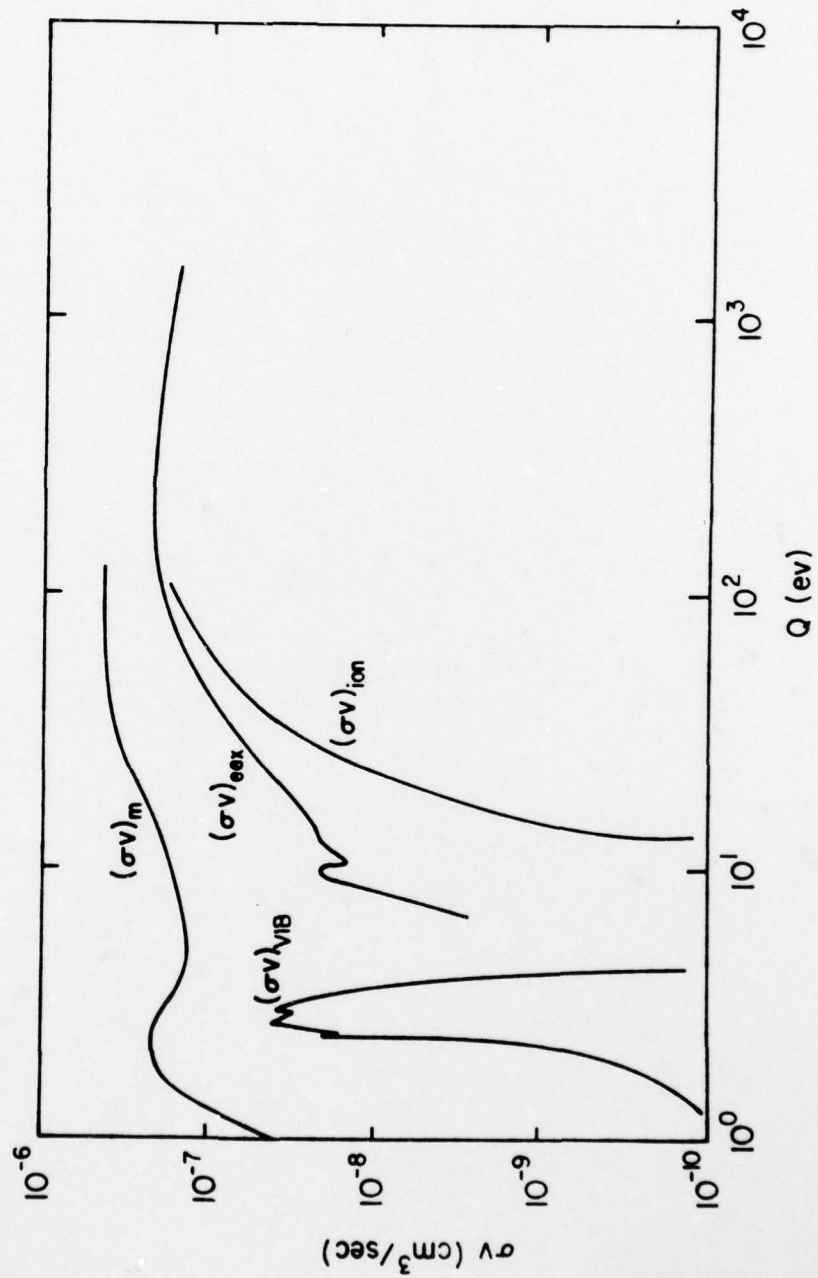


Figure 35. Experimental Molecular Nitrogen Reaction Rates

There appears to be significant disagreement in the momentum transfer cross sections as measured by Phelps (Ref 46) and as measured by Shyn (Ref 54). It does appear, however, that above energies about 50 eV the angular distributions of the scattered electrons becomes decidedly non-isotropic, with forward scatter predominating. For electron energies below 50 eV the momentum transfer cross section and the elastic scatter are virtually the same. In order to simplify the numerical program, the equality of the cross sections is assumed to extend up to 100 eV. Considering the disagreement in the data between Phelps and Shyn it is felt that the error introduced by extending the region of equality up to 100 eV is less than the uncertainty in the cross sections.

Theoretical Cross Sections

Data giving secondary electron distributions produced in the ionization process is conspicuously absent from the following tables. Only recently have a few measurements been made. Toburen (Ref 55) has measured the energy and angular distributions of secondary electrons produced from ionization of N_2 gas by proton impact up to 1.7 MeV in energy. Opal, Beatty, and Peterson (Ref 56) performed similar measurements, but with electrons as the projectiles. Energy and angular distributions were found for 50 to 2000 eV electrons onto various gases, including N_2 . Later, Green and Sawada (Ref 57) published analytic fits to the secondary distributions of Opal.

The data that exists, though, is limited to projectile energies quite a bit lower than the energy of relativistic particles. Very recently, Porter, Jackman, and Green (Ref 12) published analytic forms of the secondary electron distributions produced by either electrons or protons, valid from the region of experimental data up to one GeV kinetic energy. Beyond the region of experimental data (2000 eV for electrons and 1.7 Mev for protons onto N_2) analytic forms were made to fit the theoretical calculations for the secondary electron distribution.

The electron distribution is,

$$\frac{d\sigma_i}{dQ} = \sum_j \frac{F_j(T)}{(m_e \beta^2 c^2 / 2)} (K \Gamma_e^2(T) \{ \ln[4(\frac{\gamma^2 m_e \beta^2 c^2 C_j}{2 I_j})] - \beta^2 \}^* \\ \{ \frac{1}{(Q-Q_{oe})^2 + \Gamma_e^2(T)} - \frac{B(T)}{(Q-Q_1)^2 + \Gamma_1^2} \} \\ + \frac{N_e \pi e^4}{p^2} \{ \frac{1}{(T-Q-I_j)^2 - \Gamma_2^2} + \frac{1}{(T+m_e c^2)^2} \\ - \frac{2Tm_e c^2 + (m_e c^2)^2}{(T+m_e c^2)^2} \frac{1}{(Q+I_j)(T-Q-I_j)+T_2^2} \} \quad (E-5)$$

with

σ_i = ionization cross section

Q = secondary electron energy

$\frac{d\sigma_i}{dQ}$ = secondary electron distribution

T = pulse particle kinetic energy

m_e = electron rest mass

β = v/c

γ = $1 + T/mc^2$

N_e = Z number for $N_2 = 14$

p = 1.6×10^{-12} eV/erg

The rest of the parameters are given in Table VIII.

This form can be integrated to give the total ionization cross section

$$\sigma_i = \int_0^{Q_m} \frac{d\sigma_i}{dQ} dQ \quad (E-6)$$

where $Q_m = T/2$, and is the maximum secondary electron energy.

Thus,

$$\sigma_i = \sum_i \frac{F_i(T)}{(m_e \beta^2 c^2 / 2)} (K \Gamma_e^2(T) \{ \ln[4(\frac{\gamma^2 m_e \beta^2 c^2 C_i}{2 I_j})] - \beta^2 \}$$

$$* \{ \frac{1}{\Gamma_e} [\tan^{-1}(\frac{Q_m - Q_{oe}}{\Gamma_e}) + \tan^{-1}(\frac{Q_{oe}}{\Gamma_e})]$$

$$\begin{aligned}
& -\frac{B(T)}{\Gamma_1} \left[\tan^{-1} \left(\frac{Q m_e - Q_i e}{\Gamma_1} \right) + \tan^{-1} \left(\frac{Q_1}{\Gamma_1} \right) \right] \\
& + \frac{N_e \pi e^4}{p^2} \left\{ \frac{1}{\Gamma_2} \tan^{-1} \left(\frac{T - I_j}{\Gamma_2} \right) + \tan^{-1} \left(\frac{T - Q m_e - I_j}{\Gamma_2} \right) \right. \\
& + \frac{Q m_e}{(T + m_e c^2)^2} - \frac{2 T m_e c^2 + (m_e c^2)^2}{(T + m_e c^2)^2} \frac{2}{\sqrt{q}} \\
& \left. * \left[\tanh^{-1} \left(\frac{T - 2I_j}{\sqrt{q}} \right) - \tanh^{-1} \left(\frac{T - 3I_j}{2\sqrt{q}} \right) \right] \right\} \quad (E-7)
\end{aligned}$$

where

$$q = 4 \left[I_j (T - I_j) + \Gamma_2^2 \right] + (T - 2I_j)^2$$

Figure 36 is a comparison of the experimental electron ionization cross section with the theoretical ionization cross sections for electrons.

Another useful bit of information that can be derived from the analytic forms of the secondary electron distribution function is the energy distribution function. Defining

$$f_i(Q, T) = \int_0^Q Q' \frac{d\sigma_i(Q', T)}{dQ'} dQ' \quad (E-8)$$

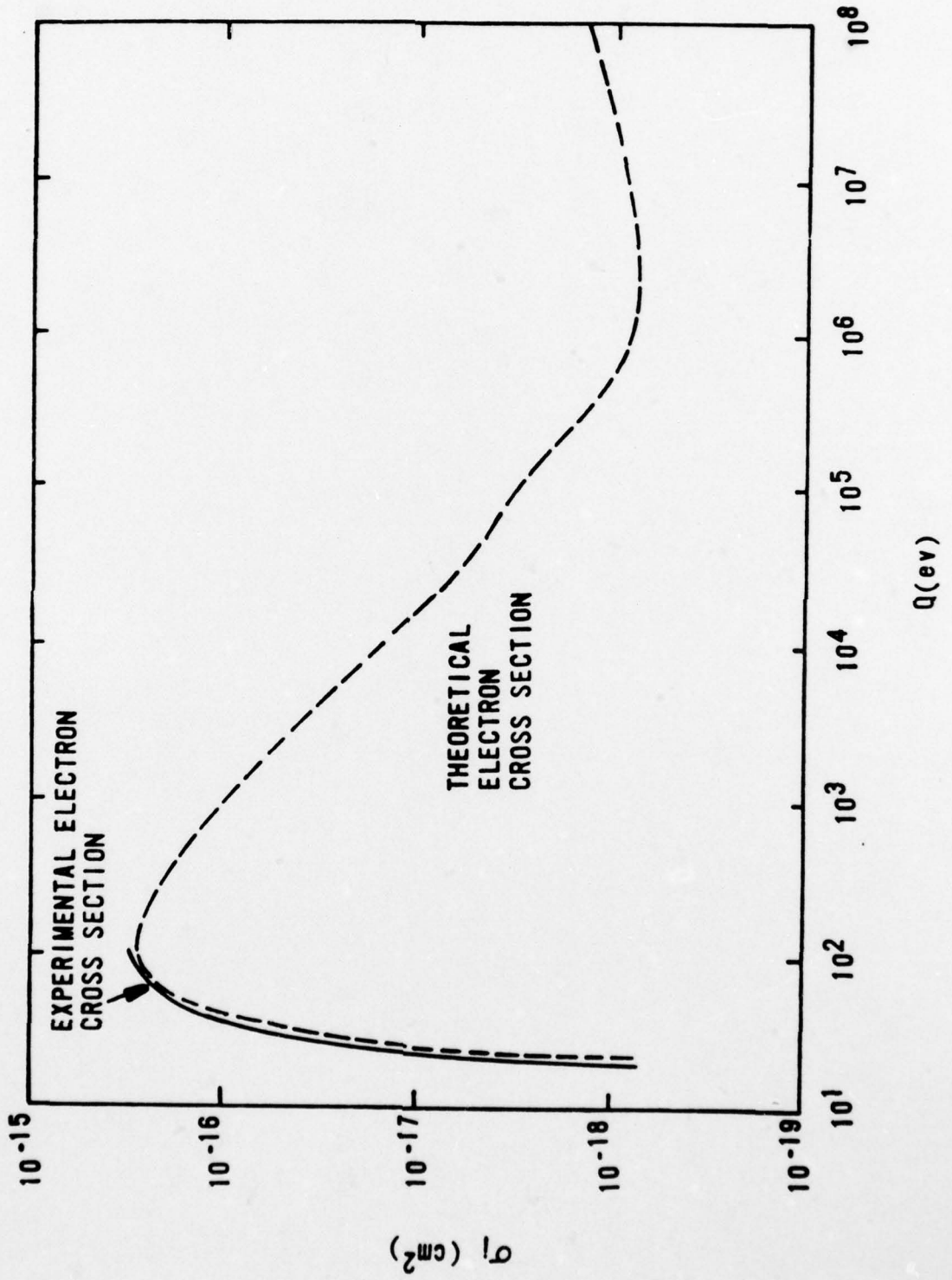


Figure 36. Comparison of Experimental and Theoretical Ionization Cross Sections for Molecular Nitrogen

we have,

$$\begin{aligned}
 f_i(Q,T) &= \sum_j \frac{F_j(T)}{(m_e \beta^2 c^2 / 2)} (K \Gamma_e^2(T) \{ \ln[4(\frac{\gamma^2 m_e \beta^2 c^2 C_i}{2 I_i})] - \beta^2 \}) \\
 & * \{ \frac{1}{2} \ln [\frac{(Q-Q_{oe})^2 + \Gamma_e^2}{Q_{oe}^2 + \Gamma_e^2}] + \frac{Q_{oe}}{\Gamma_e} [\tan^{-1}(\frac{Q-Q_{oe}}{\Gamma_e}) + \tan^{-1}(\frac{Q_{oe}}{\Gamma_e})] \\
 & - \frac{B(T)}{2} \ln [\frac{(Q-Q_1)^2 + \Gamma_1^2}{Q_1^2 + \Gamma_1^2}] - \frac{B(T)Q_1}{\Gamma_1} [\tan^{-1}(\frac{Q-Q_1}{\Gamma_1}) + \tan^{-1}(\frac{Q_1}{\Gamma_1})] \} \\
 & + \frac{N_e \pi e^4}{p^2} \{ \frac{1}{2} \ln [\frac{(Q+T-I_j)^2 \Gamma_2^2}{(T-I_j)^2 + \Gamma_2^2}] - (\frac{T-I_j}{\Gamma_2}) [\tan^{-1}(\frac{Q+T-I_j}{\Gamma_2}) \\
 & - \tan^{-1}(\frac{T-I_j}{\Gamma_2})] + \frac{Q^2}{(T+m_e c^2)^2} \\
 & - [\frac{2Tm_e c^2 + (m_e c^2)^2}{(T+m_e c^2)^2}] [\frac{1}{2} \ln (\frac{\Gamma_2^2 + I_j(T-I_j)}{-Q^2 + Q(T-2I_j) + \Gamma_2^2 + I_j(T-I_j)}) \\
 & - (\frac{T-2I_j}{-q}) (\tanh^{-1}(\frac{T-2I_j-2Q}{-q}) - \tanh^{-1}(\frac{T-2I_j}{-q})) \} \quad (E-9)
 \end{aligned}$$

with

$$q = -4 [\Gamma_2^2 + I_j(I-I_j) - (T-2I_j)^2]$$

Finally, the energy loss rate of a beam particle is given by

$$\frac{1}{N} \frac{dT}{dz} = - f_i(Q_{\max}, T) + \sigma_i \bar{I} + \sigma_e \epsilon_s \quad (\text{E-10})$$

where

\bar{I} = average ionization potential ≈ 16 ev

σ_e = excitation cross section

ϵ_e = average electronic excitation energy loss

At high energies (> 1 Kev) σ_e and σ_i are nearly equivalent for electrons since both cross sections vary approximately as (Refs 12, 58)

$$\sigma_i, \sigma_e \sim \frac{1}{m_e v^2} \quad (\text{E-11})$$

Additionally, at high energies, the energy loss per electronic interaction is

$$\epsilon_e = 14.4 \text{ ev} \quad (\text{E-12})$$

Calculations performed by Porter (Ref 12) indicate that the foregoing is true. Thus, restricting ourselves to high energies, and realizing the approximate nature of the argument, one arrives at

$$\frac{1}{N} \frac{dT}{dz} = - f_i(Q_{\max}, T) + \sigma_i \bar{\epsilon} \quad (\text{E-13})$$

where

$$\bar{\epsilon} = \bar{I} + \epsilon_e = 30.4 \text{ ev} \quad (\text{E-14})$$

The beam particle energy loss rate given by (E-13) can be compared with the semi-empirical stopping power formulas (Ref 29). For electrons

$$\frac{1}{N} \frac{dT}{dz} = \frac{2\pi e^4 Z}{m_e \beta^2 c^2} \left[\ln \left(\frac{\gamma^2 m_e \beta^2 c^2}{\phi_e} \right) - \beta^2 \right] \quad (\text{E-15})$$

where

$$\phi_e = \text{empirical parameter} = 86 \text{ ev}$$

Table VIII is a comparison between results of (E-13) and the stopping power formula for electrons.

TABLE IV
 N_2 VIBRATIONAL EXCITATION CROSS SECTIONS

Level 1 Energy Loss = .290 Threshold = .278

Number	Energy	Cross Section	Number	Energy	Cross Section
1	0	0.0000	18	1.800	.3300
2	.290	0.0000	19	1.900	1.5200
3	.300	.0010	20	2.000	1.3200
4	.330	.0020	21	2.100	.4600
5	.400	.0030	22	2.200	1.6300
6	.750	.0050	23	2.300	1.2300
7	.900	.0065	24	2.400	.4600
8	1.000	.0080	25	2.500	.8600
9	1.100	.0100	26	2.600	1.0400
10	1.165	.0120	27	2.700	.2700
11	1.200	.0137	28	2.800	.4200
12	1.218	.0150	29	2.900	.4270
13	1.400	.0675	30	3.000	.4300
14	1.500	.0950	31	3.100	.5800
15	1.600	.1220	32	3.200	.3800
16	1.6500	.1390	33	3.300	.2900
17	1.700	.1600	34	3.600	.2900
			35	5.000	0.0000

TABLE IV (CONT)

Level 2 Energy Loss = .590 Threshold = 1.692

Number	Energy	Cross Section	Number	Energy	Cross Section
1	1.700	0.0000	10	2.600	.3100
2	1.800	.0900	11	2.700	.4900
3	1.900	.4000	12	2.800	.5100
4	2.000	1.5200	13	2.900	.1800
5	2.100	1.4800	14	3.000	.2400
6	2.200	.6200	15	3.100	.1500
7	2.300	.6000	16	3.200	.1100
8	2.400	1.3900	17	3.300	.0700
9	2.500	1.1400	18	3.400	0.0000

Level 3 Energy Loss = .880 Threshold = 1.692

Number	Energy	Cross Section	Number	Energy	Cross Section
1	1.800	0.0000	10	2.700	.6400
2	1.900	.1800	11	2.800	.2600
3	2.000	.7500	12	2.900	.4000
4	2.100	1.4100	13	3.000	.4000
5	2.200	1.6900	14	3.100	.1600
6	2.300	.9500	15	3.200	.1600
7	2.400	.2900	16	3.300	.1600
8	2.500	.7700	17	3.400	0.0000
9	2.600	1.1700			

TABLE IV (CONT)

Level 4 Energy Loss = 1.170 Threshold = 1.894

Number	Energy	Cross Section	Number	Energy	Cross Section
1	1.9	0.0000	9	2.700	.6000
2	2.0	.1600	10	2.800	.4900
3	2.1	.4600	11	2.900	.1800
4	2.2	1.1000	12	3.000	.1600
5	2.3	1.3000	13	3.100	.1600
6	2.4	.7100	14	3.200	.1100
7	2.5	.2000	15	3.300	.0700
8	2.6	.3100	16	3.400	0.0000

Level 5 Energy Loss = 1.470 Threshold = 1.994

Number	Energy	Cross Section	Number	Energy	Cross Section
1	2.000	0.0000	9	2.800	.3700
2	2.100	.2000	10	2.900	.6200
3	2.200	.4600	11	3.000	.4200
4	2.300	.7700	12	3.100	.2700
5	2.400	1.0400	13	3.200	.3500
6	2.500	1.0100	14	3.300	.3100
7	2.600	.5100	15	3.400	0.0000
8	2.700	.2700			

AD-A071 621

AIR FORCE INST OF TECH WRIGHT-PATTERSON AFB OHIO SCH--ETC F/6 20/3
ELECTRIC AND MAGNETIC FIELDS OF AN INTENSE PULSE OF RELATIVISTI--ETC(U)
1979 K A DREYER
AFIT/DS/PH/79-1

UNCLASSIFIED

NL

3 of 3

AD
A071621



END
DATE
FILMED
8 -79
DDC

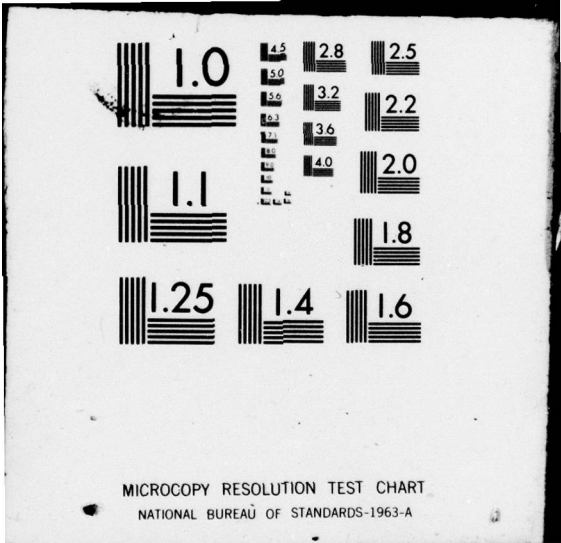


TABLE IV (CONT)

Level 6 Energy Loss = 1.760 Threshold = 2.196

Number	Energy	Cross Section	Number	Energy	Cross Section
1	2.200	0.0000	8	2.900	.0900
2	2.300	.1100	9	3.000	.1600
3	2.400	.3700	10	3.100	.1800
4	2.500	.6000	11	3.200	.0700
5	2.600	.6000	12	3.300	.0500
6	2.700	.3700	13	3.400	0.0000
7	2.800	.1500			

Level 7 Energy Loss = 2.060 Threshold = 2.297

Number	Energy	Cross Section	Number	Energy	Cross Section
1	2.300	0.0000	7	2.900	.1800
2	2.400	.0700	8	3.000	.0500
3	2.500	.1800	9	3.100	.0700
4	2.600	.2900	10	3.200	.1600
5	2.700	.4400	11	3.300	.0700
6	2.800	.3300	12	3.400	0.0000

TABLE IV (CONT)

Level 8 Energy Loss = 2.350 Threshold = 2.499

Number	Energy	Cross Section	Number	Energy	Cross Section
1	2.500	0.0000	5	2.900	.2400
2	2.600	.0700	6	3.000	.1500
3	2.700	.1100	7	3.100	.0700
4	2.800	.1800	8	3.200	0.0000

TABLE V

N₂ ELECTRONIC EXCITATION CROSS SECTIONS

Level 1 Energy Loss = 6.200 Threshold = 6.211

Number	Energy	Cross Section	Number	Energy	Cross Section
1	6.200	0.0000	8	14.00	.1800
2	8.000	.1600	9	20.00	.0900
3	9.000	.2500	10	25.00	.0800
4	10.000	.2800	11	35.000	.0500
5	11.000	.2800	12	50.000	.0170
6	12.000	.1800	13	70.000	.0060
7	13.000	.1500	14	100.000	0.0000

Level 2 Energy Loss = 7.200 Threshold = 7.195

Number	Energy	Cross Section	Number	Energy	Cross Section
1	7.200	0.0000	13	25.000	.0800
2	8.000	.0044	14	30.000	.0700
3	9.000	.0132	15	35.000	.0570
4	10.000	.0220	16	40.000	.0440
5	11.000	.0310	17	45.000	.0403
6	12.000	.0400	18	50.000	.0367
7	13.000	.0480	19	55.000	.0330
8	14.000	.0570	20	60.000	.0290
9	15.000	.0660	21	65.000	.0260

TABLE V (CONT)

Number	Energy	Cross Section	Number	Energy	Cross Section
10	16.000	.0690	22	70.000	.0220
11	18.000	.0756	23	75.000	.0180
12	20.000	0.820	24	100.000	0.0000

Level 3 Energy Loss = 7.400 Threshold = 7.397

Number	Energy	Cross Section	Number	Energy	Cross Section
1	7.400	0.0000	8	14.000	.1500
2	8.000	.1800	9	20.000	.1100
3	9.000	.4100	10	25.000	.0900
4	10.000	.6000	11	35.000	.0600
5	11.000	.6000	12	50.000	.0240
6	12.000	.2200	13	70.000	.0090
7	13.000	.1800	14	100.000	0.0000

Level 4 Energy Loss = 8.400 Threshold = 8.407

Number	Energy	Cross Section	Number	Energy	Cross Section
1	8.400	0.0000	10	35.000	.2500
2	9.000	.0300	11	50.000	.1700
3	10.000	.0900	12	70.000	.1200
4	11.000	.1800	13	100.000	.0800

TABLE V (CONT)

Number	Energy	Cross Section	Number	Energy	Cross Section
5	12.000	.3000	14	200.000	.0400
6	13.000	.3500	15	300.000	.0270
7	16.000	.4100	16	1000.000	.0080
8	20.000	.4100	17	2000.000	0.0000
9	25.000	.3600			

Level 5 Energy Loss = 11.200 Threshold = 11.210

Number	Energy	Cross Section	Number	Energy	Cross Section
1	11.200	0.0000	8	20.000	.1300
2	12.000	.0500	9	25.000	.1000
3	13.000	.2200	10	35.000	.0700
4	14.000	.4200	11	50.000	.0280
5	15.000	.3400	12	70.000	.0100
6	16.000	.2700	13	100.000	0.0000
7	18.000	.1900			

Level 6 Energy Loss - 12.400 Threshold = 12.396

Number	Energy	Cross Section	Number	Energy	Cross Section
1	12.400	0.0000	7	100.000	1.4500
2	15.000	.0650	8	200.000	1.2000

TABLE V (CONT)

Number	Energy	Cross Section	Number	Energy	Cross Section
3	20.000	.2700	9	300.000	.9200
4	30.000	.6700	10	1000.000	.4100
5	50.000	1.2500	11	2000.000	0.0000
6	70.000	1.4500			

Level 7 Energy Loss = 14.400 Threshold = 14.391

Number	Energy	Cross Section	Number	Energy	Cross Section
1	14.400	0.0000	7	100.000	1.8000
2	20.000	.0800	8	200.000	1.5000
3	22.000	.3400	9	300.000	1.1500
4	30.000	.7700	10	1000.000	.5100
5	50.000	1.5500			
6	70.000	1.8000			

TABLE VI

N₂ TOTAL IONIZATION CROSS SECTIONS

Energy Loss = 15.500 Threshold = 15.502

Number	Energy	Cross Section	Number	Energy	Cross Section
1	0.000	0.0000	15	43.000	1.9440
2	15.500	0.0000	16	46.000	2.0880
3	16.590	.0346	17	48.000	2.1660
4	16.760	.0408	18	50.000	2.2270
5	17.110	.0513	19	54.000	2.3700
6	18.680	.1161	20	60.000	2.5300
7	20.000	.2010	21	65.000	2.6200
8	23.000	.4400	22	70.000	2.7000
9	25.000	.6160	23	75.000	2.7600
10	28.000	.8800	24	80.000	2.8100
11	30.000	1.0490	25	85.000	2.8500
12	34.000	1.3600	26	90.000	2.8700
13	37.000	1.5730	27	95.000	2.8900
14	40.000	1.7720	28	100.000	2.900

TABLE VII
 N_2 MOMENTUM TRANSFER CROSS SECTIONS

Number	Energy	Cross Section	Number	Energy	Cross Section
1	6.0000	1.0000	19	2.8000	28.0100
2	.0144	2.4900	20	3.0000	21.6300
3	.0651	4.9000	21	3.3000	17.1900
4	.2260	8.2200	22	3.6000	14.6600
5	.4450	9.9500	23	4.0000	12.6200
6	1.0000	9.9800	24	4.5000	11.5200
7	1.1000	10.1400	25	6.0000	10.3000
8	1.2000	10.5100	26	10.0000	9.5100
9	1.3000	11.0000	27	15.0000	11.1000
10	1.4000	11.4500	28	20.0000	12.0000
11	1.5000	11.9600	29	25.0000	11.7000
12	1.6000	12.9000	30	35.0000	10.5000
13	1.7000	13.4300	31	40.0000	10.1000
14	1.8000	16.9500	32	42.0000	9.9000
15	1.9000	19.8300	33	50.0000	9.3500
16	2.0000	24.0100	34	56.0000	8.8500
17	2.2000	28.7600	35	100.000	6.5600
18	2.6000	29.8800			

TABLE VIII
PARAMETERS FOR ELECTRON IMPACT*

$$F_j(T) = \frac{f_j D_j}{D_j - \exp[-(T - I_j)/\alpha I_j]}$$

$$\Gamma_e(T) = \Gamma_s + \frac{\Gamma_o \Gamma_B^2 T}{(T - E_T)^2 + \Gamma_B^2}$$

$$Q_{oe}(T) = \Gamma_s - \frac{T_A}{(T + T_B)}$$

$$B(T) = B_o \{ \ln[(\gamma - 1)m_e c^2 / E_o]^2 + B_1 \}$$

$$\Gamma_2(T) = \frac{A_1 T}{T - I_j}$$

<u>Parameter</u>	<u>Value</u>
B _o	0.029
B ₁	1.035
E _o (ev)	8239.
T ₁	53.3
Γ ₁	115.
A ₁ (ev)	5000.
α	2.3
K	7.58 x 10 ⁻¹⁶

*Adapted from Porter, Jackman and Green.

TABLE VIII (CONT)

<u>Parameter</u>	<u>Value</u>
Γ_S (ev)	11.1
Γ_O	0.029
Γ_B (ev)	51.3
E_T (ev)	61.5
T_S	4.0
T_A	2450.
T_B	63.8

<u>j</u>	<u>I_j</u>	<u>f_j</u>	<u>D_j</u>	<u>C_j</u>
1	15.58	0.456	4.23	2.48
2	16.73	0.2	2.3	2.66
3	18.75	0.104	3.35	2.99
4	22.	0.07	200	3.50
5	23.6	0.07	200	3.76
6	40.	0.1	200	6.37

TABLE IX
 COMPARISON OF STOPPING POWER FORMULAS
 FOR ELECTRONS

Energy (eV)	from (E-13) eV/cm/molecule	from (E-15) eV/cm/molecule
10^3	5.12×10^{-15}	5.45×10^{-15}
10^4	9.55×10^{-16}	9.31×10^{-16}
10^5	1.73×10^{-16}	1.60×10^{-16}
10^6	7.74×10^{-17}	7.15×10^{-17}
10^7	9.09×10^{-17}	8.44×10^{-17}
10^8	1.15×10^{-16}	1.02×10^{-16}
10^9	1.39×10^{-16}	1.12×10^{-16}

VITA

Kenneth Allen Dreyer was born April 17, 1946 in Cape Girardeau, Missouri. He graduated from high school in Perryville, Missouri, whereupon he attended the University of Missouri, then Southeast Missouri State University from which he graduated with Honor in Physics, in 1968. He attended the University of Arkansas graduate physics program until enlisting in the United States Air Force in 1969. He received his commission from the Officer Training School in the same year. He then matriculated in meteorology at St. Louis University until 1970, when he was assigned to Forbes AFB, Kansas, as a weather forecaster. His next assignment was as Chief Forecaster at Osan AB, Korea, for which work he was awarded the Air Force Commendation Medal. He was a student at the Air Force Institute of Technology from 1973 through 1975. He received a Master of Science Degree from there in Nuclear Engineering. He is a Distinguished Graduate. He is currently assigned as a Theoretical Physics Research Officer at the Air Force Weapons Laboratory.

Permanent address: 118 South Moulton Street
Perryville, Missouri 63775

Unclassified

SECURITY CLASSIFICATION OF THIS PAGE (When Data Entered)

REPORT DOCUMENTATION PAGE		READ INSTRUCTIONS BEFORE COMPLETING FORM
1. REPORT NUMBER AFIT/DS/PH/79-1	2. GOVT ACCESSION NO.	3. RECIPIENT'S CATALOG NUMBER
4. TITLE (and Subtitle) Electric and Magnetic Fields of an Intense Pulse of Relativistic Electrons Propagating Through Air	5. TYPE OF REPORT & PERIOD COVERED Final	
	6. PERFORMING ORG. REPORT NUMBER	
7. AUTHOR(s) Kenneth A. Dreyer	8. CONTRACT OR GRANT NUMBER(s)	
9. PERFORMING ORGANIZATION NAME AND ADDRESS Air Force Institute of Technology Wright-Patterson Air Force Base Ohio 45433	10. PROGRAM ELEMENT PROJECT, TASK AREA & WORK UNIT NUMBERS	
11. CONTROLLING OFFICE NAME AND ADDRESS Air Force Weapons Laboratory (AFSC) Kirtland Air Force Base New Mexico 87117	12. REPORT DATE 9 July 1979	
	13. NUMBER OF PAGES 192	
14. MONITORING AGENCY NAME & ADDRESS (if different from Controlling Office)	15. SECURITY CLASS. (of this report) Unclassified	
	15a. DECLASSIFICATION/DOWNGRADING SCHEDULE	
16. DISTRIBUTION STATEMENT (of this Report) Distribution of this document is unlimited		
17. DISTRIBUTION STATEMENT (of the abstract entered in Block 20, if different from Report) 18 JUL 1970 APPROVED FOR PUBLIC RELEASE AFR 190-17. JOSEPH P. HIPPS, Major, USAF Director of Information		
18. SUPPLEMENTARY NOTES		
19. KEY WORDS (Continue on reverse side if necessary and identify by block number) Electron Beam Beam Fields Beam Propagation Air Chemistry Ionization		
20. ABSTRACT (Continue on reverse side if necessary and identify by block number) Since propagation characteristics of an electron beam traversing a neutral gas are determined by the response of the beam electrons to their self-fields, an accurate evaluation of the electric and magnetic (EM) fields is essential to any propagation analysis. We report here on theoretical models that were developed for the electromagnetic fields associated with an electron beam propagating in air. One- and two-dimensional models of the fields, and a model		

Unclassified

SECURITY CLASSIFICATION OF THIS PAGE(When Data Entered)

20.

for the electron avalanche of the air, were solved on a computer. The major conclusions from calculational results are:

(1) The ionization model adequately describes the ionization process over a pressure range of from five Torr to 760 Torr,

(2) Ionization lag from the high energy secondary electrons is unimportant.

(3) In many cases the one-dimensional model was found to be as good as the two-dimensional model, and

(4) The net current saturates near 15 kilo-Amperes at sea-level pressure, and saturates at lower values at lower air pressure.

Unclassified